WASM: Minerals, Energy and Chemical Engineering

The role of brittleness in hydraulic fracture initiation and propagation mechanisms

Runhua Feng

0000-0003-1722-4265

This Thesis is presented for the Degree of

Doctor of Philosophy

of

Curtin University

Sep 2022

Declarations

To the best of my knowledge and belief, this thesis contains no material previously published by any other person except where due acknowledgment has been made.

This thesis contains no material which has been accepted for the award of any other degree or diploma in any university.

Permission if herewith granted to Curtin University to circulate and to have copied for non-commercial purposes, at its discretion, the above tile upon the request of individuals or institutions.

Signature:_____.

Date: ___07/09/2022_____.

THE AUTHOR RESERVES OTHER PUBLICATION RIGHTS, AND NEITHER THE THESIS NOR EXTENSIVE EXTRACTS FROM IT MAY BE PRINTED OR OTHERWISE REPRODUCED WITHOUT THE AUTHOR'S WRITTEN PERMISSION.

THE AUTHOR ATTESTS THAT PERMISSION HAS BEEN OBTAINED FOR THE USE OF ANY COPYRIGHTED MATERIAL APPEARING IN THIS THESIS AND THAT ALL SUCH USE IS CLEARLY ACKNOWLEDGED.

Abstract

Brittleness index (BI) is a critical parameter characterizing the deformation regime of geo-materials, covering the range from purely brittle (cracks, fractures) to ductile (plastic flow), controlling the fracture development in a wide range of underground applications such as reservoir stimulation, fluid-induced microseismicity, Geosequestration, and Civil Infrastructures. However, the definition and quantification of a reliable BI for hydro-mechanical applications remains a challenge, i.e., the existing BI models are mainly based on rock mechanical parameters but neglect the coupled hydro-mechanical interactions associated with rock deformation at depth. The role of BI in hydraulic fracture propagation in tight sedimentary rock is still poorly understood.

In this study, we have developed a new hydro-mechanical energy-based brittleness index (BI) model; to quantify the hydro-mechanical deformation, a robust analytical model for hydraulic fracture propagation based on Poiseuille's law and scaling analysis is also proposed and validated through literature data. We carried out rock mechanical, creep, and hydraulic fracturing experiments on geomaterials exhibiting a wide range of rheology: cubic samples 50x50x50 mm^3 in size are subjected to true triaxial stresses with a low (σ_v = 6.5 MPa, σ_H =3 MPa, and σ_h =1.5MPa), and a high (15 MPa, 10 MPa, and 5MPa) confinement. The wellbore pressure and three-dimensional (3D) strains induced by hydraulic fracturing are monitored and interpreted. The geometry and surface roughness of hydraulic fracture are documented by X-ray CT images.

By comparison with the conventional BI models from literature, our newly proposed model is inherently advantageous in evaluating the BI of geomaterials involving a wide range of mechanical properties. The interpretation of BI, the 3D strain induced by hydraulic fracturing, geometry of hydraulic fracture, and the creep data reveals that: **(i)** The orientation angle of hydraulic fracture is highly inclined to the maximum horizontal σ_H (or vertical σ_v) stresses in brittle/semi-brittle samples; as BI decreases, the angle inclination is reduced for that of semi-ductile samples, finally reaches to zero (parallel to σ_H and σ_v) in ductile sample. This is attributed to a) the significant plasticity and strain softening in the vicinity of the fracture tip diffuses the stress concentration; b) reduce of stress anisotropy caused by the viscoelastic stress relaxation **(ii)** The intermediate stress plays a profound role in HF propagation and associated rock deformation, which is indicated by the nonlocalized strain softening in semi-ductile/ductile samples. **(iii)** The fracturing area decreases as the BI among different samples under both low and higher confinement. In addition, for the same type of sample, the tortuosity and roughness of fracture surface leads to a larger surface area of hydraulic fracture at the higher confinement rather than that of low confinement.

The results of viscoelastic stress relaxation not only explain the distinct characteristics of hydraulic fracturing induced deformation among the tested samples subjected to true triaxial stress state, but also verify the reliability of our proposed BI models (e.g., BI_9 and BI_{10}). The outcome of this research can facilitate not only laboratory or numerical studies, but also the field applications involving hydraulic fracturing where the complexities of brittle-to-ductile behaviour are required to be considered.

Acknowledgements

I had the privilege of working with my supervisors, teammates, colleagues, and friends. The Ph.D. journey would not be completed without the help and encouragement from them.

First of all, I would like to express my sincere and deep gratitude to my academic supervisor, **A/Prof. Mohammad Sarmadivaleh**, for your excellent mentor and assistance during my master & Ph.D. study: your hand-training of both industrial and in-house built True Triaxial Stress Cells (TTSCs) bring me into a new scientific world of hydraulic fracturing experiments -"In the past years I wish there were 25hrs for everyday at the Geomechanics laboratory". The experience and dedication from Dr.Sarmadivaleh provide a significant contribution to completion of this thesis.

Next, I would like to give my deep gratitude to my associated supervisor, **Dr. Joel Sarout** from CSIRO Energy. I did remember the first time we met at your office, your systematic training of the software-Insite Seismic Processor for microseismic monitoring & interpretation were so attractive, encouraging me toward the deep understanding of hydraulic fracture propagation. I am deeply grateful for your great contribution in insightful discussion, review, and revision of the manuscripts especially for the theoretical and experimental parts of this thesis. Thank you for your numerous time, great mentor and motivation during these four years. I also would like to thank my associated supervisor, **Dr. Jeremie Dautriat** from CSIRO Energy, for your consistent training of the laboratory software, and the design & setting up of the apparatus for acoustic monitoring at CSIRO Geomechanics & Geophysics Lab. Many thanks for your insightful discussion on preparation, and characterization of rock samples for hydraulic fracturing experiments; providing invaluable comments of the manuscripts for this study.

Prof. Reza Rezaae, one of my co-supervisors, who taught me two core units in Petroleum Geology during my master study. Many thanks for your great lecture which helps me understand the fundamental concept as well as the field applications in solving the industrial problems. During my Ph.D. time, I am grateful to attend many of your academic seminars, in which broaden my knowledge and skills of research. I sincerely appreciate for your time in discussing about the experimental results and reviewing of the manuscript. I also would like to acknowledge **Prof. Hamid Roshan,** one of my external supervisors from UNSW who providing constructive comments and help me in reviewing & editing the manuscripts for this thesis.

I also want to thank **Prof. Mofazzal Hossain,** who taught me two core units in of Petroleum Production Engineering during my master study. Much appreciate for the opportunity you offered me for training from some of your research projects. As my thesis chairperson, your great help and advices always motivate me for both master and Ph.D study. **Prof. Ali Saeed,** many thanks for the two core units in Reservoir Engineering you taught during my Master study. Much appreciate for the opportunity you offered me for learning from some of your research projects. Your great advices and mentorship always motivate me in completing my Ph.D study. I also would like to thank **Dr. Ali Rezagholilou,** who is one of my co-supervisors during my master study, for your great mentorship & assistant of the initial discussion, sample preparation, rock mechanical and hydraulic fracturing experiments. I also would like to extend my acknowledgement to the staffs from CSIRO Geomechanics & Geophysics Lab, sincere thanks to **Dr. Ausama Giwelli, Shane Kager, David Nguyen, Leigh Kiewiet, Neil Sturrock, and Dr. Mustafa Sari.**

It is also my great honour to acknowledge some of my elite colleagues at Curtin University. Many thanks for the meet and collaboration during my Ph.D study. First of all, I would thank **Dr. Shuo Liu** and her husband-**Mr. Guanghan Chu**, who were my talent teammates during my master study; **Dr. Liu** continued her Ph.D study on numerical simulations of hydraulic fracturing in our geomechanics group. Much appreciate for your motivation, research collaboration, great assistance of CT images segmentation and experiments; also, the "delightful conversations daily", and "Gourmet food" you dedicated should not be forgot not only during my Ph.D study but also for my rest of life. A special thanks goes to **Mr. Chu**, who provides great help in my daily life during these years, such as heavy apparatus handling, Delicious meal offering, car repairment, and the most impressive moment-blocking my layup & fadeaway jump-shot no matter how much effort I made crossover & pump fake as always. I would like to thank **Dr.Miftah Hidayat,** one of the exchange Ph.D student recently graduated from University of Aberdeen. I appreciate your companionship at the laboratory & office, or dining table day and night. The lexical word created for us only -"Tough Brothers" should never be forgot. I would like to thank **Dr.Xuekai Li**, who provides the constructive comments for my experiments and thesis during my Ph.D study. I would like to thank **Dr.Yubing Liu and Dr. Zhiqi Zhong** who provide the constructive comments and collaboration opportunities. I would like to thank **Dr. Hongyi Sun** and **Dr. Shoaib Memon** for your industrial advice, experimental assistance, and collaboration opportunities. I would like to thank **Dr.Yihuai Zhang**, who provides the constructive comments and experimental assistance during the early

stage of my Ph.D study. Also, I would like to thank **Dr.Cut-Aja Fauziah, Dr. Partha Mandal, Dr. Lingping Zeng**, **Dr. Jamiu Ekundayo, Dr.Pei Li, Dr.Jiang jia, Dr. Faaiz Shajalee, Dr.Muhammad Atif Iqbal, Dr.Yujie Yuan, and Dr.Jie Zou** for their assistance, collaboration, and friendship during my Ph.D study. At the end, thanks for all the staffs and students from Petroleum Engineering Department and WASM, as well as the staffs from graduate school, Curtin University for their assistance.

I would like to acknowledge some of the elite colleagues from other institutions, a special thank to **Dr. Quanquan Cao** from University of Montpellier, now as a professor at Sichuan Agricultural University. **Dr. Cao** is not only one of my great colleagues, but also my best friend since junior high school. I do appreciate the great moment we spent many years ago, and the encouragement from you in recent years. **Dr. Qingjia Cui** from Hunan University, one of my best friends since high school, who encouraged me a lot for my undergraduate and research study. **Dr. Miftah Hidayat** from University of Aberdeen, as I mentioned before, we are "tough brothers" who stayed day and night at lab & office. I would like to thank **Dr. Hongyu Wang** who is from University of Western Australia, for your consistent help and encouragement for my research study. I would like to thank **Dr. Jiecheng Zhang** from Texas A&M University, now as a researcher in China University of Petroleum. **Dr. Zhang** was one of my most talent colleagues since my undergraduate study at University of Tulsa, as I did remember the time we worked as the teammates for the final capstone design. Thanks for your continuing encouragement and collaboration until now. **Dr. Yun Yang** from University of Calgary, who is also one of my most talent colleagues since the undergraduate study at TU, I appreciate your consistent help and encouragement for my research study. **Dr. Qianjun Liu** from University of Texas at Austin, many thanks to **Dr.Liu** for the encouragement; and the collaboration opportunity in the history matching of fractured reservoir constrained by microseismic data, which enhanced my knowledge and understanding of the application of MS data in the field. Also, I would like to give my acknowledgement and best wishes to the colleagues named as following: **Dr. Andreas Michael** from Colorado School of Mines, **Dr. Yunfeng Chen** from Zhejiang University, **Dr. Ruijia Wang** from Southern University of Science and Technology, and **Dr. Hongliang Zhang** from University of Alberta.

At the end, I would like to express my deepest appreciation to my parents for their endless love and support since I was born. I cannot pursue this degree without your love and support, I love you from bottom of heart.

Perth, 7th Sep, 2022 Runhua Feng

Acknowledgements of Financial Support

I sincerely thanks China Scholarship Council-Curtin International Postgraduate Research Scholarship (CSC-CIPRS, Grant No. 201808190001) for their four-years financial support on this research.

Perth, 7th Sep, 2022 Runhua Feng

©Copyright by Runhua Feng 2022

All Rights Reserved

Table of Contents

List of Figures

List of Tables

Chapter 1

Introduction

1 Introduction

Hydraulic fracturing has been widely used in many underground applications, e.g. reservoir stimulation, geothermal energy extraction, geo-sequestration, etc. Brittleness Index (BI) has been recognized as one of the key parameters controlling the development of hydraulic fracture (HF) in geo-materials. However, quantification of BI for such hydro-mechanical applications remains a challenge, i.e., the existing BI models are mainly based on rock mechanical parameters but neglect the coupled hydro-mechanical interactions associated with rock deformation at depth. The role of brittle/ductile rock behavior in hydraulic fracture propagation is yet not fully understood. The aim of this thesis is to understand the physics of multiscale fluid-driven fracture in different geomaterials, and develop a robust physical modelling framework for studying the role of BI in hydraulic fracture growth in these applications. To that end, I am taking an interdisciplinary study uniting analytical and experimental fluid/solid mechanics and physics. The outcome of this research can facilitate not only physical and numerical modelling, but also the field applications.

This chapter includes a modified content from the following scientific articles:

Feng R., Liu S., Sarout J., Dautriat J., Zhong Z., Rezaee R., Sarmadivaleh M (2022a). Hydraulic fracturing: Laboratory evidence of the brittle-to-ductile transition with depth. Preprint DOI: doi.org/10.31223/ X55M1J

Feng R., Zhang Y., Rezagholilou A., Roshan H., Sarmadivaleh M (2020). Brittleness Index: From Conventional to Hydraulic Fracturing Energy Model. *Rock Mechanics and Rock Engineering* 53: 739-753.

1.1 Hydraulic fracturing

Hydraulic fracturing is a technique to artificially create hydraulic fracture (HF), which facilitates the permeability enhancement of unconventional reservoir for economic production (Economides and Nolte 1989). This technique has also been applied in many other engineering fields, such as geothermal energy (Legarth et al. 2005; Salimzadeh et al. 2018), geo-sequestration (Papanastasiou et al. 2016), civil infrastructures (Tedd et al. 2011), contaminated soils (Murdoch 1993), waste disposal (De Laguna 1966), in-situ stress measurement (Serdyukov et al. 2016), etc. For improving the efficiency of these applications, a deeper understanding of the characteristics of HF propagation is essential. However, the HF propagation is underlying a coupled multi-physics and scale-dependent process, requiring an extensive numerical-laboratory appraisal to assess feasibility in the field.

When hydraulic fracture initiates and propagates within geo-materials under *in-situ* stresses, three types of failure modes are often observed: mode-I (tensile), mode-II (shear), and mixed-mode-I and II (Economides and Nolte 1989; Wu 2006; Gischig and Preisig 2015; Feng et al 2019). The uncertainties of the failure mode may arise as the confinement varies, i.e., the alteration of rock rheology and mechanical properties, which may challenge the characterization of failure modes and HF propagation. In addition, the stress anisotropy, fluid properties, and natural fractures are also recognized as the influential factors for the failure mode (Papanastasiou 1997; Zhou et al. 2008; Zhang et al. 2009; Sarmadivaleh 2012; Gischig and Preisig 2015; Liu et al. 2020a; Wang 2019; Yang et al. 2021; Liu et al. 2022). Incorporating all these parameters in fracturing analysis is complicated to be achieved either in numerical or laboratory study. Since the hydraulic fracture growth is a dynamic process where the damage is mainly accumulated adjacent to the tip within the process zone (Bunger 2005b; Desroches et al. 1994; Elices et al. 2002; Garagash 2019; Ju et al. 2021; Liu and Lecampion 2021; Papanastasiou 1997), which is highly influenced by the mechanical property of the materials. Several studies demonstrated that the plastic yielding/strain softening at the tip will absorb the effective injection energy, which significantly hinders the fracture propagation and results in a uniformed fracture geometry in ductile rocks (Feng et al. 2020; Ju et al. 2021; Papanastasiou 1997; Parisio et al. 2021).

1.2 Brittleness index

Brittleness is a critical mechanical criterion that identifies the fracability of a formation (Tarasov and Potvin 2013). The conventional brittleness index (*BI*) models have been mainly developed based on a) rock mechanical responses (Altindag and Guney 2010; Bishop 1967; Hajiabdolmajid et al. 2003; Hucka and Das 1974; Tarasov and Potvin 2013), b) rock acoustic responses (Rickman et al. 2008) and c) mineralogical composition (Jarvie et al. 2007; Jin et al. 2015; Wang and Gale 2009). For example, Bishop (1967) introduced a *BI* model based on the peak (Tf) and residual strength (Tr) of the rock obtained from the triaxial stress loading. Hajiabdolmajid et al. (2003) later suggested that the developed plastic strain must be considered in the model development and proposed a new strain-based *BI* model. It is however ducumented that both the strength-dependent and strain-dependent *BI* models have significant uncertainties and limitations. For instance, the rocks with the identical strength can exhibit different displacments along the same stress path (Hajiabdolmajid et al. 2003; Zhang et al. 2016). Hucka and Das (1974) defined their *BI* model as the ratio of elastic deformation energy to the total deformation energy obtained from the stress-strain response of the rock. They

suggested that combining the uniaxial compressive strength (UCS) with tensile strength (σ_T), and the internal friction angle (Φ) can quantify the *BI* more accurately. Despite this effort, there is no consistency amongst these formulations leading to rather questionable practical applications of these models.

The more practical approach based on petrophysical analysis was introduced by Rickman et al. (2008). In this approach, *BI* was obtained using Dynamic Young's modulus (*E*) and Passion's ratio (*v*) extracted from the acoustic log data. The method has been particularly attractive as no core sample is required. Field implementation of the model, however, indicated that *BI* of quartz-rich shale (candidate) and limestone (caprock) formations cannot be differentiated using this approach (Perez Altamar and Marfurt 2014). Altindag and Guney (2010) later proposed a *BI* model by correlating the specific energy (corresponding to *UCS* and σ_T) and brittleness. This *BI* model has been widely applied to drilling and tunneling applications; however, its application to hydraulic fracturing operation is yet to be assessed. Tarasov and Potvin (2013) defined the brittleness of the rock based on the post-peak energy release (correlating the loading and unloading elastic modulus) in tri-axial loading. This model considered both the pre- and post-failure process to describe the deformation range from brittle to ductile regime. However, it is hard to obtain the precise stress-strain response for the model during the post-peak stage (Zhang et al. 2016). Jin et al. (2015) proposed a modified mineralogical approach and reported a good agreement of the model with the experimental data. The extrapolation of such non-physical correlation beyond its measurement range can be however erroneous. In addition, mineralogy alone is very unlikely to give a good estimate of the *BI* since the other factors such as grain size and skeleton cementation have profound effect on brittleness (Luan et al. 2014). In a current effort, Papanastasiou et al. (2016) presented a new definition of *BI* for hydraulic fracturing based on dislocation theory, which combines the rock strength with in-situ stresses. This model is based on Mohr-Coulomb criterion and was derived from analytical model of hydraulic fracturing in weak formations, however; the model has not been validated experimentally.

1.3 Motivation

In the past decades, a few studies regarding to the role of brittle/ductile rock behaviour in hydraulic fracturing appeared **(Table 1.1**). Papanastasiou and Thiercelin (1993) numerically studied the role of inelastic rock behaviour in hydraulic fracturing, this study was then extended by Papanastasiou (1997) and Papanastasiou (1999) using Mohr-coulomb flow theory of plasticity with a two-dimensional (2D) coupled finite element-finite difference scheme. He

showed that significant plasticity and strain softening in the vicinity of the fracture tip increases the fracture toughness, resulting in more energy required for propagating an elasto-plastic fracture rather than elastic fracture. The similar modelling approach was performed by van Dam et al. (2002), in which he also conducted laboratory experiments on hard and soft rocks. They demonstrated that the tip plasticity increases the fracture width with a lower propagation pressure in soft rocks. Later, Yao (2012) modified a cohesive zone model to study the HF propagation behaviour in brittle and ductile rocks, the results indicated that fracture toughness increases as the ductility increases. Wang (2015) applied the coupled CZM and XFEM model to demonstrate that the hydraulic fracture always propagates to the lower Young's modulus within the elastic formation; abnormal fracturing pressure is caused by in-elastic rock behaviour such as shear failure.

Recently, Shimizu et al. (2018) studied the effect of brittleness in the complexity of hydraulic fracture using discrete element method. Their results indicate the brittleness plays a positive role in the HF complexity. Huang and Chen (2021) numerically studied the effect of ductility in a single hydraulic fracture growth by a modified traction-separation law. Their results reveal that Young's modulus (E) appears as the most influential parameter for brittle/ductile behaviour, in which the HF length decreases as the E decreases. Ju et al. (2021) performed a 3D numerical model for hydraulic fracture propagation in tightly brittle and ductile reservoirs. They confirmed that the stress concentration near the fracture tip is highly accommodated in the ductile reservoir. Parisio et al. (2021) carried out an experimental study of the brittle-to-ductile transition of hydraulic fracture within Polymethyl Methacrylate (PMMA). They observed complex fracture patterns under non-uniform stress distribution in the sample under the brittle regime. The complexity of fracture is significantly reduced as the ductility increases.

Although the abovementioned studies shedlighted the road of studying brittleness in hydraulic fracturing, a pracitical and unified brittleness index (BI) model for characterizing the ductile behaviour of rock subjected to hydraulic fracturing, is not fully developed. Moreover, experimental studies for understanding the hydraulic fracture initiation & propagation behaviour under the true triaxial stresses conditions (TTSC) are scared, especially for the materials with a wide range of mechanical properties. Here we focus on the development of a unified brittleness index (BI) model and the study of BI in hydraulic fracture initiation & propagation behaviour of a wide range of material types.

Table 1.1 Literature for Brittle/ductile rock behavior subjected to hydraulic fracturing

Study	Method	Researcher	Results
The influence of plasticity in hydraulic fracturing	Numerical (FEM)	*Papanastasiou (1997)*	Elasto-plastic fracture is shorter and wider than an elastic fracture; higher propagation pressure
Impact of Rock Plasticity on Hydraulic Fracture Propagation and Closure	Experimental+ Numerical (FEM)	*Van Dam et al (2000)*	Plasticity induces a larger fracture width; a lower propagation pressure
Linear elastic and cohesive fracture analysis to model hydraulic fracture in brittle and ductile rocks	Numerical (FEM)	*Yao (2012)*	Fracture toughness is increased in ductile rock
Numerical modeling of non-planar hydraulic fracture propagation in brittle and ductile rocks	Numerical (XFEM)	*Wang (2015)*	In-elastic deformation induced by HF plays a role in propagating pressure and geometry
A study of the effect of brittleness on hydraulic fracture complexity	Numerical (DEM)	*Shimizu et al (2018)*	Complexity of hydraulic fractures is anticipated in the higher brittleness of rock
Effects of Ductility of Organic-Rich Shale on Hydraulic Fracturing	Numerical (XFEM)	*Huang and Chen (2021)*	Fracture length is reduced with the increase of ductility
3D Numerical Model for Hydraulic Fracture Propagation in Tight Ductile Reservoirs	Numerical (Coupled FE-DEM)	*Ju et al (2021)*	Geometry of hydraulic fracture transits from complexity (brittle) to uniform (ductile reservoir)
A laboratory study of hydraulic fracturing at the brittle-ductile transition	Experimental	*Parisio et al (2021)*	The complexity of HF is reduced as the increase of ductility

1.4 Research Objective

- Quantification of the brittleness index of geomaterials based on the existing BI models
- Development and validation of a practical Brittleness Index (BI) model for hydraulic fracturing
- Hydraulic fracture characterization, e.g., geometry, dimensions for a wide range of rock samples under true triaxial stresses conditions (TTSC) at Lab scale
- Interpretation of the quantified BI and the characterization of hydraulic fracture attributes

1.5 Research Significance

- The consistency and effectiveness of existing BI models for hydraulic fracturing application;
- Two new and robust Brittleness index (BI) models are proposed and validated for HF;
- A robust analytical model for hydraulic fracture propagation (temporal radius prediction) is newly developed;
- Hydraulic fracture attributes, i.e., Geometry, and Dimensions are interpreted for variable rock samples under TTSC;

- The brittle-to-ductile transition is observed in orientation angle, intermediate strain, and fracturing area among testing samples
- Creation of laboratory data set for validation/improvement of the theoretical models.

1.6 Thesis Structure

This thesis is organized as two main parts-I Theory Development detailed in Chapters 2-3 and II Experiments and Results detailed in Chapters 4-6:

I Theory Development

Chapter 2 discusses the brittleness index (BI) model development for hydraulic fracturing (HF) application. We have developed a preliminary BI model based on the partitioning of the total injection energy E_I into kinetic energy E_k , and aseismic deformation energy E_d associated with hydraulic fracture propagation, using wellbore pressure data as input. Later, the BI model is optimized by introducing a constitutive relation between wellbore pressure and the three-dimensional strain recorded during hydraulic fracturing subjected to true triaxial stress conditions (TTSC). Finally, the directly calculated aseismic deformation energy E_d offers a more accurate quantification of the BI comparing to the previous two models.

Chapter 3 investigates the newly developed analytical model for hydraulic fracture propagation (i.e., temporal radius prediction). This model (R_d) predicts the fracture opening and internal pressure gradient using Poiseuille's law and assuming a homothetic propagation. Scaling laws and dimensional analysis are used to define the propagation regimes; non-linear hydro-mechanical coupling is accounted in the near-tip region. This model (R_d) is validated by published laboratory data. As a benchmark comparison, we also quantify the growth of the fracture radius using linear elastic fracture growth model (R_E); and tip asymptotic solutions (R_V and R_T).

II Experiments and Results

Chapter 4 presents rock mechanical tests and the core experiments. In this thesis, hydraulic fracturing tests conducted under both low and high TTSC in synthetic rock samples exhibiting a wide range of mechanical properties. We interpreted the experimental data, e.g., wellbore pressure, 3D and volumetric strain induced by hydraulic fracturing, and the geometry of hydraulic fracture.

Chapter 5 discusses the brittleness index (BI) quantification based on our developed theory-energy partitioning (BI_8), cohesive energy concept (BI_9), direct quantification of aseismic deformation energy (BI_{10}) and the experimental results.

Chapter 6 finally presents the interpretation of the quantified BI based on the newly developed model BI_{10} and the characterized hydraulic fracture (HF) attributes, e.g., HF geometry, fracturing area, roughness of the fracture surface.

Conclusions and Recommendations are reported in **Chapter 7.**

Appendices are given at the end for supporting information of this thesis

I Theory Development

Chapter 2
Brittleness Index (BI) model development for hydraulic fracturing applications

2 Brittleness Index (BI) model development for hydraulic fracturing applications

This chapter discusses the brittleness index (BI) model development for hydraulic fracturing (HF) application. We initially developed a model (BI_8) based on the partitioning of the total injection energy E_I into surface energy E_G , and aseismic deformation energy E_d associated with hydraulic fracture propagation, using wellbore pressure data as representative (**Section 2.2.1**). Later, the BI_8 is optimized by introducing a phenomenological relation between wellbore pressure and the three-dimensional strain recorded during hydraulic fracturing subjected to true triaxial stress conditions (BI_9)(**Section 2.2.2**). Finally, the direct calculation of aseismic deformation energy E_d and injection energy E_I is introduced (BI_{10}) (**Section 2.2.3**), which may offer a more reliable quantification of the BI comparing to the previous two models.

This chapter includes a modified content from the following scientific articles:

Feng R., Sarout J., Dautriat J., Ghuwainim Y., Rezaee R., Sarmadivaleh M (2022b). Laboratory validation of a new hydro-mechanical energy-based brittleness index model for hydraulic fracturing. Preprint DOI: doi.org/10.31223/X55M1J

Feng R., Zhang Y., Rezagholilou A., Roshan H., Sarmadivaleh M (2020). Brittleness Index: From Conventional to Hydraulic Fracturing Energy Model. *Rock Mechanics and Rock Engineering* 53: 739-753.

2.1 Introduction

The deformation of a geo-material comprises several stages with shear stress increasing toward failure: Stage I – low-strain initial elastic deformation; Stage II – non-recoverable (inelastic) deformation, e.g., brittle micro-cracking, or ductile/plastic flow; Stage III – micro-cracks coalescence and macroscopic fracture propagation/strain localisation, resulting in the failure of the rock. In this context, conventional BI models were developed based on either a) triaxial stress-strain data; b) the recoverable/total strain energy ratio; or c) mechanical parameters derived from multiple rock mechanics tests (Altindag and Guney 2010; Hucka and Das 1974; Tarasov and Potvin 2013). Such BI models are suitable for near-surface applications with relatively low magnitudes of deviatoric stress, e.g., tunnel engineering (Hajiabdolmajid and Kaiser 2003; Steiner et al. 2011; Yagiz et al. 2020). However, they may have limited application in deeper underground environments where natural or anthropogenic fluid-driven fracturing takes place. The depth, and therefore the in situ effective (triaxial) stress will affect the mechanical response of the rock, e.g., static and dynamic elastic properties,

brittleness/ductility, yield/failure type, post-failure behaviour (Dautriat et al. 2011; Feng et al. 2019; He et al. 2021; Huang and Chen 2021; Iyare et al. 2021; Li et al. 2020b; Liu et al. 2020; Sarout et al. 2014; Sarout and Guéguen 2008a; Sarout and Guéguen 2008b). Such depth-dependent rock deformation features should be accounted for in order to devise the most reliable and efficient BI model, i.e., sensitive, discriminative, reproducible.

Rickman et al. (2008) proposed a practical BI model for unconventional shale reservoirs based on sonic and density logs, which provides the dynamic Young's Modulus E_{dyn}, and Poisson's ratio v_{dyn}, disregarding the post-failure response of the rock, which limits the applicability of this model to relative brittleness quantification only (Cho and Perez 2014). Feng et al. (2020) showed that Rickman et al.'s BI model agrees only qualitatively with other models based on the post-failure behaviour of the rock. Reported limitations of this BI model include: (i) unphysical increase of the BI with confining pressure (Holt et al. 2015); and (ii) limited discrimination between brittle and ductile depth intervals (Perez Altamar and Marfurt 2014; Zhang et al. 2016). Despite its reported limitations, this BI model is commonly applied in the field. More recently, Papanastasiou et al. (2016) proposed an analytical BI based on Mohr-Coulomb's brittle failure model, where the internal friction angle Φ, the cohesion C_o, the maximum (σ_{max} vertical) and minimum (σ_{min} horizontal) principal stresses are accounted for in a mode-I hydraulic fracture propagation scenario (ideal propagation scenario). However, the BI values computed with this model are unexpectedly low when the difference between σ_{max} and σ_{min} becomes significant (Feng et al. 2020).

An alternative BI model based on hydraulic fracturing energy was recently reported by Feng et al. (2020)**,** in which the induced deformation energy E_d is estimated through energy partitioning from wellbore pressure data, avoiding the need for direct strain measurements. They also experimentally examined the consistency and applicability of a total of eight distinct BI models available in the literature, including the abovementioned BI models (Feng et al. 2020). They found that the models from Rickman et al. (2008)**,** Papanastasiou et al. (2016), and Feng et al. (2020) followed qualitatively consistent trends for different rock types. However, Feng et al. (2020) experimentally showed that the magnitude of the BI from Rickman et al. (2008) was significantly larger than the seven other BI models analysed for synthetic quartz-rich samples (analogous to S_1 in this article). In addition, Holt et al. (Holt et al. 2015) also showed that the BI value from Rickman et al. (2008) increases with confining pressure, which is unphysical, i.e., rock brittleness (ductility) should decrease (increase) with increasing confining pressure. Feng et al. (2020) also showed experimentally that the BI values from

Papanastasiou et al. (2016) range between 0.1 and 0.22, significantly lower than the seven other BI models analysed for several synthetic rock types (S_1 to S_4). These discrepancies are attributed to (i) a difference in model definition, (ii) the calculation of the aseismic deformation energy E_d, and to (iii) the inherent uncertainties associated with rock deformation measurements.

Beyond the injection rate, hydraulic fracture initiation and propagation is governed by multiple parameters, including, but not limited to (i) the viscosity of the injected fluid; (ii) rock mechanical properties (elastic moduli, brittleness/ductility, mechanical strength, fracture toughness); and (iii) boundary conditions, e.g., triaxial stress field at depth. To our knowledge, no BI model based on fluid-induced rock deformation and fracturing under realistic triaxial stress conditions has been published in the literature.

The goal of this chapter is to introduce the theory of our BI model development for hydro-mechanical deformation associated applications. The information on conventional *BI* models (i.e. BI_1 to BI_7) investigated in this thesis and on our proposed BI models (e.g., BI_8 to BI_{10}) are shown in **Table 2.1**.

Table 2.1 List of Brittleness Index (BI) models investigated in this study

BI models	Description	Test Method	Reference
$BI_1 = \frac{\varepsilon_{el}}{\varepsilon_{total}}$	ε_{el} -Recoverable strain ε_{total} -Total strain	UCS test	Hucka and Das (1974)
$BI_2 = \frac{W_{re}}{W_{total}}$	W_{re}-Recoverable energy W_{total}-Total energy	As above	Hucka and Das (1974)
$BI_3 = \frac{1}{2}(\frac{E_{dyn}(0.8-\emptyset)-1}{8-1} + \frac{v_{dyn}-0.4}{0.15-0.4})$	E_{dyn}-Dynamic Young's Modulus v_{dyn}-Dynamic Poisson's Ratio $\emptyset$-Porosity	Acoustic measurement	Rickman et al (2008)
$BI_4 = \frac{UCS-\sigma_T}{UCS+\sigma_T}$	σ_c-Unconfined compressive strength σ_T-Maximum tensile strength	Brazilian and UCS test	Hucka and Das (1974)
$BI_5 = \sqrt{\frac{UCS*\sigma_T}{2}}$	As above	As above	Altindag and Guney (2010)
$BI_6 = \sin(\Phi)$	Φ-Internal friction angle	TCS test	Hucka and Das (1974)

$BI_7 = 1 - \frac{(\sigma_1 - \sigma_3)}{2c\ cos\Phi + (\sigma_1 + \sigma_3)sin\Phi}$	σ_1-Maximum principle stress; σ_3-Minimum principle stress Φ-Internal friction angle c- Cohesion	TCS test	Papanastasiou and Atkinson (2015)
$BI_8 = 1 - \frac{E_d}{E_d + E_G}$	E_d - Deformation energy (represented by wellbore pressure response) E_G - Surface energy (represented by wellbore pressure response)	Hydraulic fracturing test	Defined in this study (Feng et al (2020))
$BI_9 = 1 - \frac{G_{Hcd}}{G_{HD}}$ $= 1 - \frac{\int_{\xi_i}^{\xi_{re}} [P_W(\xi) - \sigma_r - \sigma_\mu] d\xi}{[P_{Wp} - \sigma_r - \sigma_\mu] \times (\xi_{re} - \xi_i)}$	P_W – Wellbore pressure ξ- Strain Induced by fracture propagation σ_r -Residual stress σ_μ -Residual Viscous force G_{Hcd}-strain energy release rate induced by a typical hydraulic fracture G_{HD}-strain energy release rate induced by a hydraulic fracture in an ideally ductile rock	Hydraulic fracturing test (with strain)	Defined in this study
$BI_{10} = 1 - \frac{E_d}{E_I} = 1 - \frac{\int_{L_{r_1}}^{L_{r_2}} A_d P(L_r)\, dL_r}{Q \int_{t_1}^{t_2} P(t) dt}$	A_d – Temporal fracturing area $P(L_r)$-Wellbore pressure Q- Injection rate L_r- Resultant strain E_d – Aseismic Deformation energy E_I - Injection energy	Hydraulic fracturing test (with strain)	Defined in this study (Feng et al (2021))

2.2 BI model development

2.2.1 BI model based on empirical energy partitioning (BI_8)

Griffith's energy criterion derived based on linear elastic fracture mechanics (LEFM) (Griffith 1921) has been widely applied to simulate the fracture propagation in brittle materials. Orowan (1954) and Irwin (1957) modified the energy criteria by considering the irreversible energy mechanism:

$$\frac{dU_s}{dc} \geq \frac{dU_y}{dc} + \frac{dU_p}{dc} \tag{2.1}$$

where U_s is the elastic potential energy (or strain energy); U_y is the surface energy; U_p is plastic deformation energy and c is the crack length. Eq. (6) emphasizes that for a crack propagation, the minimum released strain energy rate ($\frac{dU_s}{dc}$) should be exceed or equal to the crack resistance (right-hand side of **Eq.2.1**).

On the other hand, the energy criterion of hydraulic fracture propagation can be expressed (Goodfellow et al. 2015):

$$E_I + \Delta W = \overbrace{E_G + E_d + I}^{E_{HF}} + \overbrace{E_f + E_H + E_R}^{E_{AES}} \quad (2.2)$$

Where E_I is the fluid injection energy and ΔW is the change in elastic potential energy. On the right hand side of **Eq. (2.2)**, the associated output energy can be divided into two main parts: hydraulic fracture components (E_{HF}) and seismic dissipated energy (E_{AES}). E_{HF} consists of E_G (the energy needed to create new fracture faces), E_d (aseismic deformation energy according to fracture opening/dilation), and I (any additional energy loss). The I itself includes the viscous dissipation energy (I_v) and fluid leak-off loss (I_l). It is noted that the majority of energy is consumed by E_G, E_d and I processes during fracturing (Shlyapobersky 1985; Zhao et al. 2018). Furthermore, the radiated seismic energy, E_{AES} accounts for friction of microshear plane (E_f), new surface creation of mircoshear failure (E_H) and energy radiated as ultrasonic waves (E_R). This radiated seismic energy (E_{AES}) during hydraulic fracture propagation is << 1% of the injection energy based on both field observations (Boroumand and Eaton 2012; Maxwell et al. 2008; Warpinski et al. 2012) and laboratory measurements (Goodfellow et al. 2015). It is therefore intuitive to assume $E_{AES} \approx 0$. In addition, the change in elastic potential energy, ΔW is negligible in the formulation of energy budget (Goodfellow et al. 2015). The fluid leak-off is also neglected due to ultra-low permeability of the samples (i.e. below 0.01mD).

With above assumptions, **Eq. (2.2)** can be simplified:

$$E_I = E_G + E_d + I_v \quad (2.3)$$

It is known that the increase in rock deformation with ductile behaviour increases the energy required for fracture propagation (Fischer-Cripps 2007; Wang 2019; Yao 2012). As plastic deformation increases the effective fracture toughness, less fracture surface area is created at the same level of injection energy thus causing higher net pressure (Papanastasiou 1999). Yao (2012) performed numerical analysis based on cohesive fracture mechanics for brittle and ductile rock. The results showed that i) in an ideally brittle rock, the wellbore pressure (BHP)

dramatically decreases once it reaches the critical value of formation break-down and ii) for the ideally ductile rock, BHP increases gradually after fracture initiation and large plastic strain is developed. This phenomenon was also observed in the field operations (Jiang et al. 2017). Thus for an ideally ductile rock, the injection energy was mainly used to produce the rock deformation during the fracture propagation -from formation breakdown (t_b) to the end time of hydraulic fracture propagation (t_f). This means that additional injection energy (in addition to the energy stored in fracture until breakdown) is required to propagate the fracture (in this case, fracture propagation pressure is assumed to be maximum, see **Fig.2.1**).

Considering above statement, we examine the two extreme ends of **Eq. (2.3)** where the rock is ideally brittle or ductile. It is seen from **Fig.2.1** that E_d dominates the energy consumption/release in fracture propagation for an ideally ductile sample (i.e. BI = 0, represented by the orange curve A-D in **Fig.2.1**), which generates an exceptionally short wide fracture (Yao 2012). On the other hand, E_d approaches zero but E_G dominates the energy release for an ideal brittle case (i.e. BI = 1, represented by the green curve A-B-C in **Fig.2.1**), which produces a long narrow fracture. Therefore, we formulate the new brittleness index based on these extreme cases, where BI is related to an empirical energy partitioning $\frac{E_d}{E_d+E_G}$. The maximum value for viscous dissipation energy I_v can be estimated when fracture reaches the boundaries of the specimen (EFCB area in **Fig.2.1**) which is subtracted from the energy balance shown in **Eq. (2.3)** in the new BI model. With this analogy, the new BI model can be expressed:

$$BI_8 = 1 - \frac{E_d}{E_d+E_G} \tag{2.4}$$

which is schematically represented by areas shown in **Fig.2.1**:

$$BI_8 = 1 - \frac{S_{ABC}}{S_{ABCD}} \tag{2.5}$$

Equation 2.5 is an empirical estimation of the **Eq. (2.4)** and was thus used to calculate the BI_8 in this study.

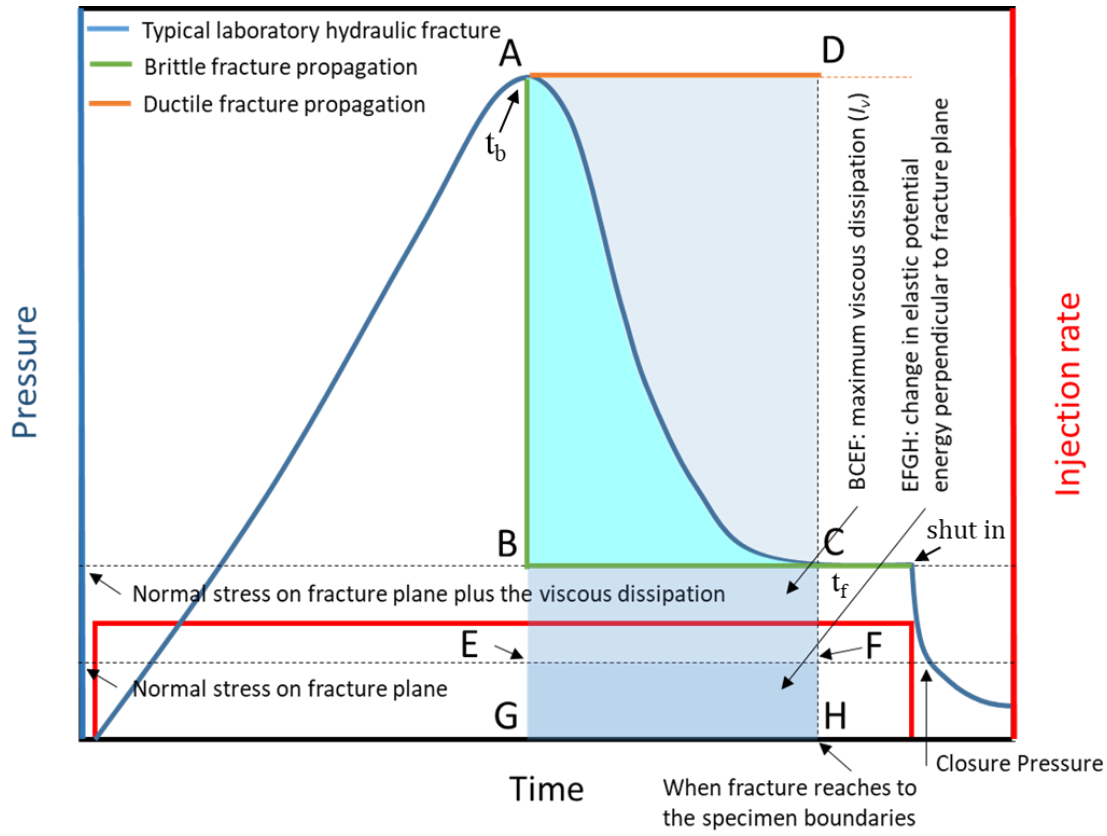

Fig.2.1 Schematic of typical pressure curve during hydraulic fracturing test

2.2.2 BI model based on cohesive energy concept (BI_9)

The quantification of BI_8 relies on the empirical response of wellbore pressure data, which may lead to the uncertainties of prediction of brittleness index (BI) among a wide range of rock types. Therefore, in this section, we introduce the integration of the wellbore pressure and the strain induced by hydraulic fracturing. Based on the cohesive energy concept, we proposed an optimized model BI_9, which may increase the accuracy and consistency of BI prediction.

Cohesive zone model (CZM) has been widely used in describing the stress induced elasto-plastic fracturing process especially for capturing the nonlinearity ahead of crack tip in geomaterials subjected to failure (Bradley 2013; Elices et al. 2002; Lisjak et al. 2013; Lisjak et al. 2014; Wang and Nakamura 2004). Elices et al. (2002) provided an informative review of the application of CZM in different materials, e.g., concrete, PMMA, and steel. He shows that the softening behavior predicted by CEM is consistent with that from experimental measurement of such materials. Elices et al. (2002) also argued that the inherent simplicity of concept and computation of CEM achieve an optimized balance between the capability and

accuracy. Later, Wang and Nakamura (2004) demonstrated that the cohesive element is more applicable for simulating the failure process in inhomogeneous (graded) materials. Lisjak et al. (2013) and Lisjak et al. (2014) performed numerical study of the mechanical behavior of geomaterials (e.g., Opalinus clay, brittle rock), and demonstrated that the applicability of cohesive model in finite/discrete element method. Recently, Pan et al. (2021) numerically studied the role of micro-scaled heterogeneity in mechanical properties of brittle rocks, and argued that the CEM is successfully applied with the grain-based discrete element method.

The cohesive-zone method (CZM) has also been used as a propagation criterion of hydraulic fracture in geomaterials. To address the process zone ahead the fracture tip, Papanastasiou (1997;1999), Sarris and Papanastasiou (2011), and Yao (2012) incorporated an approach called cohesive fracture mechanics into a finite element analysis for simulating the hydraulic fracture propagation in ductile rock. Such non-elastic behavior induced by hydraulic fracture propagation within the naturally fractured shale was numerically studied by Taleghani et al. (2018), in which he presented and validated an integrated approach based on triaxiality and the CZM. Recently, Huang and Chen (2021) modified the conventional cohesive zone model by unified variable traction/separation laws, and they demonstrated the applicability of CZM in modelling of ductile shale. Such application was also studied by Alpak (2021), in which he validated the reliability of CZM in both poro-elastic and poro-plastic geomechanics implementations. Very recently, Liu et al (2022) performed a microstructure-based modelling of hydraulic fracture propagation in brittle metamorphic rock using CZM and validated it against experimental results.

Given the applicability and reliability of CZM in both brittle, quasi-brittle, and ductile geomaterials, and the related experimental response of stress and strain regarding the brittle-to-ductile transition observed by Lisjak et al. (2014), we therefore incorporate two endmembers for the traction-separation relation (CZM), and the energy partitioning concept (Feng et al. 2020) into a new brittleness index (BI) model.

The dynamic failure of rock can be modelled as a cohesive-zone approach, aiming to address the non-linearity between stress and strain charactering of the fracture process zone adjacent to macro-crack tip (Bradley 2013). According to cohesive element failure process (Bradley 2013), the strain energy release rate of a cohesive crack for the two type of failure modes, tensile (G_{IC}), and shear (G_{IIC}) are:

$$G_{IC} = \int_{\varepsilon_i}^{\varepsilon_r} \sigma(\varepsilon) d\varepsilon \tag{2.6}$$

$$G_{IIC} = \int_{S_i}^{S_r} [\tau(s) - f_r] ds \quad (2.7)$$

where ε_r is the strain resulting from fracture opening; $\sigma(\varepsilon)$, and $\tau(s)$ are the normal or shear bonding stress corresponding to the tensile ε_r and shear strain S_r, from fracture nucleation ε_i or S_i; f_r is the residual shear strength.

For hydraulic fracture (HF) propagation under confining stress, the total injection energy contributes to four main components, (i) the kinetic energy (hydraulic force) driving the fracture creating new surface; (ii) the aseismic deformation energy due to the tip plasticity within the cohesive zone; (iii) the energy required to keep HF open against confining stress; (iv) the energy dissipated within viscous fluid.

Therefore, the release rate of strain energy for a typical hydraulic fracture (G_{Hcd}) reads:

$$G_{Hcd} = \int_{\xi_i}^{\xi_r} [P_W(\xi) - F_R] d\xi \quad (2.8)$$

where ξ_r is the strain resulting from fracture opening; ξ_i is the initial strain from fracture nucleation; $P_w(\xi)$ is the wellbore pressure as a function of the strain ξ; F_R is the residual stress mainly attributed to the confining stress (σ_h) and viscous force of fluid (σ_μ).

As shown in **Fig.2.2**, for a hydraulic fracture that propagates until the boundary of sample ξ_{re}, **Eq.2.8** can be rewritten as:

$$G_{Hcd} = \int_{\xi_i}^{\xi_{re}} [P_W(\xi) - \sigma_h - \sigma_\mu] d\xi \quad (2.9)$$

For hydraulic fracture that propagates in an ideally ductile rock, the strain energy release rate G_{HD} can be represented as:

$$G_{HD} = [P_{Wp} - \sigma_h - \sigma_\mu] \times (\xi_{re} - \xi_i) \quad (2.10)$$

where P_{wp} is the maximum wellbore pressure subjected to fracture initiation (formation breakdown).

Therefore, the brittleness index (BI) of a rock subjected to hydraulic fracturing is defined as:

$$BI_9 = 1 - \frac{G_{Hcd}}{G_{HD}} = 1 - \frac{\int_{\xi_i}^{\xi_{re}} [P_W(\xi) - \sigma_h - \sigma_\mu] d\xi}{[P_{Wp} - \sigma_h - \sigma_\mu] \times (\xi_{re} - \xi_i)} \quad (2.11)$$

Eq.(11) can be schematically represented by the areas(S):

$$BI_9 = 1 - \frac{G_{HCd}}{G_{HD}} = 1 - \frac{S_{ABCD}}{S_{ABCE}} \quad (2.12)$$

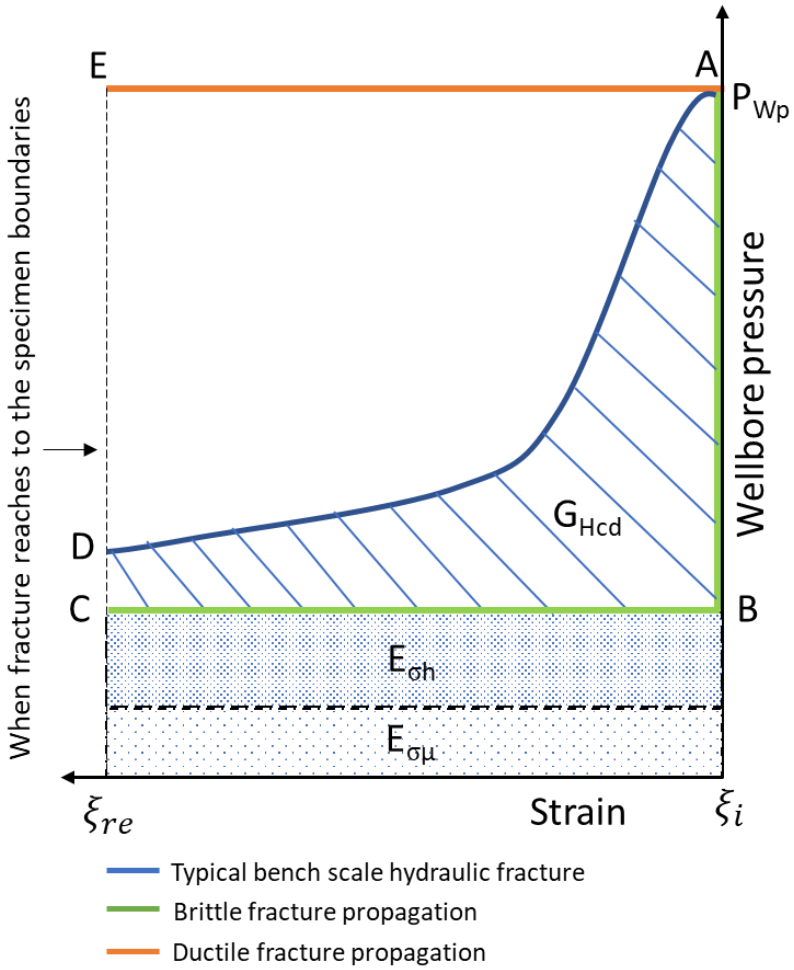

Fig.2.2 Schematic representation of energy description for a typical constitutive behaviour of wellbore pressure and strain induced by a hydraulic fracture (HF) propagation under confinement: G_{Hcd} denotes the release rate of strain energy for a typical hydraulic fracture (represented by area ABCD); $E_{\sigma h}$ and $E_{\sigma \mu}$ denote the residual energy for confining stress (σ_h) normal to HF propagation and the viscous force of fluid (σ_μ), respectively.

2.2.3 BI model based on calculation of aseismic deformation energy (*BI*$_{10}$)

In the previous two sections we discuss the BI model development based on empirical wellbore pressure response (*BI*$_8$) and the cohesive energy concept (*BI*$_9$), but there is no direct calculation of the aseismic deformation energy (E_d) has been done yet for BI quantification. In this section, we introduce the new BI model based on the calculation of aseismic deformation energy-E_d and injection energy-E_I.

Considering the displacement induced by the opening hydraulic fracture (2D displacement field shown in **Fig.2.3**), the induced aseismic deformation energy E_d reads

$$E_d = \int_{L_{r_i}}^{L_{r_e}} A_d \, P(D_r) \, dL_r, \tag{2.13}$$

where A_d is the temporal-evolving fracturing area (The calculation of A_d is detailed in **Chapter 3**) where the surface roughness is neglected; L_r is the displacement resulting from the opening fracture; $P(L_r)$ is the wellbore pressure corresponding to the displacement L_r, from fracture nucleation L_{ri}, to the end of fracture propagation L_{re}. In ductile rocks, most of the injection energy E_I is dissipated through aseismic deformation ($E_I \sim E_d$), while kinetic energy E_k can be neglected, i.e., $E_k << E_d$ (Feng et al. 2020).The opposite holds in brittle rocks, for which $E_I \sim E_k$ and $E_d << E_k$. In this context, we defined a new Brittleness Index BI_3 as the ratio of E_d/E_I,

$$BI_{10} = 1 - \frac{E_d}{E_I} = 1 - \frac{\int_{L_{r_1}}^{L_{r_2}} A_d\, P(L_r) dL_r}{Q \int_{t_1}^{t_2} P(t) dt}\,. \tag{2.14}$$

In practice, fracture propagation in controlled laboratory conditions can be complex, e.g., jagged or straight propagation, orthogonal to the minimum principal stress or not. In this study, we consider both a) idealized fracture orientation (mode-I) - the fracture propagates perpendicular to the direction of minimum stress (e.g., horizonal stress σ_h); and b) anomalous fracture orientation (mixed mode-I and II) - the fracture ends up inclined with respect (as opposed to orthogonal) to the direction of minimum stress. Considering a single vertical fracture subjected to the *in-situ* horizontal stresses σ_h and σ_H, (see **Fig.2.3a**), the resulting normal stress on the fracture surface σ_r reads

$$\sigma_r = \sigma_h \cos\theta + \sigma_H \sin\theta, \tag{2.15}$$

where θ is the angle between the fracture plane and the maximum horizontal stress σ_H (or between the normal vector to the fracture surface and the minimum horizontal stress σ_h). The resulting 2D displacement L_r in this plane reads

$$L_r = \varepsilon_h D_h \cos\theta + \varepsilon_H D_H \sin\theta\,, \tag{2.16}$$

where ε_h and ε_H are the strains induced by the fracture in the two horizontal directions, i.e., along σ_h and σ_H, respectively; D_h and D_H are the dimensions of the sample in these directions, respectively. In the case of an idealised fracture orientation ($\theta = 0°$), the normal stress σ_r reduces to σ_h, and L_r reduces to $\varepsilon_h \times D_h$.

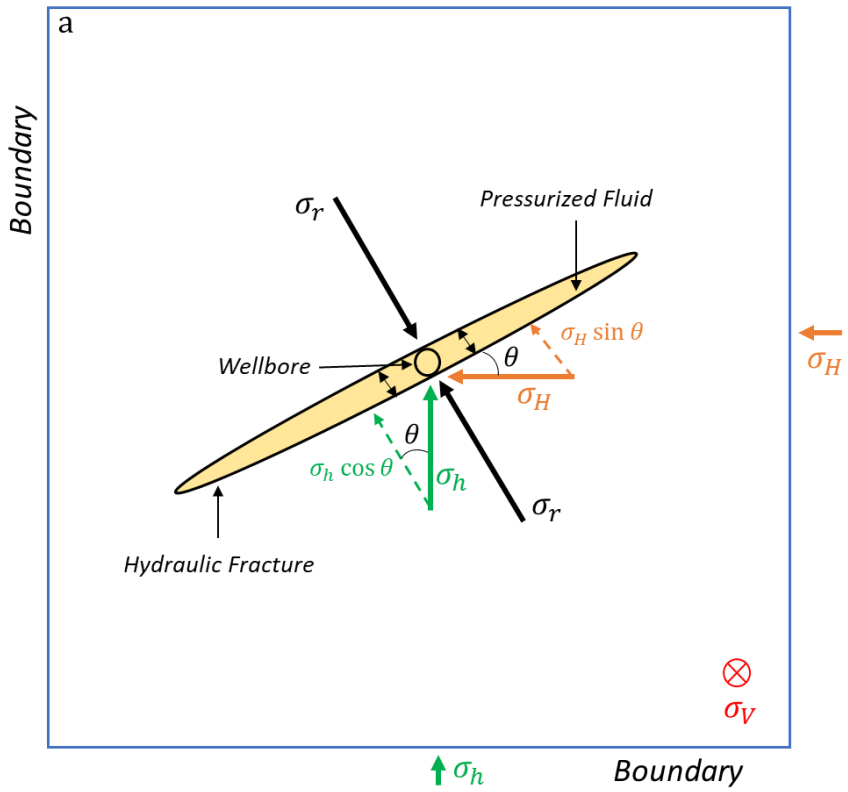

Fig.2.3 2D Schematic of an inclined (anomalous) hydraulic fracture propagation

Chapter 3
Analytical model for prediction of temporal fracturing radius during propagation of a hydraulic fracture at laboratory

3 Analytical model for prediction of temporal fracturing radius during propagation of a hydraulic fracture at laboratory

Hydraulic fracturing is a coupled multi-physics and scale-dependent process requiring an extensive numerical-laboratory appraisal to assess feasibility in the field. Developing a robust model of hydraulic fracture propagation requires knowledge of the time evolution of the geometrical attributes, e.g., width/aperture and length/radius. However, it is inherently challenging to directly measure even the simplest fracture attribute (i.e., radius) within a rock sample subjected to confining stresses in the laboratory, let alone in the field. In this study, an analytical model is developed to predict the time evolution of the radius for a penny-shaped hydraulic fracture. This model (R_d) predicts the fracture opening and internal pressure gradient using Poiseuille's law and assuming a homothetic propagation. Scaling laws and dimensional analysis are used to define propagation regimes. Non-linear hydro-mechanical coupling is accounted for in the near-tip region. Based on the available experimental data from literature, we quantify the growth of the fracture radius using linear elastic fracture growth model (R_E); tip asymptotic solutions (R_V and R_T); semi-analytical solutions (R_S); and the model R_d. A comparison of the four analytical models with published experimental data reveal that (i) the asymptotic solutions are limited to linearly elastic and homogeneous materials, i.e., PMMA; (ii) the semi-analytical solutions (R_S) is only suitable for late-time propagation (iii) the performance of the linear elastic model (R_E) poorly matches the experimental data, especially for unstable propagation situations; (iv) the new R_d model takes advantage of a robust reconstruction of the temporal radius growth of hydraulic fracture problems under realistic stress conditions. This model also considers the multiscale propagation regimes, cohesive effects, as well as stable and unstable propagation regimes of geomaterials.

This chapter includes a modified content from the following scientific article:

Feng R., Sarout J., Dautriat J., Zhang J., Roshan H., Rezaee R., Sarmadivaleh M (2022c). Data-constrained analytical model for the propagation of a penny-shaped hydraulic fracture under true triaxial stresses. *Engineering Fracture Mechanics*, under review. Preprint DOI: doi.org/10.21203/rs.3.rs-1525036/v4

3.1 Introduction

Fluid-driven fracture propagation has been studied for application to subsurface reservoir stimulation operations (Bunger 2005; Adachi et al. 2007; Sarmadivaleh 2012; Salimzadeh and

Khalili 2015; ; Lecampion et al. 2017; Garagash 2019; Huang and Chen 2021), geothermal energy extraction (Legarth et al. 2005; Salimzadeh et al. 2018), CO_2 geo-sequestration (Papanastasiou et al. 2016), control of fluid-induced seismicity (Amitrano 2003; ; Shapiro 2015; Goebel et al. 2017; Liu et al. 2022), and modelling of magma migration (Weinberg and Regenauer-Lieb 2010). The underlying hydro-mechanical interactions taking place at depth are governed by the coupling between fluid flow and rock deformation under prescribed *in-situ* stress conditions.

Early investigations of crack propagation in solids were based on mathematical solutions of elasticity, i.e., solving integral equations (England and Green 1963; Green and Zerna 1992), or using the Fourier transform(Sneddon 1946; Sneddon 1995). In the initial attempts, mathematical solutions were proposed for the propagation of a Griffith fracture in plane strain (Sneddon and Elliot 1946), and for the propagation of a penny-shaped fracture in three dimensions (Sneddon 1946).

Later, these models were enriched to account for fluid flow, fluid mass balance and fracture geometry, and applied to hydraulic fracturing problems, e.g., (i) Perkins and Kern (1961) and Nordgren (1972) developed the so-called PKN model for the propagation in the horizontal direction of a vertical fracture with an elliptical cross-section, assuming a constant fracture height much smaller than fracture length, and a one-dimensional fluid flow within the fracture; (ii) Zheltov (1955) and Geertsma and De Klerk (1969) developed the so-called KGD model for the propagation in the horizontal direction of a vertical fracture with a rectangular cross-section, assuming a constant fracture height much larger than the fracture length, and a one-dimensional fluid flow within the fracture; and (iii) Abé et al. (1976) and Advani et al. (1987) developped a propagation model for a two-dimensional penny-shaped hydraulic fracture, accounting for two-dimensional fluid flow within it (**Fig.3.*1*a**).

To remain mathematically tractable, these analytical models are generally based on simplifying assumptions corresponding to asymptotic regimes that can be relevant in specific conditions. In practice though, they only offer approximate solutions to actual, more complex problems in the field, e.g., heterogeneity of the rock formation or fluid leak-off within the fracture. In fact, hydromechanical coupling and the impact of the boundary conditions (far field stress) will lead to non-linear fracture propagation locally, which must be captured in order to achieve robust and accurate predictions for a specific application.

To address the inherent limitations of analytical models, numerical simulations of fracture propagation in pseudo-3D were introduced in the early 70s (Fung et al. 1987; Simonson et al.

1978), followed by more accurate but costly planar-3D (PL3D) models (Clifton and Abou-Sayed 1981; ; Vandamme and Curran 1989; Advani et al. 1990; Clifton and Wang 1991; Naceur et al. 1990). Recently, Lecampion and Desroches (2015) presented a PL3D model for the initiation and propagation of a radial fracture based on an implicit time-stepping scheme and involving the Displacement Discontinuity Method (DDM) (Lecampion and Detournay 2007). Notably, this model captures the initiation and early-time propagation of the fracture, when nonlinearity dominates. However, this approach requires to iteratively track the front of the propagating fracture and update the system of equations, which is computationally costly in practice. In addition, the application of the DDM is restricted to homogenous and linear elastic solids (Lecampion and Desroches 2015). For heterogeneous rocks with non-local deformation around the fracture tip (process zone) a discrepancy exists between model predictions and experimental observations, typically in terms of wellbore pressure and fracture width (Lecampion et al. 2017). Note also that computational costs are aggravated when modelling heterogeneous or anisotropic reservoirs. Alternatively, the time and scale integration of multiple tip asymptotic solutions to predict hydraulic fracture propagation leads to a good agreement with experimental data for homogeneous and brittle materials such as Polymethyl Methacrylate (PMMA), or synthetic cement/sand samples (Garagash and Detournay 2000; Savitski and Detournay 2002; Lecampion and Detournay 2007; Bunger and Detournay 2007; Kovalyshen 2010; Lecampion et al. 2017).

Linear hydraulic fracture mechanics (LHFM) incorporates linear elastic fracture mechanics (LEFM) and Poiseuille's flow law. This approach is widely used to model the growth of a hydraulic fracture in homogeneous and brittle materials such as PMMA or glass (Bunger and Detournay 2008; Liu 2021). However, the nonlinearity induced by the deformation and energy dissipation taking place in the cohesive (process) zone, and by fluid flow near the tip region within quasi-brittle materials (e.g., sedimentary rock) are often neglected (Liu 2021). Earlier studies show that the LHFM approach is suitable for low ratio of confining to cohesive stress (σ_o/σ_c). Significant deviations from LHFM predictions are observed in laboratory or field applications when the dimensionless ratio σ_o/σ_c becomes large (Adachi et al. 2007; Garagash 2019). This may explain the discrepancy observed between numerical simulation results and experimental observations for heterogeneous rocks subjected to realistic triaxial stress fields (De Pater et al. 1994b; Lecampion et al. 2017; van Dam et al. 2000b). For example, Poiseuille's cubic flow law is well accepted for modelling the laminar flow of highly viscous fluids such as magma within fractures, where the process zone is embedded in the fluid lag zone (**Fig.3.1b**).

However, for a low-viscous fracturing fluid (e.g., slick water or gel), the lag zone is usually embedded in the process zone (**Fig.3.1c**), where the cubic flow law is no longer valid (Garagash 2019). Therefore, for quasi-brittle materials, the determination of the fluid lag and cohesive zone adjacent to the crack tip are necessary for validating the use of Poiseuille's cubic flow law in modelling hydraulic fracturing.

Simultaneous measurement of the borehole pressure (BHP), fracture radius (R), and width/aperture (w) of a hydraulic fracture under true triaxial stress condition (TTSC) are scarce in the literature (De Pater et al. 1994b; Lhomme 2005). In the laboratory, the width of hydraulic fracture can be estimated by measuring the bulk deformation of the rock sample with Linear Variable Differential Transformers (LVDT) attached to its faces, or internal LVDTs located within the wellbore. However, tracking the evolution of the fracture's radius is technically more challenging. Such radius estimations were traditionally performed on samples of transparent material with a high-speed camera (Bunger 2005), or using active and/or passive ultrasonic monitoring (De Pater et al. 1994b; Lhomme 2005; Nabipour 2013; Kovalyshen et al. 2014). To overcome the aforementioned mathematical, numerical, or experimental challenges for tracking the extent of a hydraulic fracture, it is essential to develop a robust model using the less and most reliable input data, for application to the widest range of underground stimulation projects.

Here, we develop a new analytical model for the temporal evolution of the fracture radius R_d for a radial hydraulic fracture (**Fig.3.1a**). For this R_d model, and based on dimensional analysis, we discuss the possible propagation regimes for various near-tip conditions (i.e., cohesive zone, fluid lag). For comparison, we also quantify the radius based on linear elastic fracture growth model (R_E); asymptotic solutions (R_v and R_T); and semi-analytical solutions (R_S). The four analytical models are then verified using literature data (i.e., Seven different materials: Cement/Sand, Colton and Felser sandstones, and PMMAs). Finally, the results and recommendations of the several models are discussed. **Table 3.1** compares the characteristics of the existing methods from the literature and the newly R_d model defined in this paper.

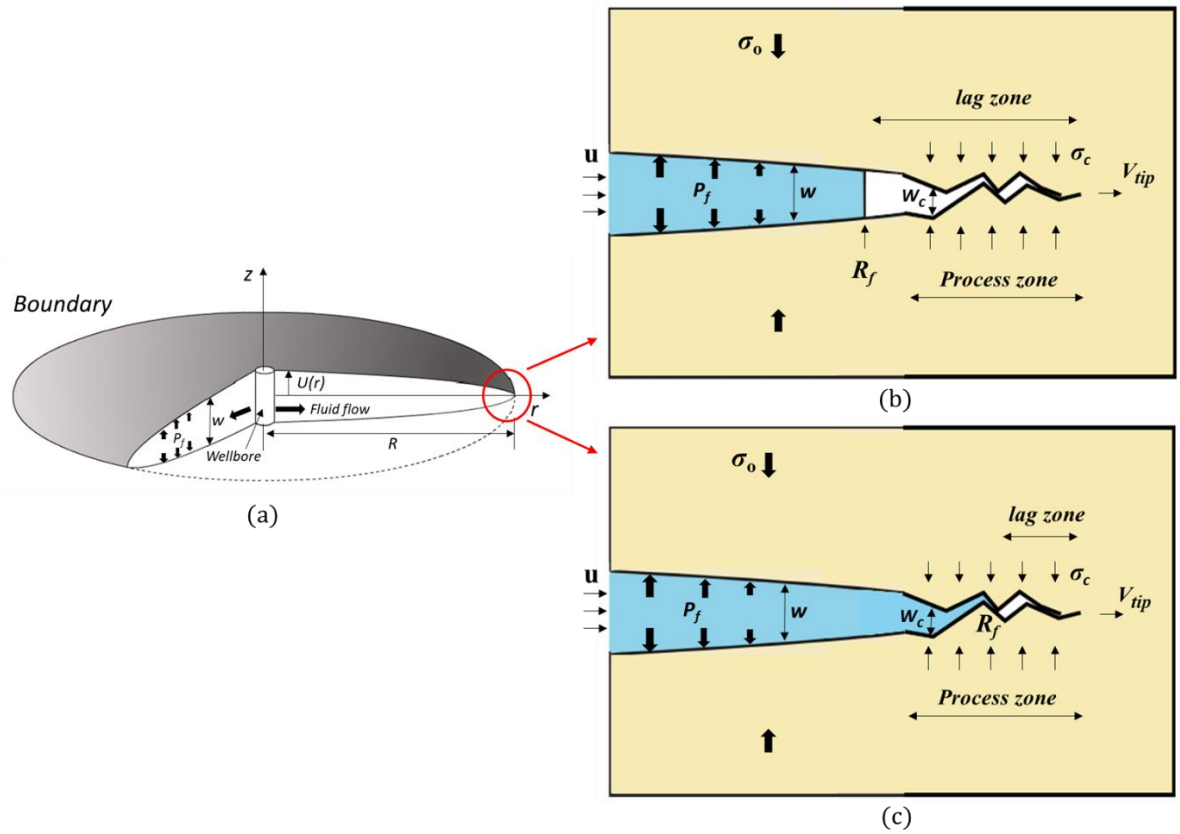

Fig.3.1 Schematic of penny-shaped hydraulic fracture **a)** 3D geometry of propagation adapted from Valkó and Economides (1995) and Savitski and Detournay (2002), **b)** the near-tip region modelled as Poiseuille flow with significant lag in a semi-infinite crack (image modified from Garagash (2015)) and **c)** the near-tip region modelled as "rough" channel flow with limited lag zone in a semi-infinite crack (image modified from Garagash (2019))

Table 3.1 Radius prediction of penny-shaped hydraulic fracture: Comparison between existing methods and our new developed analytical model R_d

	Reference	Assumption	Early-time initiation	Fluid lag	Cohesive zone
Analytical approximation	Abé et al. 1976; Advani et al. 1987	Homogeneous, linear elastic medium			
Asymptotic solutions	Savitski and Detournay 2002; Detournay 2004	Homogeneous, linear elastic medium		✓	
Numerical work	Lecampion and Desroches (2015); Lecampion et al (2017)	Homogeneous isotropic medium	✓	✓	
Experimental measurement	Lhomme (2005); Nabipour (2013)	N/A	✓		
Temporal radius model R_E (analytical)	Sneddon (1946); Valkó and Economides (1995)	linear elastic medium	✓		

Semi-analytical solution R_S	Dontsov (2016)	Homogeneous, linear elastic medium		✓	
Temporal radius model R_d (analytical)	Defined in this paper	Homothetic propagation	✓	✓	✓

3.2 Fracture propagation models

3.2.1 Elastic fracture growth model (R_E)

Linear elasticity is widely applied for static equilibrium of solids (Green and Zerna 1992; Valkó and Economides 1995). For the propagation of a penny-shaped fracture **(Fig.3.1a)**, borehole pressure (BHP) is a function of mechanical properties (Young's modulus E and Poisson's ratio ν), fracture dimensions (radius R and width w), and time t, i.e., BHP = f (w, R, E, ν, t). The propagation of hydraulic fractures can be described by linear elasticity using the Fourier transform (Sneddon 1995). Solving the initial-boundary value problem for a penny-shaped fracture propagating from a borehole at $r = 0$ entails constructing an auxiliary function $g(\xi)$ (Green and Zerna 1992; Sneddon 1995; Valkó and Economides 1995), i.e.,

$$g(\xi) = \frac{2}{\pi}\int_0^{\xi} \frac{P(\xi)}{(\xi^2 - r^2)^{\frac{1}{2}}}\, r\, dr, \text{ with } 0 < \xi < R, \tag{3.1}$$

where ξ is a dummy length variable; $g(\xi)$ possesses the dimension of a fluid pressure P; r is a point on the fracture surface, and R is the radius of the fracture at a given time t. Considering **Eq. (3.1)**, the normal displacement of any point on the upper part of the fracture disk reads

$$U_z(r) = \frac{2}{E'}\int_r^R \frac{g(\xi)}{(\xi^2 - r^2)^{\frac{1}{2}}}\, \xi\, d\xi, \text{ with } 0 \le r \le R, \tag{3.2}$$

where E' is the plane strain modulus.

The fluid pressure within a real hydraulic fracture is not uniform, and more complex fluid pressure distributions can be approximated by a polynomial Taylor expansion in terms of the small variable ξ, i.e.,

$$P(\xi) = P_o + \frac{P_1}{1!}\xi + \frac{P_2}{2!}\xi^2 + o(r^3) \tag{3.3}$$

Where P_o is the initial fluid pressure at the wellbore (zeroth-order), P_1, and P_2 are the primary and secondary pressure gradients (i.e., $P_1 = \frac{\partial p}{\partial r}$ and $P_2 = \frac{\partial p^2}{\partial^2 r}$), which are unfortunately difficult to determine in practice.

For sake of simplicity, we assume a uniform fluid pressure within the fracture, $P(\xi) = P_0$, the auxiliary function **Eq. (3.1**) reduces to

$$g(\xi) = P_o \xi. \quad (3.4)$$

Integration of **Eq. (3.2)** over the radius r yields the fracture's aperture $w = 2\ U_Z(r)$, i.e.,

$$w(r) = \frac{8}{\pi E'} P_o \sqrt{R^2 - r^2}, \text{ with } 0 \le r \le R. \quad (3.5)$$

For an elliptical cross-section of the fracture (see **Fig.3.1a)**, the maximum width occurs at the wellbore ($r = 0$),

$$w_{\max}(r = 0) = \frac{8}{\pi E'}\ P_o R. \quad (3.6)$$

Correspondingly, fracture width is nominally zero at the tip, where $r = R$, i.e.,

$$w_{\min}(r = R) = 0. \quad (3.7)$$

3.2.2 Homothetic fracture growth model (R_d)

Considering a possible fluid lag (see **Fig.3.1b and c**) for a cohesive hydraulic fracture (Garagash 2015; 2019), we introduce the fluid radius R_f, smaller or approximately equal to the fracture radius R, i.e., $R_f < R$ *or* $R_f \approx R$. Poiseuille's law is used to describe the flow of a Newtonian fluid driven by fluid pressure within a penny-shaped fracture (Batchelor and Batchelor 2000; Lecampion et al. 2017)

$$q(r,t) = w(r,t)\ u(r,t) = -\frac{w(r,t)^3}{12\ \mu_f}\frac{\partial p_f(r,t)}{\partial r}, \text{ with } 0 < r < R_f < R, \quad (3.8)$$

where q is the flow rate per unit of fracture perimeter; $w\,(r,t)$ is the width/aperture of the fracture; $p_f\,(r,t)$ is the fluid pressure within the fracture; $u(t) = dR_f(t)/dt$ is the velocity of the fluid at the fluid front $r = R_f(t)$; and μ_f is the viscosity of the fluid. Note that $R_f = R_f(t)$ and $R = R(t)$ are time-dependent during fracture propagation.

Assuming a self-similar (homothetic) hydraulic fracture growth for **Eq. (3.8)** (see **Fig.3.2**), and considering Stefan condition at the interface between the fluid front and the lag at $r = R_f(t)$, leads to (Lecampion et al. 2017)

$$\frac{dR_f(t)}{dt} = -\frac{w(r,t)^2}{12\ \mu_f}\frac{\partial p_f(r,t)}{\partial r}\Big|_{r=R_f} \quad \text{at } r = R_f\,, \quad (3.9)$$

where the change in fluid pressure with radius at $r = R_f$, i.e., $\partial p_f(r,t)/\partial r\big|_{r=Rf}$, is difficult to evaluate in practice, whether in the laboratory or in the field. Eq. (3.9) can be rewritten as (see derivation in **Appendix A.1**)

$$\frac{dR_f(t)}{dt} = \sqrt{\frac{w(r,t)^2}{12\ \mu_f}\frac{\partial p_f(r,t)}{\partial t}\Big|_{r=R_f}} \quad \text{at } r = R_f\,, \quad (3.10)$$

which now involves the change in fluid pressure with time at the fluid front $r = R_f$, i.e., $\partial p_f(r,t)/\partial t\big|_{r=Rf}$. Although the fluid pressure variations within the borehole (i.e., at the fracture inlet) are known, the fluid pressure variations at the moving fluid front $r = R_f$ during fracture propagation is difficult to evaluate, whether in the laboratory or in the field.

Therefore, we further assume that for a given time increment the pressure-time variations at the fluid front and at the fracture inlet (borehole) are proportional (see justification in **Appendix A.2**), i.e.,

$$\frac{\partial p_f(r,t)}{\partial t}\Big|_{r=Rf} \cong -\lambda_p(t)\ \frac{\partial p_f(r,t)}{\partial t}\Big|_{r=0} = -\lambda_p(t)\ \frac{dp_o(t)}{dt}, \tag{3.11}$$

where $dp_o(t)/dt$ is the borehole pressure-time variations often recorded in laboratory experiments or field stimulation operations. This assumption of proportionality at each time increment during propagation ultimately implies that the proportionality coefficient can in principle be time-dependent, i.e., different for consecutive time increments $\lambda_p = \lambda_p(t)$. However, based on laboratory fracturing data reported in the literature (see **Appendix A.3** for details), the proportionality coefficient $\lambda_p(t)$ is found to be relatively constant during propagation for a given fracturing experiment. This empirical observation allows us to simplify **Eq. (3.11)** to

$$\frac{\partial p_f(r,t)}{\partial t}\Big|_{r=R_f} \cong -\lambda_p\ \frac{dp_o(t)}{dt}. \tag{3.12}$$

Combining **Eqs.(3.10) and (3.12)** yields

$$\frac{dR_f(t)}{dt} \cong \sqrt{-\lambda_p \frac{w(0,t)^2}{12\,\mu_f}\frac{dp_o(t)}{dt}}. \tag{3.13}$$

where $w(0,t)$ is the width at wellbore, varies with time. Note that even when a fluid lag exists, it is small compared to R, and gets smaller with time during propagation (Savitski and Detournay 2002). Therefore, we thus further assume that $R_f \approx R$. Therefore, **Eq. (3.13)** can be rewritten as

$$\frac{dR(t)}{dt} \cong \sqrt{-\lambda_p \frac{w(0,t)^2}{12\,\mu_f}\frac{dp_o(t)}{dt}}. \tag{3.14}$$

Eq. (3.14) can be discretised and applied to laboratory measurements of wellbore pressure $p_o(t)$ during fracturing (see **Fig.3.3**), i.e.,

$$\frac{\Delta R}{\Delta t} \cong \sqrt{-\lambda_p \frac{w(0,t)^2}{12\,\mu_f}\frac{\Delta p_o}{\Delta t}} \tag{3.15}$$

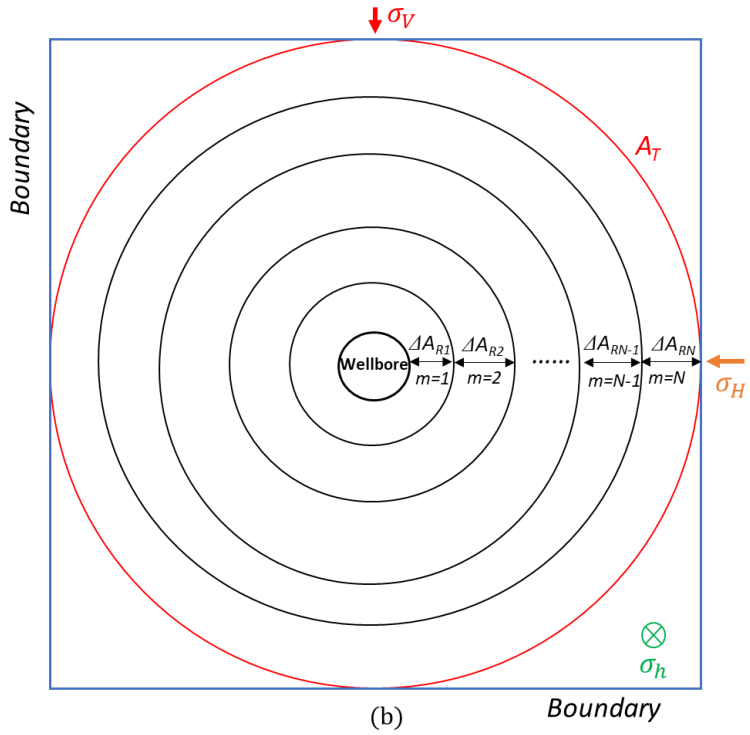

Fig.3.2 2D schematic of the homothetic evolution of the radial fracture, outlining the temporal fracture surface area A_d.

Experimental results reported in the literature suggest that laboratory-scale transverse or longitudinal hydraulic fractures in low permeability rocks are approximately penny-shaped (Bunger 2005; Lhomme 2005; Rodriguez and Stanchits 2017; Sarmadivaleh 2012). In this context, the total time-cumulated volume of incompressible fluid injected into the fracture propagating from the wellbore by the end of propagation, i.e., when $R = R_T$, is $V_T = 2\pi \int_0^R w(0,t)\, r\, dr = \pi\, w(0,t)\, {R_T}^2$. Similarly, the time-cumulated volume at any time t, when the fracture reaches a radius $R(t) < R_T$ during propagation, is related to the average (constant) injection flow rate Q_{in} by

$$V(t) = 2\pi \int_0^R w(0,t)\, R\, dR = \pi\, w(0,t)\, R^2 = w(0,t)\, A_R = Q_{in} t\,, \tag{3.16}$$

where $A_R = \pi\, R^2$ is the fracture's surface area at time t. For a self-similar (homothetic) propagation of the penny-shaped fracture, for a small enough incremental increase in fracture surface area $(\Delta A_R)_m$ per time increment Δt_m, and noting that $\frac{dA_R}{dt} = 2\pi R\, \frac{dR}{dt}$, **Eq.(3.15)** becomes

$$\frac{(\Delta A_R)_m}{\Delta t_m} \cong 2\pi R_m \sqrt{\lambda_p} \sqrt{-\frac{{w_m}^2}{12\mu_f}\left(\frac{\Delta p_o}{\Delta t}\right)_m}\,, \text{ with } 1 \le m \le N, \tag{3.17}$$

where $2\pi\, R_m$ is the circumference of the homothetic moving boundary of the growing penny-shaped fracture (**Fig.3.2**), w_m is the width (aperture) of fracture at the time step m, i.e., w_m (0,m); and N is the total number of time increments. **Eq. (3.17)** indicates that $(\Delta A_R)_m$ is proportional

to $\sqrt{-\frac{{w_m}^2}{12\mu_f}\left(\frac{\Delta p_o}{\Delta t}\right)_m}$, where a new proportionality coefficient $\lambda_m(t) = 2\pi R_m\,\Delta \mathrm{t_m}\,\sqrt{\lambda_p}$ and an intercept B_m are introduced so that

$$(\Delta A_R)_m \cong \lambda_m(t)\sqrt{-\frac{{w_\mathrm{m}}^2}{12\mu_f}\left(\frac{\Delta p_o}{\Delta t}\right)_\mathrm{m}} + B_m, \text{ with } 1 \le m \le N. \tag{3.18}$$

Let A_T be the total (maximum) fractured area, obtained when the fracture reaches the boundaries of the rock sample, where $R = R_T$. The time-dependent area ratio $(\Delta A_R)_m/A_T$ reads

$$\frac{(\Delta A_R)_m}{A_T} \cong \frac{\lambda_m(t)\sqrt{-\frac{{w_\mathrm{m}}^2}{12\mu_f}\left(\frac{\Delta p_o}{\Delta t}\right)_m} + B_\mathrm{m}}{\sum_{i=1}^{N}\left(\lambda_i(t)\sqrt{-\frac{{w_i}^2}{12\mu_f}\left(\frac{\Delta p_o}{\Delta t}\right)_i} + B_i\right)}, \text{ with } 1 \le i \le N \text{ and } 1 \le m \le N \tag{3.19}$$

where the indices i and m reflect the time steps between the nucleation ($i = m = 1$) and the end of propagation ($i = m = \mathrm{N}$) of the hydraulic fracture, i.e., when it reaches the boundaries of the rock sample. Fitting **Eq.(3.18)** to the fracture growth data published in the literature, we observe that $\lambda_m(t) \cong \lambda$ is approximately constant for a given propagation experiment, and that B_m is negligibly small, i.e., $B_m << (\Delta A_r)_\mathrm{m}$ (see details in **Section 3.3**). Therefore, **Eq. (3.19)** can be approximated by

$$(\Delta A_R)_m \cong \frac{A_T\sqrt{-\frac{{w_\mathrm{m}}^2}{12\mu_f}\left(\frac{\Delta p_o}{\Delta t}\right)_m}}{\sum_{i=1}^{N}\sqrt{-\frac{{w_i}^2}{12\mu_f}\left(\frac{\Delta p_o}{\Delta t}\right)_i}}, \text{ with } 1 \le i \le N \text{ and } 1 \le m \le N \tag{3.20}$$

Finally, the cumulative increase in fracture area with time, A_d between fracture nucleation, $m = 1$ and a later time step, $m = n$ (where $n \le N$) reads (see **Fig.3.2**)

$$A_d \cong \sum_{\mathrm{m}=1}^{n}(\Delta A_R)_m = A_T\frac{\sum_{\mathrm{m}=1}^{n}\left(\sqrt{-\frac{{w_\mathrm{m}}^2}{12\mu_f}\left(\frac{\Delta p_o}{\Delta t}\right)_m}\right)}{\sum_{i=1}^{N}\left(\sqrt{-\frac{{w_i}^2}{12\mu_f}\left(\frac{\Delta p_o}{\Delta t}\right)_i}\right)}, \text{ with } 1 \le i \le N \text{ and } 1 \le m \le n \le \mathrm{N} \tag{3.21}$$

Furthermore, **Eq.(3.14)** indicates that w is proportional to $\frac{dR}{dt}$ where the Poiseuille's law (**Eq.3.8**) is still valid when the energy dissipation is dominated by fluid flow within the fracture (Garagash and Detournay 2000; Garagash 2019; Peck et al. 2018). In contrast, when the part of energy dissipation is dominated by cohesive-zone effects near the tip region (Garagash 2019; Lhomme 2005; Liu and Lecampion 2021; Sarris and Papanastasiou 2011), (i) the fracture opens smoothly, i.e., w becomes proportional to $\left(\frac{dR}{dt}\right)^{\frac{3}{2}}$, ($w \propto \left(\frac{dR}{dt}\right)^{\frac{3}{2}}$) (Garagash and Detournay 2000;

Garagash 2019), and (ii) the coefficient of proportionality remains the same as for the Poiseuille's fluid condition, i.e., $\sqrt{-\frac{1}{12\,\mu_f}\frac{dp_o}{dt}}$. In this case, **Eq. (3.15)** is replaced by

$$\frac{\Delta R}{\Delta t} \cong \sqrt[3]{-\lambda_p \frac{w^2}{12\,\mu_f}\frac{\Delta p_o}{\Delta t}}, \tag{3.22}$$

and **Eq.(3.21)** is replaced by

$$A_d \cong A_T \frac{\Sigma_{\mathrm{m}=1}^{n}\left(\sqrt[3]{-\frac{w_m{}^2}{12\mu_f}\left(\frac{\Delta p_o}{\Delta t}\right)_m}\right)}{\Sigma_{i=1}^{N}\left(\sqrt[3]{-\frac{w_i{}^2}{12\mu_f}\left(\frac{\Delta p_o}{\Delta t}\right)_i}\right)}, \quad \text{with } 1 \le i \le N \text{ and } 1 \le m \le n \le \mathrm{N} \tag{3.23}$$

For all propagation regimes the equivalent radius of the fracture R_d is defined as

$$R_d = \sqrt{\frac{A_d}{\pi}}. \tag{3.24}$$

3.2.3 Fracture propagation regimes, asymptotic solutions, and the semi-analytical approximate solution for a penny-shaped hydraulic fracture

A dimensionless group, i.e., time scale (t_{om} , t_{mk}), dimensionless toughness (k), and the time scale ratios (χ, Ψ) have been introduced to analyse fracture propagation regimes (Bunger and Detournay 2007; Detournay 2004b; Dontsov 2016; Garagash 2006; Lecampion et al. 2017; Lhomme 2005; Savitski and Detournay 2002). A set of three scaled material parameters were defined by dimensional analysis

$$\begin{aligned} K' &= \left(\frac{32}{\pi}\right)^{\frac{1}{2}} K_{IC}, \\ E' &= \frac{E}{1-v^2} K_{IC}, \\ \mu' &= 12\mu, \end{aligned} \tag{3.25}$$

where K_{IC} is the fracture toughness, E is Young's Modulus, v is Poisson's ratio, and μ is the viscosity of the fluid. For a constant fluid injection rate Q_{in}, a time scale t_{mk} is defined as the time required for fracture propagation to evolve from a viscosity-dominated regime at early times to a toughness-dominated one at larger times, i.e.,

$$t_{mk} = \left(\frac{\mu'^5 Q_{in}^3 E'^{13}}{K'^{18}}\right)^{\frac{1}{2}}, \tag{3.26}$$

and a dimensionless toughness k is introduced for discriminating the two propagation regimes, i.e.,

$$k = K'\left(\frac{t^2}{\mu'^5 Q_{in}^3 E'^{13}}\right)^{\frac{1}{18}}. \tag{3.27}$$

When $k \leq 1$, the propagation regime is viscosity dominated; while for $k \geq 3.5$, the regime is said to be toughness dominated (Savitski and Detournay 2002).

A time scale ratio χ is also introduced to capture the transition from the early-time fracture initiation driven by the compressibility of the injection system, to the large-time steady propagation at a constant injection rate Q_{in} (Lecampion et al. 2017), i.e.,

$$\chi = \frac{E'^4 {Q_{in}}^{3/2} {\mu'}^{3/2}}{K'^6 U^{1/2}}, \tag{3.28}$$

where U is the volumetric compliance of the injection system, i.e., combined compressibility of the fluid and the pumping system. A time scale t_{om} is also introduced in relation to the coalescence of the fluid front and fracture tip, when the fluid lag goes to zero, i.e.,

$$t_{om} = \frac{E'^2 \mu'}{{\sigma_o}^3}, \tag{3.29}$$

where σ_o is the compressive stress orthogonal to the fracture surface. A second time scale ratio Ψ is introduced for the transition from the viscosity-dominated regime driven by fluid lag, to the large-time propagation regime where fluid front and fracture tip are nearly coincided (Lecampion et al. 2017)

$$\Psi = \frac{t_{mk}}{t_{om}} = \left(\frac{E'^{3/2} {Q_{in}}^{1/2} {\mu'}^{1/2} \sigma_0}{K'^3}\right)^3. \tag{3.30}$$

Garagash (2015), Garagash (2019), and Liu and Lecampion (2021) showed that (see summary in **Table 3.2)**

(i) If $k < 1$ and $\Psi >> 1$, the fracture propagates in a viscosity-dominated regime with significant fluid lag (**Fig.3.1b**); in this situation Poiseuille's flow law is valid, and **Eqs. (3.21) and (3.24)** can be used to estimate A_d and R_d, respectively;

(ii) If $1 \leqslant k \leqslant 3.5$ and $\Psi << 1$, the fracturing fluid invades the process zone (**Fig.3.1c**), resulting in local turbulent flow and slight deviation from Poiseuille's flow law (Liu and Lecampion 2021); in this situation **Eqs. (3.23) and (3.24)** can be used to estimate A_d and R_d, respectively;

(iii) If $1 \leqslant k \leqslant 3.5$ and $\Psi >> 1$, the ratio of confining stress to cohesive stress, σ_o/σ_c, becomes critical. A large σ_o/σ_c ratio accelerates the penetration of the fluid into the cohesive zone, and is modelled as inversely proportional to the size of the fluid lag zone (Garagash 2019; Liu and Lecampion 2021). For instance, the numerical results reported by (Liu and Lecampion 2021) suggest that for a dimensionless toughness $k = 2$, the fluid fraction ζ ranges from 0.85 to 0.98 when σ_o/σ_c ranges from 1 to 10. In this situation, the ratio between the size of the fluid lag and that of the cohesive

zone is relatively small. Therefore, we argue that this situation is similar to case **(ii),** and **Eqs. (3.23) and (3.24)** can be used to estimate A_d and R_d, respectively;

(iv) If $k > 3.5$, a strongly toughness-dominated propagation regime, the fluid lag-to-cohesive zone size ratio is also small (Bunger et al. 2013; Liu and Lecampion 2021). In this situation, a relatively large amount of fluid invades the anticipated large cohesive zone, especially for a low σ_o/σ_c ratio (Liu and Lecampion 2021). We again argue that in this situation **Eqs. (3.23) and (3.24)** can be used to estimate A_d and R_d, respectively;

(v) The aforementioned conditions **(i)-(iv)** only apply to conventional rocks for which the peak tensile stress (cohesive strength) lies in the range 2MPa to 12MPa (Rybacki et al. 2015). In contrast, for brittle materials like PMMA or glass, the tensile strength lies in the range 60 to 70MPa (Zhou et al. 2018), resulting in a very limited extent of the cohesive zone (Garagash 2019). Therefore, for PMMA or glass, **Eq. (3.21)** is used instead of **Eq. (3.23)** for quantifying A_d.

Table 3.2 Fracture propagation regimes and validity of Poiseuille law

Condition	Propagation regime	Fluid Lag	Poiseuille law	Equation for A_d model
$k < 1$, $\Psi >> 1$	Viscosity dominated	Significant	Valid	**Eq.(3.21)**
$1 \le k \le 3.5$, $\Psi << 1$	Transitional	Minor	Invalid	**Eq.(3.23)**
$1 \le k \le 3.5$, $\Psi >> 1$, $\sigma_o/\sigma_c > 1$	Transitional	Minor	Invalid	**Eq.(3.23)**
$k > 3.5$	Toughness dominated	Minor	Invalid	**Eq.(3.23)**
PMMA	Toughness dominated	Minor	Valid	**Eq.(3.21)**

The analytical asymptotic solutions of radius for a radial hydraulic fracture reads for viscosity dominated regime (Savitski and Detournay 2002; Detournay 2004b; Chen et al. 2017):

$$R_V = R(t) = 0.696 \left(\frac{E'}{\mu' Q_{in}}\right)^{\frac{1}{9}} (Q_{in}t)^{4/9} \tag{3.31}$$

And for toughness dominated regime:

$$R_T = R(t) = (\frac{3}{\sqrt{2}\pi})^{\frac{2}{5}} \left(\frac{E'}{K'}\right)^{\frac{2}{5}} (Q_{in}t)^{\frac{2}{5}} \tag{3.32}$$

Eq.(3.31) defining R_V, or **Eq.(3.32)** defining R_T , also called vertex solution, are used for fracture radius predictions under the limiting regimes of propagation (Detournay 2016; Dontsov 2016). Therefore, a semi-analytical approximate solution capturing the transitions

among different vertex solutions are developed by Dontsov (2016), based on the approximation for the fracture width:

$$w(r,t) = \left(\frac{R+r}{2R}\right)^{\lambda} w_a(R-r) \tag{3.33}$$

Where w_a is the tip asymptotic solution, in addition to distance to the tip R-r, λ is a parameter determined based on the numerical evaluation.

And for the equation of global fluid balance:

$$w_a(R)\int_0^1 \left(\frac{1+\rho}{2}\right)^{\lambda}(1-\rho)^{\bar{\delta}}\rho d\rho + 2C't^{0.5}\int_0^1 \sqrt{1-\rho^{\frac{1}{\alpha}}}\rho d\rho = \frac{Q_{in}t}{2\pi R^2} \tag{3.34}$$

where $\rho=r/R$ denotes the scaled spatial coordinate. $\bar{\delta}$ is a varying function for $w_a(R-r) \propto (R-r)^{\bar{\delta}}$. Details of this semi-analytical model can be found in Dontsov (2016). We will also us this model to quantify the temporal fracturing radius (R_S). In this study, the models introduced earlier (R_E R_d, R_V, R_T, and R_S) will be compared to the experimental data (R_{EXP}).

3.3 Validation of the homothetic fracture propagation model (R_d)

3.3.1 Experimental input data

We use the literature data recorded during hydraulic fracturing experiments conducted on synthetic rock analogues subjected to true triaxial stress conditions, i.e., cement/sand blocks from De Pater et al. (1994a), and tight sandstone blocks (Colton and Felser) from Lhomme (2005). Additionally, data from two PMMA blocks subjected to biaxial stresses are also considered as a brittle/homogeneous end-member (Bunger et al. 2013). These data sets include simultaneous monitoring of wellbore pressure, fracture radius, and strains (width at the wellbore) induced by hydraulic fracturing. More details of measurement of these parameters can be found in Lhomme (2005). The measured parameters, e.g., maximum fractured area of the sample (A_T), fluid viscosity (μ_f), wellbore pressure (p_o), and width (w_m) will be fitted into the model (**Eqs.21 or 23**) for computing the temporally fractured area (A_d); then the calculated A_d will be compared to the temporal fracturing area measured from experiments (e.g., **Figs.4-7**).

As shown in **Table 3.3**, the propagation of hydraulic fractures can be classified as stable or unstable based on the experimental conditions (Bunger et al. 2013; De Pater et al. 1994a; Lhomme 2005). The permeability of Colton 08 and 09 ranges from 0.15 to 0.3 mD, while it is one order of magnitude lower for Cov12c, i.e., ~ 0.02mD; fluid leak-off through the fracture walls is therefore very limited for the typical duration of a laboratory hydraulic fracturing

experiment. However, the permeability of the Felser sandstone samples is in the range 2 to 5 mD, which implies that pressurized fracturing fluid can leak into the pore space of the sample during the experiment (Lhomme 2005). Based on their petrophysical properties, the seven rock samples are classified into four groups: (i) stable fracture propagation limited leak-off, i.e., Cov12c and Colton 08; (ii) stable fracture propagation with moderate leak-off, i.e., Felser 02; (iii) unstable fracture propagation limited leak-off, i.e., Colton 09, ab5, c11m1; and (iv) unstable fracture propagation with moderate leak-off, i.e., Felser 03.

In the case of a stable fracture propagation (**Fig.3.3a**), the early-time fracture nucleation process dissipates a significant amount of energy, resulting in the fracture propagating at a wellbore pressure much lower than the maximum wellbore breakdown pressure (See Appendix B for correction of the depressurization rate prior to breakdown), and the rate of wellbore pressure drop to zero is relatively small. The fracture radius and width gradually increase to reach a plateau. In the case of an unstable fracture propagation (**Fig.3.3b**), fracture initiation and borehole breakdown always coincide. In this situation, the fracture radius and width increase virtually instantaneously, and the wellbore pressure drops approximately ten-times faster than in the stable case.

Table 3.3 Materials parameters and experimental conditions from literature (Bunger et al. 2013; De Pater et al. 1994a; Lhomme 2005)

	Sample Type	Young's Modulus E (GPa)	Poisson 's Ratio ν (-)	Permeability K (mD)	Confining Stress σ_o (MPa)	Cohesive strength σ_c (MPa)	Propagation Condition	Leak-off
Cov12c	Cement/Sand	24	0.25	0.02	9.7	3.5	Stable	Limit
Colton 08	Very Tight Sandstone	20	0.17	0.15-0.3	10	3	Stable	Limit
Colton 09	Very Tight Sandstone	14	0.17	0.15-0.3	10	3	Unstable	Limit
Felser 02	Tight Sandstone	15	0.2	2-5	10	2	Stable	Yes
Felser 03	Tight Sandstone	15	0.2	2-5	10	2	Unstable	Yes
ab5	PMMA	3.3	0.4	0	0	44	Unstable	No
c11m1	PMMA	3.3	0.4	0	0	44	Unstable	No

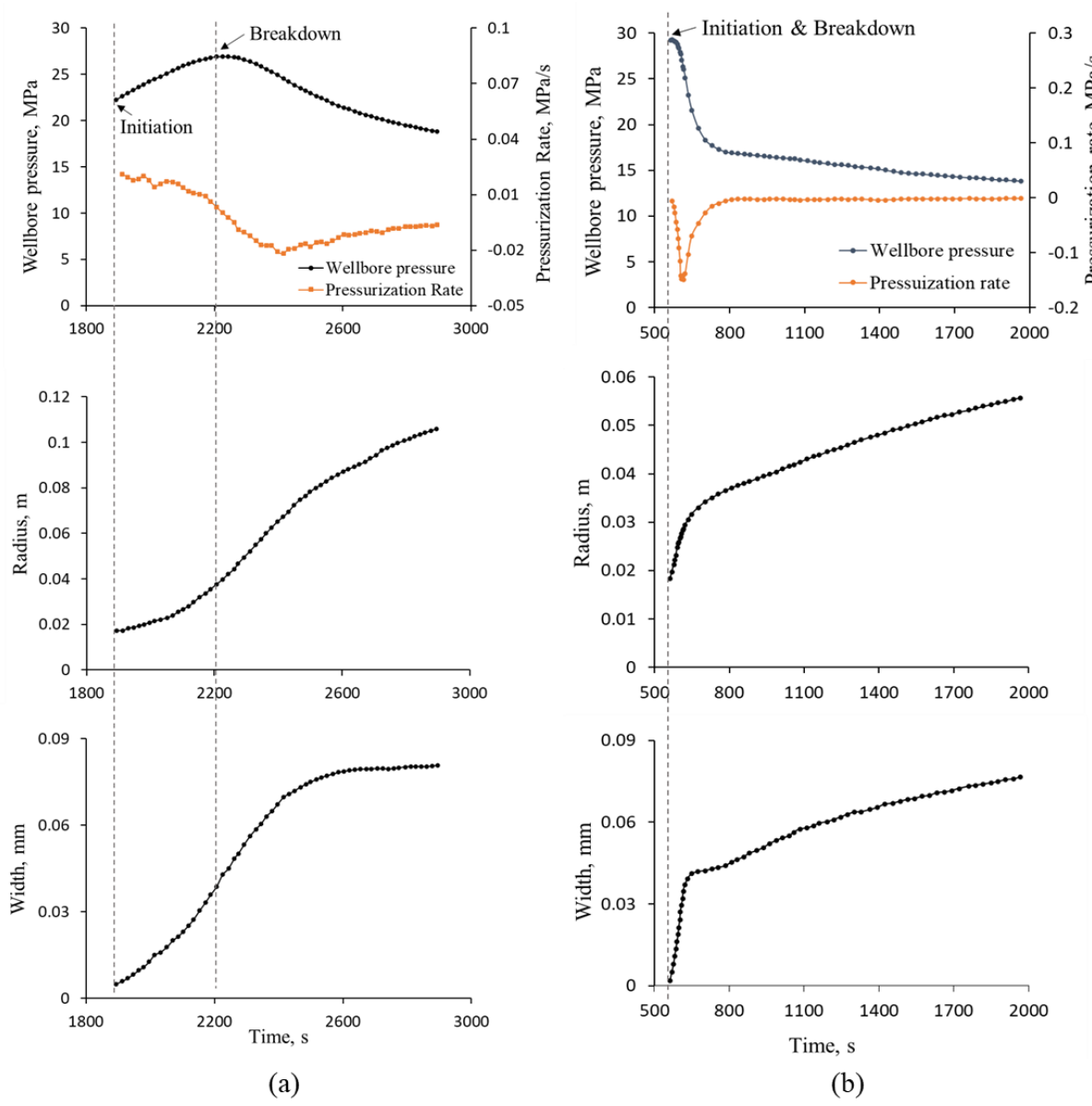

Fig.3.3 Experimental results of wellbore pressure, fracture radius, and width (De Pater et al. 1994b; Lhomme 2005): a) Cov12c, stable propagation and b) Felser 03, unstable propagation

3.3.2 Dimensionless parameters

The values of the time scales t_{mk} and t_{om}, the dimensionless toughness (k), the time scale ratios χ and Ψ, and the ratio of confining stress to cohesive strength (σ_o / σ_c) for each sample are reported in **Table 3.4**. These dimensionless parameters are used here to predict the characteristics of fracture propagation in terms of stability.

3.3.2.1 Stable fracture propagation

- **Sample Cov12c**: The dimensionless toughness $k = 0.43$ indicates that the propagation regime is strongly viscosity-dominated in the far-field conditions (i.e., $t_{mk} >> t_{EXP}$) ; and $\Psi >> 1$ indicates that there is strong fluid lag during propagation. Therefore, **Eqs. (3.21)**

and (3.24) based on Poiseuille's flow law are used for the prediction of the fracture's radius R_d.

- **Sample Colton 08**: The k = 1.20 indicates a transition from a viscosity- to a toughness-dominated propagation regime; and $\Psi << 1$ indicates that fluid lag is very limited during the propagation. Therefore, **Eqs. (3.23) and (3.24)** based on the modified Poiseuille's flow law are used to estimate R_d.
- **Sample Felser 02**: The k = 1.86 also indicates a transition from a viscosity- to a toughness-dominated propagation regime; and Ψ = 215 indicates that fluid lag can occur; however, the relatively large ratio $\sigma_o/\sigma_c = 5$ suggests that the fraction of fluid lag to cohesive zone is relatively small (Liu and Lecampion 2021). Therefore, **Eqs. (3.23) and (3.24)** are again used to estimate R_d.

3.3.2.2 Unstable fracture propagation

- **Sample Felser 03**: The k = 3.4 indicates that the fracture propagation regime is essentially toughness dominated; and $\Psi = 21.5$ implies that fluid lag can occur, although this effect is partly compensated by the relatively large stress ratio $\sigma_o/\sigma_c = 5$, which tends to accelerate fluid flow into the process zone, and reduce the fluid lag-to-cohesive zone ratio. Therefore, **Eqs. (3.23) and (3.24)** are used to estimate R_d.
- **Sample Colton 09**: The k = 3.0 indicates that the fracture propagation regime is essentially toughness dominated; and Ψ = 3.5 and $\sigma_o/\sigma_c = 3.3$ suggest that fluid lag is relatively small during propagation. Therefore, **Eqs. (3.23) and (3.24)** are used to estimate R_d.
- **Samples ab5 and c11m1 (PMMA)**: The $k = 3.5$ for sample ab5, and $k = 5.3$ for sample c11m1 indicate that the fracture propagation regime is essentially toughness dominated (i.e., $t_{EXP} >> t_{mk}$). These experiments were conducted in the laboratory under the condition $\sigma_o/\sigma_c = 0$ to allow for high-resolution monitoring of the propagation with a high-speed camera through the transparent PMMA samples. In this situation, fluid lag was not observed during propagation (Bunger 2005a; Bunger et al. 2013). Numerical simulations also suggest a very limited fluid lag (Liu and Lecampion 2021). It is worth noting that the tensile strength (peak cohesive strength) of PMMA is larger than 60MPa (Zhou et al. 2018), which is orders of magnitude larger than for rocks, resulting in a very limited extent of the cohesive zone in PMMA (Bunger and Detournay 2008; Garagash 2019). Therefore, fluid flow is expected to follow Poiseuille's law, and **Eqs. (3.21) and (3.24)** are used to estimate R_d.

Table 3.4 Key parameters governing the propagation regime of laboratory hydraulic fracturing experiments reported in the literature: Experimental propagation duration (t_{EXP}); compressibility of the injection system (U); dimensionless wellbore radius Λ and notch η_*; time scale of the transition from early-time compressibility-dominated regime to large-time constant flow rate regime $t_{o\hat{}o}$ and $t_{k\hat{}k}$; time scale of the transition from viscosity- to toughness-dominated regime t_{mk}; time scale of the collapse of the fluid lag t_{om}; dimensionless toughness k; time scale ratios χ, Ψ by constant injection rate Q_{in}, and ratio of confining stress to cohesive strength (σ_o/σ_c)

	t_{EXP} (s)	U (m^3/MPa)	Λ	η_*	$t_{o\hat{}o}$ (s)	$t_{k\hat{}k}$ (s)	t_{mk} (s)	t_{om} (s)	k	$\chi = \frac{t_{mk}}{t_{m\hat{}k\hat{}}}$	$\Psi = \frac{t_{mk}}{t_{om}}$	σ_o/σ_c
COV12c	1002	1.5e-07	0.064	0.005	620	250	2.23e+06	1181	0.43	235	1886	2.8
Colton 08	2029	2.4e-07	0.134	0.02	1853	2184	421	2545	1.2	0.37	0.17	3.3
Colton 09	10.6	3.2e-07	0.123	0.02	57	65	18	5	3.0	0.45	3.51	3.3
Felser 02	2466	4.0e-07	0.125	0.02	1365	746	3.15e+05	1465	1.86	38	215	5
Felser 03	1404	4.1e-07	0.124	0.02	134	110	787	37	3.4	3.3	21.5	5
ab5	4.3	N/A	N/A	N/A	N/A	N/A	2.1	0	3.5	N/A	0	0
c11m1	9.2	N/A	N/A	N/A	N/A	N/A	0.1	0	5.3	N/A	0	0

3.3.3 Validation of the fracturing area model (A_d)

Here we validate the model of fracture area A_d using published data detailed in **Section 3.3.1.** Four typical cases are presented in this section:

(i) Stable propagation for a strong viscosity dominated regime (k=0.43) in a tight cement-sand sample, i.e., Cov12c

(ii) Stable propagation for a transitional propagation regime (k=1.2) in a very tight sandstone, i.e., Colton 08

(iii) Unstable propagation for a toughness dominated regime (k=3.0) in a very tight sandstone, i.e., Colton 09

(iv) Unstable propagation for a strong toughness dominated regime (k=5.3) in a linear-elastic material (PMMA), i.e., C11m1.

Note that the results for the other PMMA sample ab5 are similar. For sake of completeness, they are reported in **Appendix C.1**. For the Felser 02 and 03 samples where the propagation of hydraulic fracture is affected by the leak-off effect (Lhomme 2005), the validation is additionally reported in **Appendix.C.1and C.3**.

3.3.3.1 Stable fracture propagation (Limited leak-off)

Cov12c:

The evolution of the fracture area with time $A_d(t)$ in the cement-sand sample measured by (De Pater et al. 1994b) and predicted with the new A_d model are displayed in **Fig.3.4**. **Fig.3.4a** shows that the incremental fracture area per time step $(\Delta A_R)_m$ correlates well with the product $PD_1 = \sqrt{-\frac{{w_m}^2}{12\mu_f}\left(\frac{\Delta p_o}{\Delta t}\right)_m}$. The resulting linear correlation (robust fitting) shown in **Fig.3.4b** validates a posteriori the linearity assumption stated in Section 2.2, i.e.,

$$(\Delta A_R)_m = 3.06 \times 10^3 \times \sqrt{-\frac{{w_m}^2}{12\mu_f}\left(\frac{\Delta p_o}{\Delta t}\right)_m} - 5.55 \times 10^{-7}, \text{ with } R^2 = 0.96 \quad (3.35)$$

where the value of the y-axis intercept $B = -5.55 \times 10^{-7} << (\Delta A_R)_m$. Therefore, **Eq.(20)** can behave closely to **Eq.(3.19)**. Considering this correlation, the time evolution of the dimensionless parameter of relative change in fracture area ${(\Delta A_R)_m}/{A_T}$ and the fraction $\sqrt{-\frac{{w_m}^2}{12\mu_f}\left(\frac{\Delta p_a}{\Delta t}\right)_m} \Big/ \sum_{i=1}^{N}\sqrt{-\frac{{w_i}^2}{12\mu_f}\left(\frac{\Delta p_a}{\Delta t}\right)_i}$ are calculated and shown in **Fig.3.4c**, indicating a reasonably robust fit, despite some measurement-induced fluctuations in ${(\Delta A_R)_m}/{A_T}$. Finally, **Fig.3.4d** compares the predicted evolution of the fracturing area A_d (red triangles) and the experimental data (black dots).

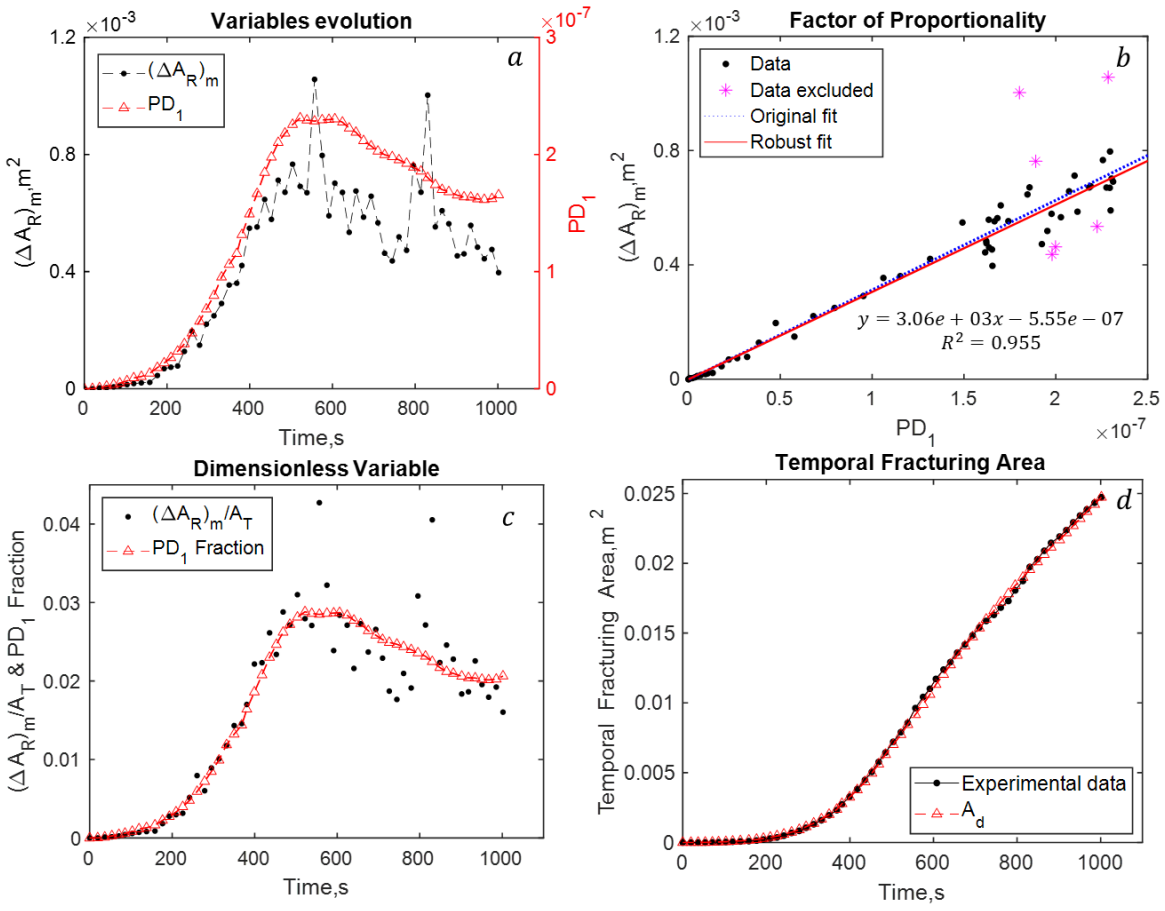

Fig.3.4 Evolution of the fracture area for the cement/sand sample during stable propagation; Comparison between direct laboratory measurements and predictions of the new model presented here.

Colton 08:

The evolution of the fracture area with time in the Colton 08 sample experimentally measured by Lhomme (2005) and analytically predicted by our A_d model is presented in **Fig.3.5**. The aforementioned dimensionless parameters suggest that cohesive zone effects are significant in the Colton sandstone (Garagash 2019; Lhomme 2005), which is accounted for in **Eqs.3.22 and 3.23** for the Colton 08 sample. Similar to Cov12c, we obtain a reasonably good linear correlation (**Fig.3.5b**):

$$(\Delta A_R)_m = 15.59 \sqrt[3]{-\frac{w_m{}^2}{12\mu_f}\left(\frac{\Delta p_o}{\Delta t}\right)_m} - 8.24 \times 10^{-6}, \text{ with } R^2 = 0.9 \qquad (3.36)$$

A good fit is also observed between our analytical prediction and the experimental measurement data in terms of fracturing area growth with time (see **Fig.3.5c** and **d**).

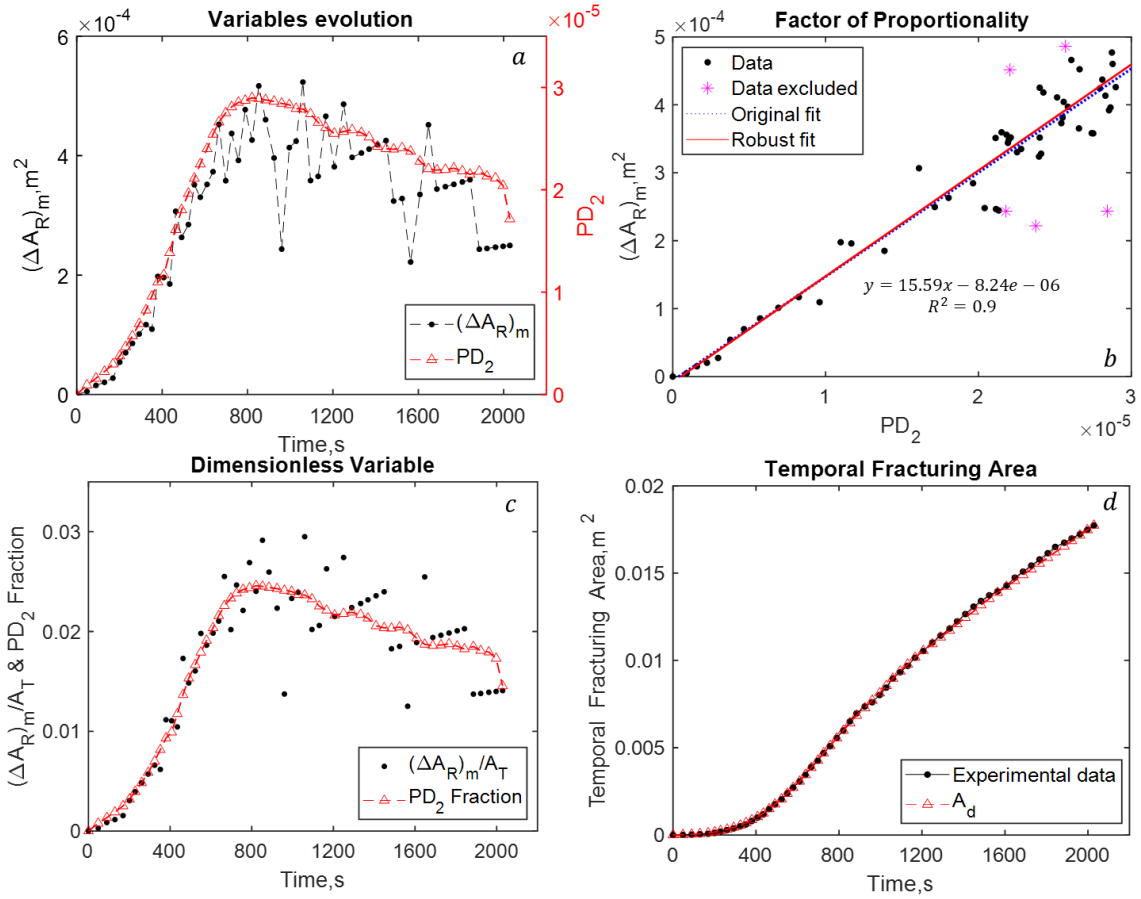

Fig.3.5 Evolution of the fracture area for the Colton 08 sandstone sample during stable propagation; Comparison between direct laboratory measurements and predictions of the new model presented here.

3.3.3.2 Unstable fracture propagation

Here we validate the model of fracturing area A_d for an unstable propagation using published data detailed in **Section 3.1**, i.e., **Colton 09 and c11m1** samples for which the leak-off is negligible.

Colton 09 and c11m1:

The evolution of the fracture area with time measured by Lhomme (2005) in the Colton 09 sample, and by Bunger et al. (2013) in the PMMA sample c11m1, along with the predictions of the new A_d model are shown in **Fig.3.6** and **Fig.3.7**, respectively. Analogously to the case of stable propagation, we obtain reasonably good linear correlations, i.e.,

$$(\Delta A_R)_m = 0.14 * \sqrt[3]{-\frac{w_m^2}{12\mu_f}\left(\frac{\Delta p_o}{\Delta t}\right)_m} - 2.28e-07, \text{ with } R^2 = 0.95 \quad (3.37)$$

for the Colton 09 sample, and

$$(\Delta A_R)_m = 1.35 * \sqrt{-\frac{w_m^2}{12\mu_f}\left(\frac{\Delta p_o}{\Delta t}\right)_m} - 1.37e-08, \text{ with } R^2 = 0.92 \quad (3.38)$$

for the PMMA c11m1 sample.

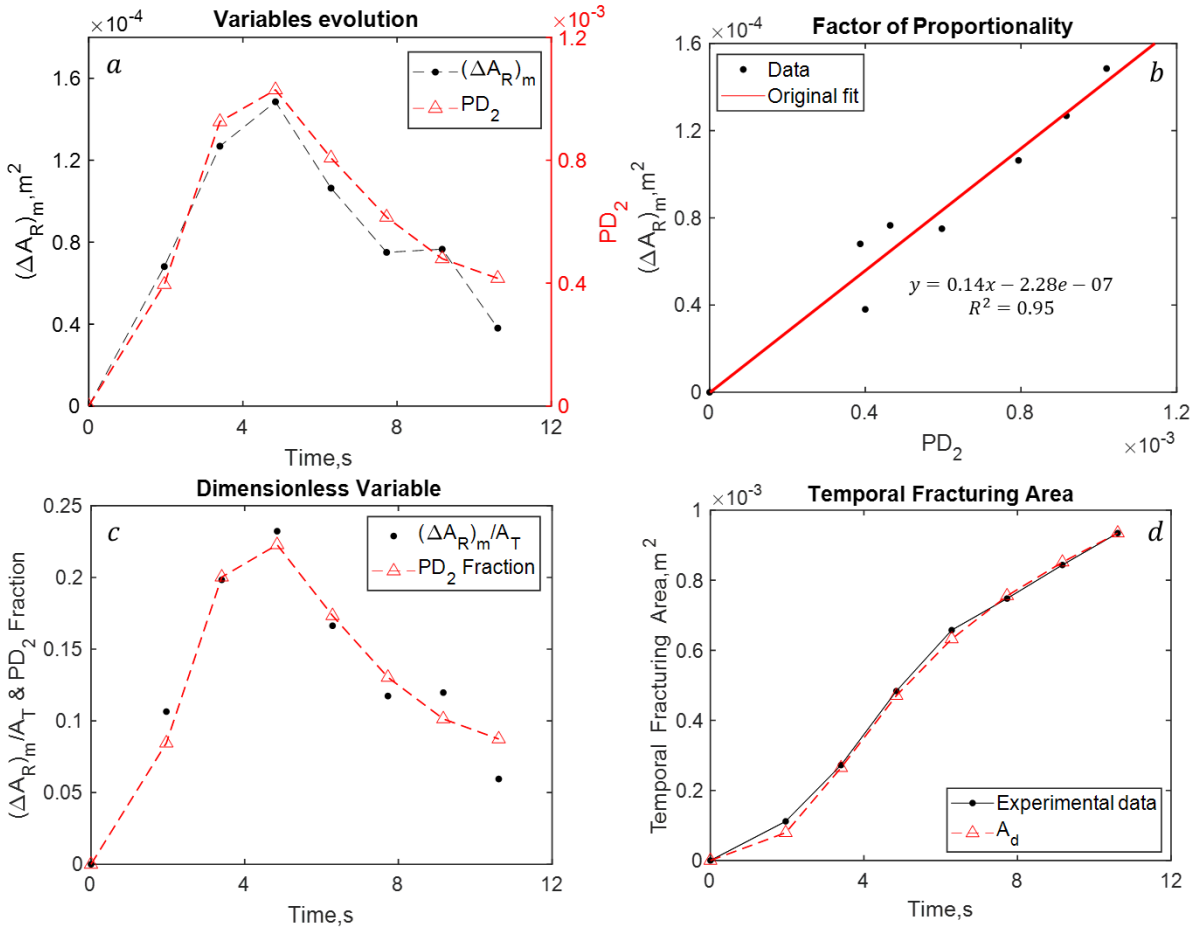

Fig.3.6 Evolution of the fracture area for the Colton 09 sandstone sample during unstable propagation; Comparison between direct laboratory measurements and predictions of the new model presented here.

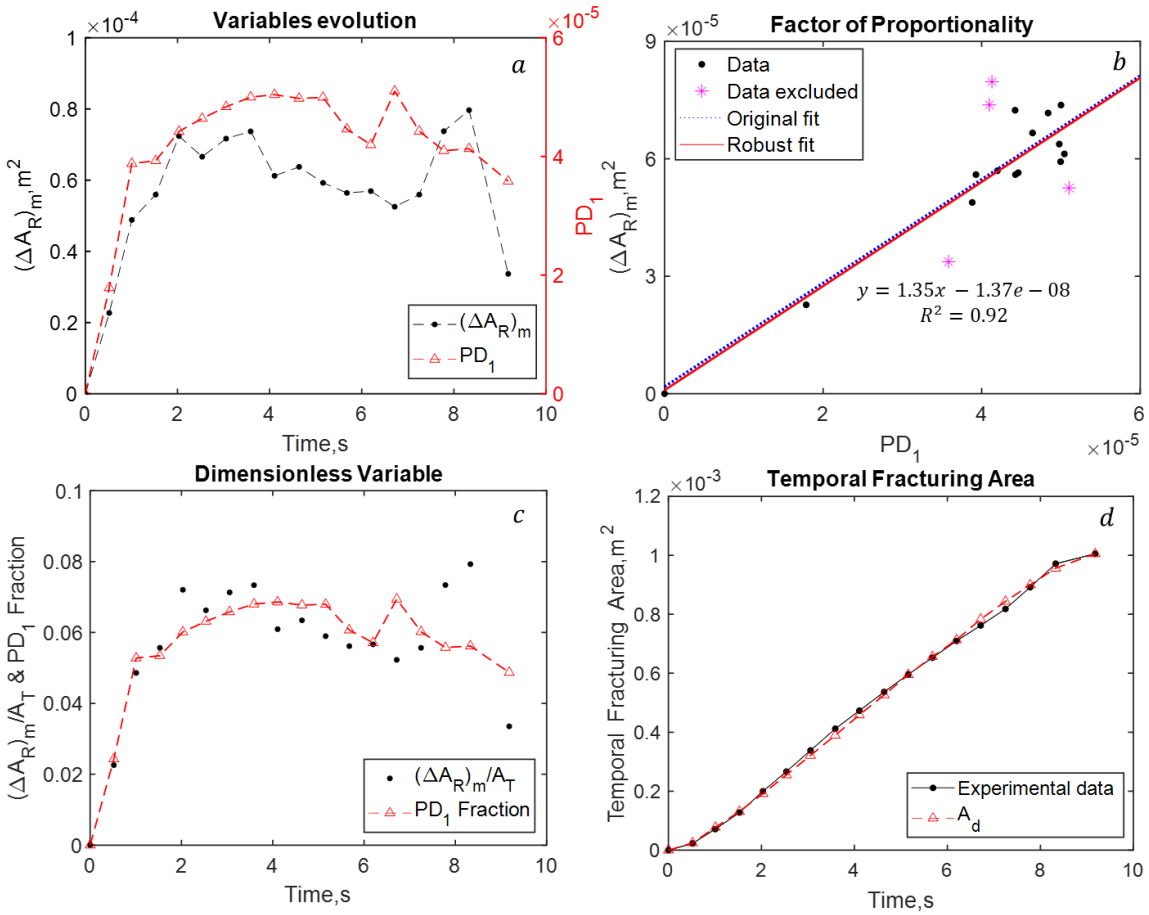

Fig.3.7 Evolution of the fracture area for the PMMA sample c11m1 during unstable propagation; Comparison between direct laboratory measurements and predictions of the new model presented here.

3.4 Comparison between fracturing models

For the seven samples detailed in **Table 3.3**, we compare here the radius predictions of (i) the linear elastic fracture model R_E in **Eq.3.7;** (ii) the asymptotic solutions, i.e., viscosity-driven R_V in **Eq.3.28**, and toughness-driven R_T in **Eq.3.29**; (iii) the semi-analytical approximation R_S in **Eq.3.34;** and (iv) the new homothetic fracture growth R_d in **Eqs.3.21 and 3.24**, or **3.23 and 3.24**, depending on whether cohesive-zone effects are significant.

3.4.1 Stable fracture propagation

3.4.1.1 Limited leak-off

We report here the comparison between the model predictions and the experimental data for the cement/sand sample **Cov12c** (viscosity-dominated fracture propagation experiment), and one ultra-tight sandstone sample **Colton 08** (transited fracture propagation regimes). The time

evolution of the fracture radius as predicted by the four models R_V, R_T, R_S, R_E and R_d are compared to the experimentally-estimated radius in **Fig.3.8**.

For sample **Cov12c** (**Fig.3.8a**), the predicted radius R_E slightly over-estimates the measured fracture radius at early time (T < 200s), but slightly under-estimates it when t > 400 s. For **Colton 08** (**Fig.3.8b**), the predicted radius R_E is in relatively good agreement with experimental data when T < 600 s, but significantly overestimates the measured fracture radius after 600 s. The radius predicted by the asymptotic solutions R_V and R_T (viscosity- and toughness-driven, respectively) significantly overestimates the experimental measurements, although this discrepancy fades with time, i.e., t > 500 s. The semi-analytical solutions R_S improves the accuracy of the prediction (i.e., the line shifts towards the experimental data). However, the predicted radius and experimental data are only in good agreement at the late time (e.g., t > 800 s), a significant discrepancy still exists for the early-time propagation. On the other hand, for both samples **Cov12c** (**Fig.3.8a**) and **Colton 08** (**Fig.3.8b**) the predicted radius R_d agrees well with experimental data for the entire propagation period.

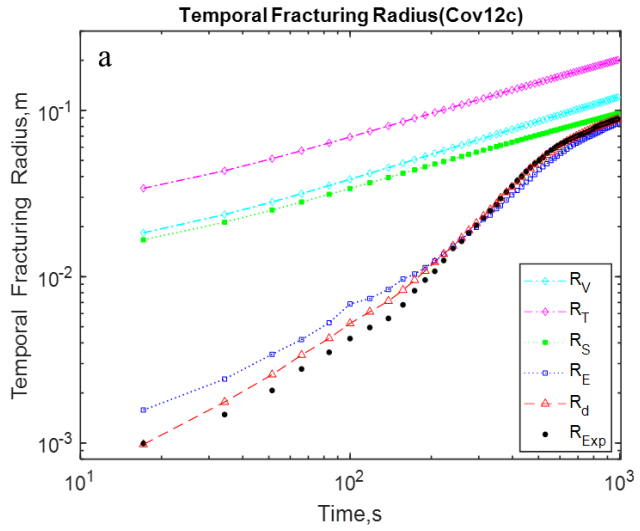

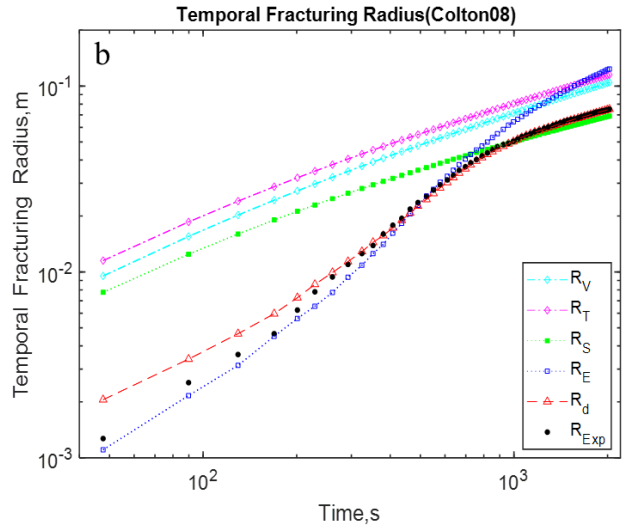

Fig.3.8 History match of experimental fracturing radius based on asymptotic solution (R_V and R_T), semi-analytical solution (R_S), linear elastic theory (R_E), and R_d models: a) Cov12c; b) Colton 08

3.4.1.2 Moderate leak-off

We report here the comparison between the model predictions and the experimental data for the **Felser 02** sample (**Fig.3.9**). The predicted radius R_d matches well the experimental data except at early propagation time (i.e., t < 300s), whereas the predicted R_E slightly under-estimates the measured radius for the entire propagation time. The semi-analytical solution R_S overestimates the fracture radius at the early-intermediate time (i.e., t < 1000s), but approaches to the experimental radius (R_{EXP}) at the late-time propagation (i.e., t > 1000s). On the other hand, R_V and R_T significantly over-estimate the experimental data at all times during the hydraulic fracturing experiment. Fluid loss (leak-off) through the fracture's wall during fracturing is a plausible cause for the smaller fracture radius reached at a given time during fracture propagation compared to the predictions of the asymptotic solution (Lhomme 2005). The large-time trend for all models is similar, but the asymptotic solution neglecting leak-off exhibits an offset of about one order of magnitude.

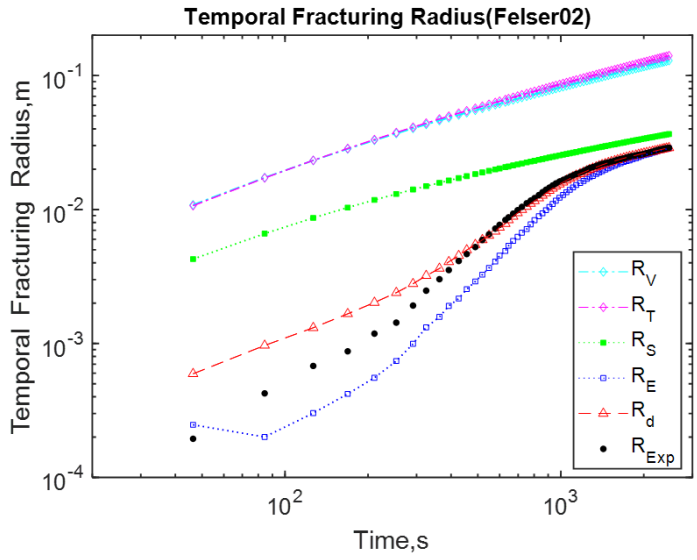

Fig.3.9 History match of experimental fracturing radius based on asymptotic solution (R_V and R_T), semi-analytical solution (R_S), linear elastic theory (R_E), and R_d models: Felser 02

In summary, for a stable fracture propagation (**Fig.3.8 and Fig.3.9**), we observe a better agreement between the R_d model predictions and the experimental data compared to the other two models. Overall, the discrepancies between model and data fade at large time (except for the R_E of **Colton08**), and the large-time trends are approaching to be consistent between data, models, and the semi-analytical solution R_S.

3.4.2 Unstable fracture propagation

We report here the comparison between the model predictions and the experimental data for the ultra-tight sandstone sample **Colton 09** (viscosity-dominated fracture propagation experiment), the two PMMA samples **ab5** and **c11m1** (toughness-dominated fracture propagation experiment) on one hand, and the tight sandstone sample **Felser 03** (toughness-dominated fracture propagation experiment) on the other. The time evolution of the fracture radius as predicted by the four models R_V, R_T, R_S, R_E, and R_d are compared to the experimentally-estimated radius in **Fig.3.10** and **Fig.3.11.**

3.4.2.1 Limited leak-off

For the three samples (**Fig.3.10**), the propagation time is only about 10 seconds to reach a final radius of approximately 0.02m. The R_d model predictions agree well with experimental data. In terms of the consistency, the R_T model predictions show the effectiveness for the PMMA samples (**Fig.3.10b and c**), but exhibit moderate discrepancies for the **Colton09** sample (**Fig.3.10a)**. For these three samples where the propagation of hydraulic fracture is toughness-dominated (see **Table 3.4**) with negligible leak-off effect, the fracturing radius based on models R_T and R_S are well agreed. On the other hand, the predicted R_E radius significantly deviates from the experimental measurements even at the large time for these three samples.

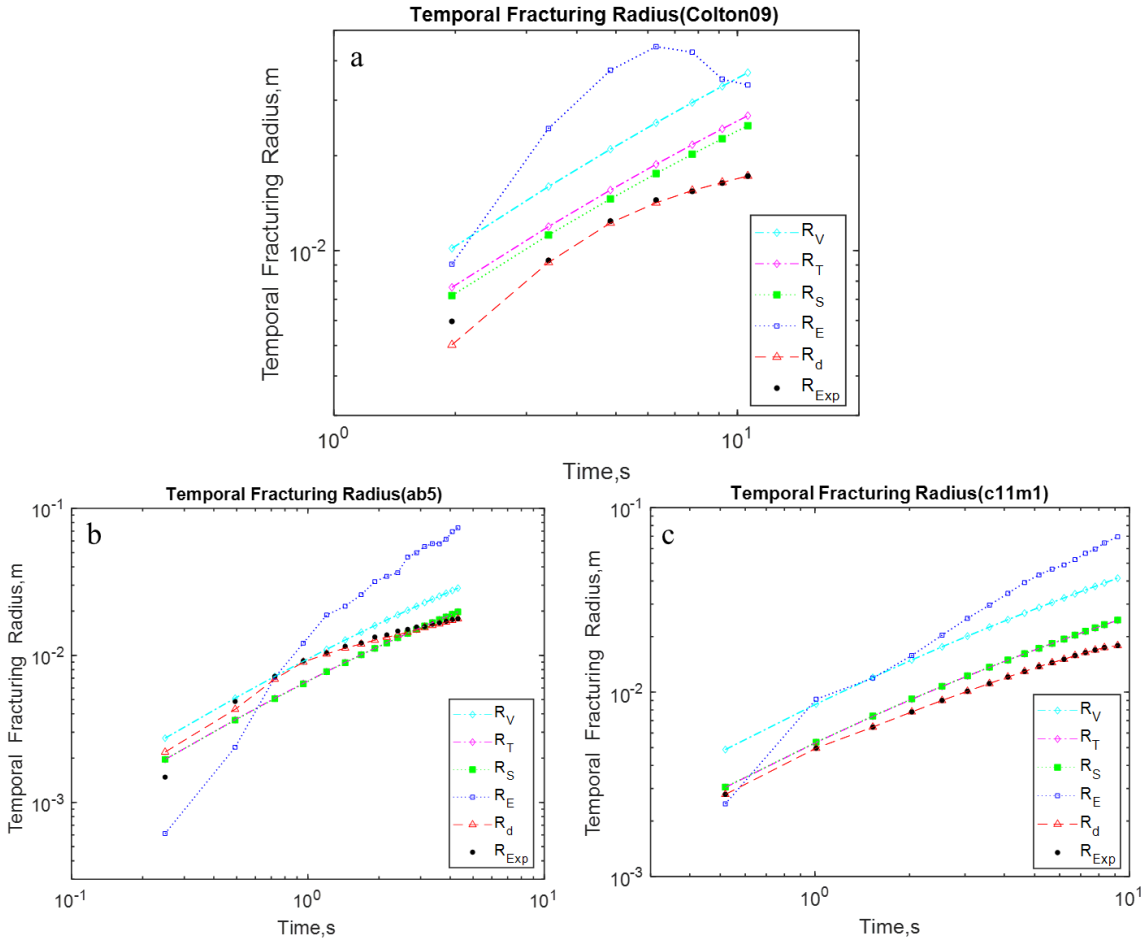

Fig.3.10 History match of experimental fracturing radius based on asymptotic solution (R_T), semi-analytical solution (R_S), linear elastic theory (R_E), and R_d model: a) Colton 09; b) ab5; c) c11m1

3.4.2.2 Moderate leak-off

For the **Felser 03** sample (**Fig.3.11**), the R_d predictions agree well with experimental data. On the other hand, the R_E model slightly under-estimates the experimental data at early time, but becomes more effective at large time. The predictions based on R_V and R_T model significantly over-estimate the experimental radius at all times. The prediction based on model R_S is shown to be moderately deviated from the experimental measurement.

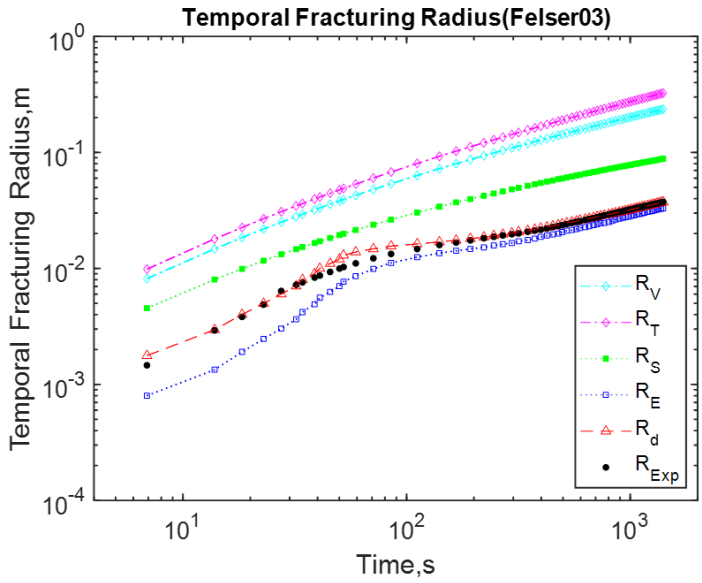

Fig.3.11 History match of experimental fracturing radius based on asymptotic solution (R_T), semi-analytical solution (R_S), linear elastic theory (R_E), and R_d model, and experimental data- Felser 03.

In summary, for unstable fracture propagation, the R_d model predictions compare well with experimental data, whereas the R_E model is significantly less effective for the **Colton 09** and two **PMMAs**. On the other hand, the asymptotic solution (R_T model) is effective for the toughness-dominated fracturing experiments with the PMMA samples, but clearly inadequate for sandstone samples **Colton 09**, and **Felser 03**, regardless of leak-off. For the semi-analytical solution R_S where the leak-off effect is considered in **Colton 09** and **Felser 03**, the accuracy of predictions are improved.

3.5 Discussion and Implications

3.5.1 Incremental increase in fracture area $(\Delta A_R)_m$

The linearity between $(\Delta A_R)_m$ and *PD* (involving the pressure change with time at the fracture inlet/borehole) is an important indicator of a successful R_d model. For both stable and unstable fracture propagation with very limited leak-off, this linearity is evident, resulting in a good agreement of the model with experimental data for most samples for which direct measurement of the fracture radius evolution with time is available in the literature (see **Table 3.*3* and Table 3.*4***, and the **Fig.3.*4*b**, **Fig.3.5b**, **Fig.3.*6*b**, **Fig.3.*7*b**, and **A2b**. On the other hand, when leak-off effects play a moderate role in relatively permeable samples, e.g., Felser 02 in **Fig.C1b** and Felser 03 in **Fig.C3b**, the linear regression between $(\Delta A_R)_m$ and *PD* is less robust, resulting in slight discrepancy between R_d predictions and experimental data. This also supports the linearity between the time-change in fluid pressure at the fluid front and the time-change in

wellbore/inlet pressure at each propagation increment (**Fig.A1**), i.e., $\left.\frac{\partial p_f(r,t)}{\partial t}\right|_{r=R_f} \propto \left(-\left.\frac{dp_f(r,t)}{dt}\right|_{r=o}\right)$.

Porosity may also affect the aforementioned relationship; the more porous the rock, the more irreversible deformation is recorded during hydraulic fracturing according to Holt et al. (2015) or Wong and Baud (2012) for instance. This is qualitatively consistent with the set of samples with different porosity we used in this study, i.e., in the Felser 02 and 03 sandstone samples (Φ = 0.21), the Colton sandstone (Φ = 0.12), and the cement/sand composite Cov12c (Φ = 0.15).

3.5.2 Validity of the Poiseuille flow within hydraulic fracture

Based on the comparison between fracturing models we conducted here (**Sections 3.3** and **3.4**), we confirm that the near-tip cohesive zone plays a critical role during the propagation of a hydraulic fracture in conventional rocks having a tensile strength in the range 2 to 12 MPa when in situ stress conditions at depth induce a high σ_o/σ_c ratio. In the viscosity-dominated propagation regime with significant fluid lag (Cov12c), and where the cohesive zone is embedded in the lag zone (see **Fig.3.*1*b)**, the conventional Poiseuille flow law is shown to be acceptable **(Fig.3.4b)**. In contrast, when a relatively small fraction of fluid lag is embedded in the cohesive zone (**Fig.3.1c for Colton 08 and 09)**, the proportionality between width *w* and fluid velocity *u* must be modified to a fractional power dependence $w \propto (\frac{dR}{dt})^{\frac{3}{2}}$, see **Fig.3.5b and Fig.3.*6*b**. For materials like PMMA with a relatively higher tensile strength (above 60MPa), the impact of the cohesive zone on fracture propagation is very limited, which in turn suggests that the conventional Poiseuille flow law and Linear elastic fracture mechanics (LFEM) can be used under such conditions **Fig.3.*7*b**.

3.5.3 Applicability of the R_v or R_T, R_S, R_E ,and R_d models

The results indicate that the asymptotic solutions (R_v or R_T) are only suitable for the fracturing radius predictions of linearly elastic homogeneous materials, i.e. PMMA (**Fig.3.10b and c**), but significant deviation are observed in the synthetic/natural tight sandstones tested (i.e., Cov12c, Coltons, and Felsers). The semi-analytical solution R_S, accounting for the leak-off effect and the transition among different regimes, improving the accuracy of predictions especially for the late stage under the stable propagation. The prediction performance of the linear elastic model (R_E) is poor for unstable propagation cases (**Fig.3.10**). Although it shows

partial agreement with the data in some cases (**Fig.3.8 and Fig.3.11),** the simplification of the fluid pressure distribution P_f within the fracture (i.e., **Eq.3.9**) leads to unreliable predictions.
The results also show that the new R_d model matches well the experimental data, regardless of the propagation regimes; the stability of the propagation; or whether leak-off is significant. The only consideration is the early-time overestimation of R_d in the stable case with leak-off (**Fig.3.10**). Such a broad applicability is due to the fact that this model is based on a mechanistic approach and involves homothetic growth, dimensional analysis, and direct laboratory observations. This suggests that the R_d model can be robustly applied in the laboratory. It is also probably applicable in the field by extrapolation, which remains to be explored.

3.6 Conclusion and Recommendations

Hydraulic fracture propagation is a complex and coupled process involving fluid-solid interactions, integrating multiscale propagation regimes with stablity conditions to be accounted for under varying stress regimes (e.g., depth, proximity to major tectonic faults, etc.). This siginifcantly challenges our ability to predict/control the propagation of hydraulic fractures, and the fate of fractuing fluids underground.
Based on the experimental data avaliable in the literature (De Pater et al. 1994, Lhomme 2005, Bunger et al. 2013), we thus compere here several models for the prediction of the time-evolution of the radius of the penny-shaped fracture. The first model relies on linear elastic fracture mechanics (R_E); the second is based the Poiseuille's flow law within the fracture and on the assumpion of homothetic fracture growth (R_d); the third is the viscosity-driven or toughness-driven asymptotic fracturing models (R_v or R_T); and the fourth is semi-analytical approximation (R_S).Their applicabilities are assessed against published experimental data, i.e., hydraulic fracturing of five synthetic/natural tight sandstone samples under true tri-axial stress, and two PMMA samples under biaxial stress conditions.
The results show that the cohesive zone plays an important role in hydraulic fracturing for conventional rocks ($2 \leqslant \sigma_c \leqslant 12$MPa): (i) Poiseulle flow within the fracture is valid for propagation in the viscosity-dominated regime ($k<<1$) with siginifcant fluid lag ($\Psi >> 1$); and (ii) when a small fluid lag is embedded within the cohesive zone (**Fig.3.1c**), the proportionalilty $w \propto \frac{dR}{dt}$ must be modified to $w \propto \left(\frac{dR}{dt}\right)^{\frac{3}{2}}$ in the R_d model.
The asymptotic models (R_v or R_T) are limited to linearly elastic homogeneous materials, i.e. PMMA (**Fig.3.10b and Fig.3.10c**). The semi-analytical solution R_S improves the accuracy of predictions, leading to a reliable result for the late-time stable propagation. The (R_E) model

poorly agrees with the experimental data, especially for unstable propagation cases. On the other hand, a good agreement between the results from our R_d model and experimental data indicates that the experimental radius of the hydraulic fracture under true tri-axial stress condition can be properly reconstructed:

(i) The homothetic propagation of radial hydraulic fractures is valid for laboratory-scale experiments.

(ii) Where fracture aperture, wellbore pressure, and the boundaries are obtained from laboratory or field investigations, our R_d model can predict the fracture radius evolution with time in multiple situations (e.g., stable/unstable propagation, leak-off effect). The model is mathematically simple to implement with low computational costs.

(iii) Field assessment of the R_d model is recommended, where the radius predicted from R_d can be applied for the calibration of fracture growth monitoring based on active/passive seismic data interpretation.

II Experiments and Results

Chapter 4
Rock Mechanical and Hydraulic fracturing experiments

4 Rock mechanical and Hydraulic fracturing experiments

This chapter mainly discusses the rock mechanical tests conducted for mechanical properties (parameters), and the hydraulic fracturing (HF) tests conducted in artificial geomaterials exhibiting a wide range of rheology: cubic samples 50x50x50 mm^3 in size are subjected to true triaxial stresses with either a low (σ_v = 6.5 MPa, σ_H =3 MPa, and σ_h =1.5MPa), or a high (15 MPa, 10 MPa, and 5MPa) confinement. The 3D strains induced by hydraulic fracturing are monitored and interpreted. Both experimental data will be used for brittleness index (BI) quantification based on different *BI* models (detailed in **Chapter 5**), as it is shown in **Table 2.1**. The results from HF tests, e.g., fracture geometry, orientation, and fracturing area will be integrated with the BI results (detailed in **Chapter 6**)

This chapter includes a modified content from the following scientific articles:

Feng R., Liu S., Sarout J., Dautriat J., Zhong Z., Rezaee R., Sarmadivaleh M (2022a). Hydraulic fracturing: Laboratory evidence of the brittle-to-ductile transition with depth. Preprint DOI: doi.org/10.31223/X5PH0S

Feng R., Sarout J., Dautriat J., Ghuwainim Y., Rezaee R., Sarmadivaleh M (2022b). Laboratory validation of a new hydro-mechanical energy-based brittleness index model for hydraulic fracturing. Preprint DOI: doi.org/10.31223/X55M1J

Feng R., Zhang Y., Rezagholilou A., Roshan H., Sarmadivaleh M (2020). Brittleness Index: From Conventional to Hydraulic Fracturing Energy Model. *Rock Mechanics and Rock Engineering* 53: 739-753.

4.1 Sample Preparation

To minimise the impact of heterogeneity, bedding, and defects usually found in natural rocks, we used in this study synthetic rock blocks made of silica, clay, and calcite mineral mixtures, with variable relative fractions. These minerals are most commonly found in geological materials in the Earth's crust such as shales, sandstones, and limestones (Iqbal et al. 2022; Luan et al. 2016). Standard Portland cement was added to the mineral mixtures as a bonding agent for its small grain size and low toughness (De Pater et al. 1994a). Blocks were moulded, out of which multiple plugs and cubic samples were extracted after cement curing.

It is noteworthy to mention that a series of synthetic samples were initially made for the preliminary assessment (i.e., to exam the effectiveness of model BI_1 to BI_8). The details of the mineral composition and density of the various mixtures are listed in **Table 4.1**. More details on the samples fabrication procedures can be found in Feng et al. (2020) and Sarmadivaleh and Rasouli (2015).

Table 4.1 Composition and density of the Preliminary four types of synthetic rock (mineral cement mixtures) used in this study.

Mineral-cement mixture	Silica (%)	Kaolinite (%)	Calcite (%)	Cement (%)	Density(g/cm^3)
Quartz-rich(S_1)	52.5%	22.5%	0.0%	25%	1.73
Clay-rich(S_2)	22.5%	52.5%	0.0%	25%	1.46
Calcite-rich(S_3)	15.0%	7.5%	52.5%	25%	1.62
Mixed average(S_4)	30.0%	22.5%	22.5%	25%	1.66

Based on the preliminary results of BI (see details in Feng et al. (2020) and **Chapter 5**), a new series of synthetic samples were made (**Table 4.2)** to effectiveness of the model BI_3, BI_7 , BI_9 , and BI_{10} only. Due to the different brand of materials and vibration technique used between the preliminary and new series of samples, the density (see **Table 4.1 and Table 4.2)** and mechanical properties (see **Table 4.3 and Table 4.4)** are shown to be different. In addition to the mineral-cement mixtures listed in **Table 4.2**, a block of PMMA was used as an ideally homogeneous and brittle rock analogue (Bura and Seweryn 2018; Long et al. 2020).

At least four samples of each mineral-cement mixture were prepared for testing (part of the samples is shown in **Fig.4.1a**). The schematic of a cubic sample assembly during a typical hydraulic fracturing test is shown in **Fig.4.1b**, along with the fluid injection wellbore and casing**.** A vertical 33 mm long wellbore is drilled into the sample, and the casing is introduced and glued to the wellbore down to one-third of the sample's height (17 mm below the sample's top surface), leaving an open hole section of 16 mm. Due to the extremely high tensile strength of PMMA which is above 60MPa (Zhou et al. 2018), the wellbore in the PMMA cubes are notched at half the height of the sample to assist fracture initiation (25 mm below the sample's top surface).

Table 4.2 Composition and density of the NEW five types of synthetic rock (mineral cement mixtures) used in this study.

Mineral-cement mixture	Silica (%)	Kaolinite (%)	Calcite (%)	Cement (%)	Density(g/cm^3)
Quartz-rich(S_1)	52.5%	22.5%	0.0%	25%	1.58
Clay-rich(S_2)	22.5%	52.5%	0.0%	25%	1.26
Calcite-rich(S_3)	15.0%	7.5%	52.5%	25%	1.44
Mixed average(S_4)	30.0%	22.5%	22.5%	25%	1.50
Clay-rich$_2$(S_5)	30.0%	45%	0.0%	25%	1.46

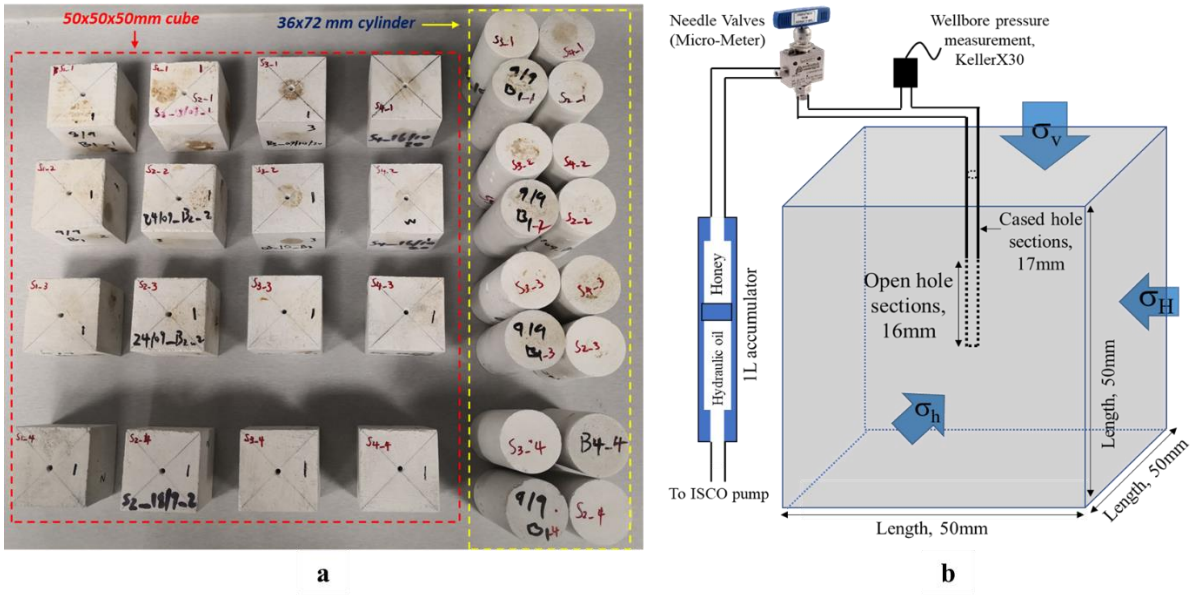

Fig.4.1 a) Part of the synthetic rock samples used in this study: a) 50x50x50mm cubes for hydraulic fracturing, and 36x72mm cylindrical plugs for mechanical characterisation; b) schematic of a typical cubic sample prepared for hydraulic fracturing tests (modified from Feng et al. (2020)).

4.2 Experimental Procedure

4.2.1 Rock mechanical testing

The complete sample set, including mineral-cement mixtures and PMMA, comprises a) 25 cylindrical sample plugs 36 mm in diameter and 72 mm in height, used for estimating the mechanical properties of each material, i.e., 10 unconfined (UCS) and 25 triaxial (TCS) compression tests on dry samples; and b) 25 initially dry cubic samples 50x50x50 mm^3 in size, used for hydraulic fracturing tests under true triaxial stress conditions. The TCS tests were conducted in dry conditions at 0.6, 2.1, and 3.4 MPa confining pressure.

UCS tests (**Fig.4.2a**) were performed on the samples to obtain the mechanical parameters required for the *BI* models (**Table 2.1**) and scaling analysis of *HF* experiment (Feng et al. 2020) (Feng et al. 2020). The measured mechanical properties were uniaxial compressive strength (*UCS*), Young's Modulus (*E*), Poisson's Ratio (*v*) and overall stress-strain response. In addition, compressional (V_p) and shear wave velocity (V_s) (km/s) measured by acoustic instruments (**Fig.4.3**) were used to calculate the dynamic Young's Modulus (E_{dyn}) and Poisson's ratio (Fjaer et al. 2008):

$$E_{dyn} = \frac{\rho V_s^2 (3V_p^2 - 4V_s^2)}{(V_p^2 - V_s^2)} \tag{4.1}$$

$$\upsilon_{dyn} = \frac{V_p^2(V_p^2 - 2V_s^2)}{2(V_p^2 - V_s^2)} \quad (4.2)$$

Due to ultra-low permeability of synthetic samples composed of fine particles of cement, clay and calcite, the porosity ($\emptyset$) measurement using conventional experimental techniques is difficult thus the porosity ($\emptyset$) was alternatively estimated using an empirical equation (Han et al. 1986):

$$\emptyset = \frac{5.59 - 2.18C - V_p}{6.93} \quad (4.3)$$

where, C is the weight percentage of clay, calcite, and cement content of the sample and V_p is the measured compressive wave velocity. E_{dyn} , υ_{dyn} and $\emptyset$ were used for BI_3 calculation.

Brazilian tensile test (*BTT*) is an indirect method to obtain the maximum tensile strength of the rock (σ_T) (He and Hayatdavoudi 2018). The measured tensile strength from *BTT* along with the measured *UCS* were used as input for BI_4 and BI_5 (**Table 2.1**). The tri-axial compressive strength (*TCS*) tests (**Fig.4.2b**) were also carried out to extract the internal friction angle (Φ) and cohesion (C_o) based on the Mohr-Coulomb failure criterion (Roshan et al. 2017) i.e. required by BI_6 model. In addition, the semi-circular bending test (*SCB*) was conducted to obtain the fracture toughness (K_{IC}) (Chong et al. 1987) which was needed for the scaling law (Detournay 2004a) of the hydraulic fracturing test. The equations of K_{IC} proposed by (Chang et al. 2002) was thus used:

$$K_{IC} = \frac{P\sqrt{\pi a}}{Dt} Y_k \quad (4.4)$$

$$Y_k = 4.47 + 7.4\frac{a}{D} - 106(\frac{a}{D})^2 + 433.3(\frac{a}{D})^3 \quad (4.5)$$

Where P is the applied force; a is the length of the notch; D is the diameter and t is the thickness of the sample; Y_k is the geometrical factor estimated by third-order polynomial **Eq. (4.5)**. In the SCB test , the diameter (D) of the sample was 15 cm, length of the notch (a) is 1.9 cm, the distance between two supporting rod (2S) is 12 cm and thickness is 10 cm.

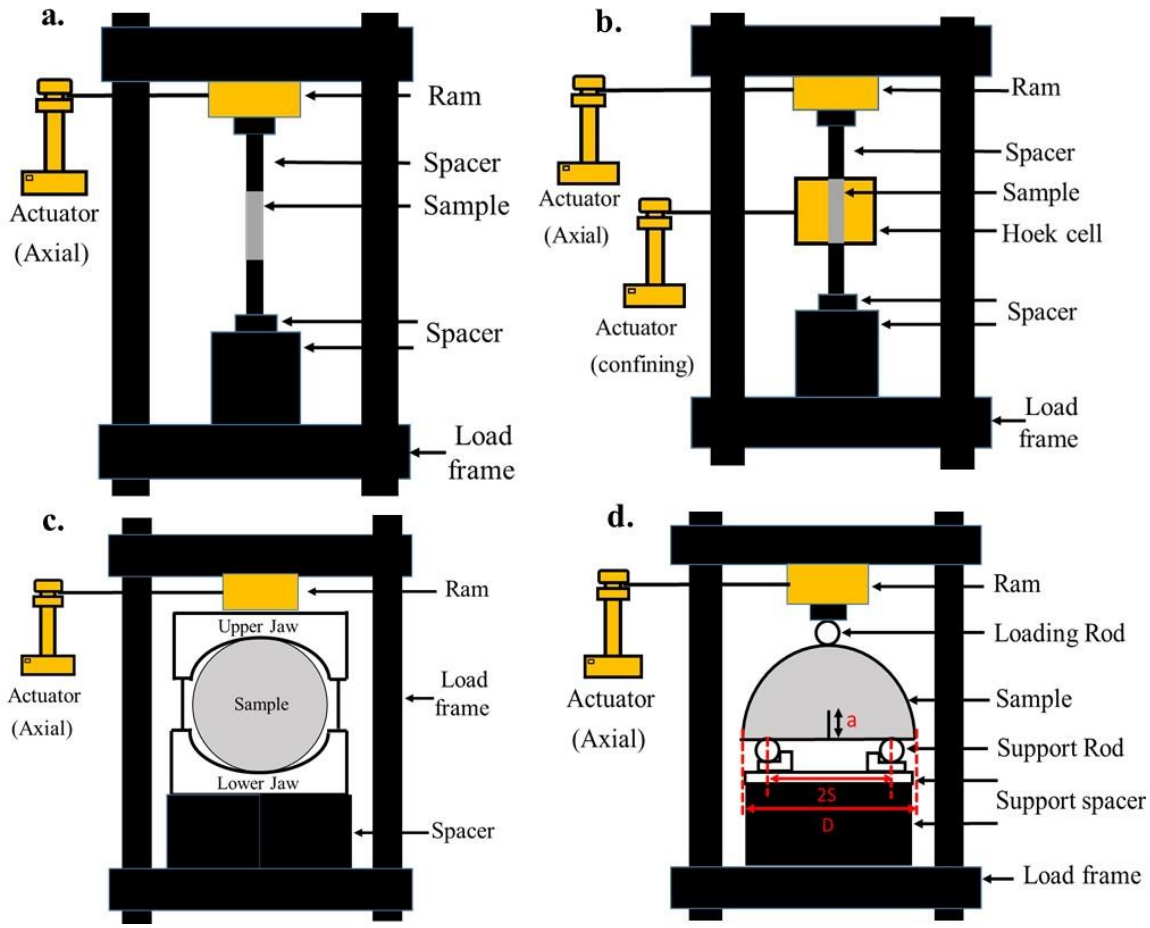

Fig.4.2 Schematic of rock mechanical testing setup: a) Uniaxial compressive strength (UCS) test; b) Tri-axial compressive test (TCS); c) Brazilian tensile test (BTT) and d) Semi-circular bending test (SCB).

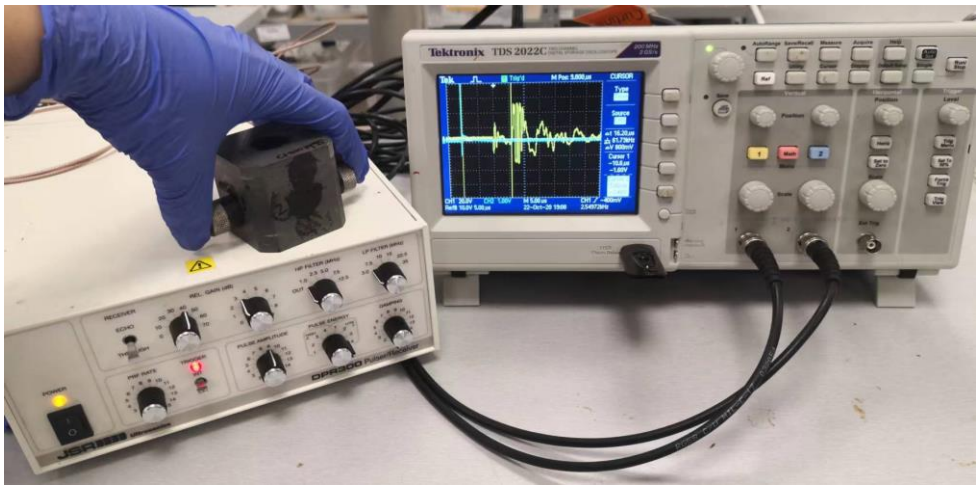

Fig.4.3 Apparatus used for acoustic measurement at ambient condition.

4.2.2 Hydraulic fracturing experimentation

Hydraulic fracturing experiments under true triaxial stress conditions were conducted on a suite of synthetic rocks prepared in **Section 4.1** in order to evaluate the validity and performance of the new cohesive-energy and hydro-mechanical energy-based Brittleness Index model, i.e., BI_9 (**Eq.2.17**) and BI_{10} (**Eq.2.19**). In this section we describe the experimental setup and procedure used for the rock deformation (creep) and hydraulic fracturing experiments. The testing apparatus is shown in **Fig.4.4**. The setup is composed of four key sub-systems:

a) Three independent and mutually orthogonal dual actuators to apply three independent and mutually orthogonal stresses on a cubic rock sample (**Fig.4.4b**).

b) Three hydraulic pumps to supply and independently regulate the hydraulic oil pressure in each dual actuator, and control the stress in that direction; and one additional pump to inject the fracturing fluid into the wellbore-sample assembly (**Fig.4.4a**).

c) Three Linear Variable Differential Transformers (LVDTs) attached to the dual actuators to measure the displacement along each stress direction.

d) A data acquisition system to monitor wellbore pressure with high-sensitivity pressure transducers (Keller X30) (**Fig.4.4c**).

The details of this testing apparatus (e.g., TTSC frame, LVDTs) can be found in Minaeian 2014 and Sarmadivaleh 2012. In order to capture the aseismic strain energy dissipation with sufficient time resolution during the experiment, fracture propagation must be sufficiently slow (Bunger 2005a; Sun and Jin 2006). To achieve this, a Newtonian fluid with a relatively high viscosity (i.e., honey), and a low injection rate of 0.2 cc/min were used, while the borehole pressure evolution with time is monitored (Feng et al. 2020). Moreover, a micro-metric control needle valve V_i (see **Fig.4.4**) is used at the injection inlet to slow down the injected fluid, minimise turbulent flow into the wellbore/sample, and better mimic in the laboratory field injection conditions. (Bunger 2005a; Sarmadivaleh and Rasouli 2015) The initial stress conditions prior to injection are maintained (regulated) at low (σ_v = 6.5 MPa, σ_H = 3 MPa, σ_h = 1.5 MPa) and high (σ_v = 15 MPa, σ_H = 10MPa, σ_h = 5 MPa) for the hydraulic fracturing experiments reported here. The time-dependent deformation (creep) are also measured under the high stress condition (see Section 6.4 and **Appendix D**).

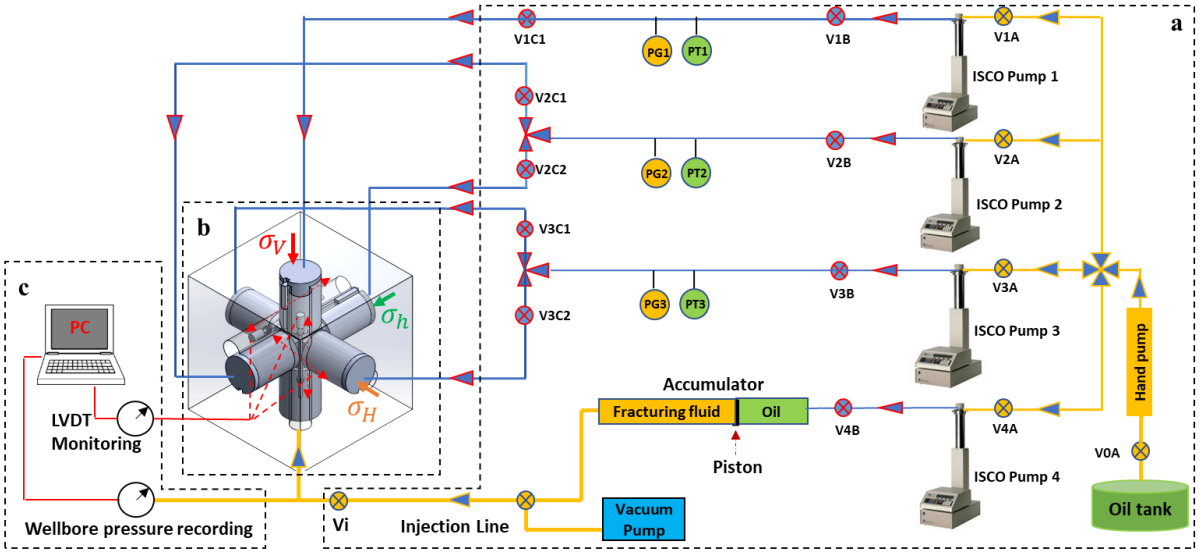

Fig.4.4 Schematic of hydraulic fracturing experimental setup: **a** Pumping system; **b** fracturing system; and **c** data acquisition system. PT pressure transducer, PG pressure gauge, V valve, Vi micro-meter valve, LVDT Linear Variable Differential Transformer, PC data acquisition.

4.3 Results and Discussion

4.3.1 Preliminary experimental results for BI_1 to BI_8

As abovementioned, four different type of samples were tested namely S_1 (quartz-rich sample), S_2 (clay-rich sample), S_3 (calcite-rich sample) and S_4 (mixed average). The failure patterns of samples after four mechanical tests (a-*UCS*, b-*TCS*, c-*BTT* and d-*SCB*) are presented in **Fig.4.5**. Shear failure is observed in all samples including an additional natural sample (*NS* used as a reference)(**Fig.4.5a**). The results of *BTT* and *SCB* are also shown in **Fig.4.5c and d** indicating developed cracks along the vertical line of the samples, caused by tension as expected. The stress-strain curve of S_1 from *UCS* test is additionally shown in **Fig.4.6** i.e. the elastic strain and polynomial function fitting the axial stress-strain curve are shown on the graph, where the length of DE and DF represent the elastic and total strain. The recoverable and total energy can be represented as the area under BCF and ACF respectively. The internal friction angle (Φ) and cohesion (*Co*) are also obtained based on TCS test (**Fig.4.5b)** and Mohr-Coulomb criterion (**Fig.4.7**). The obtained mechanical properties are additionally listed in **Table 4.3**, which are later used in *BI* calculation and scaling law.

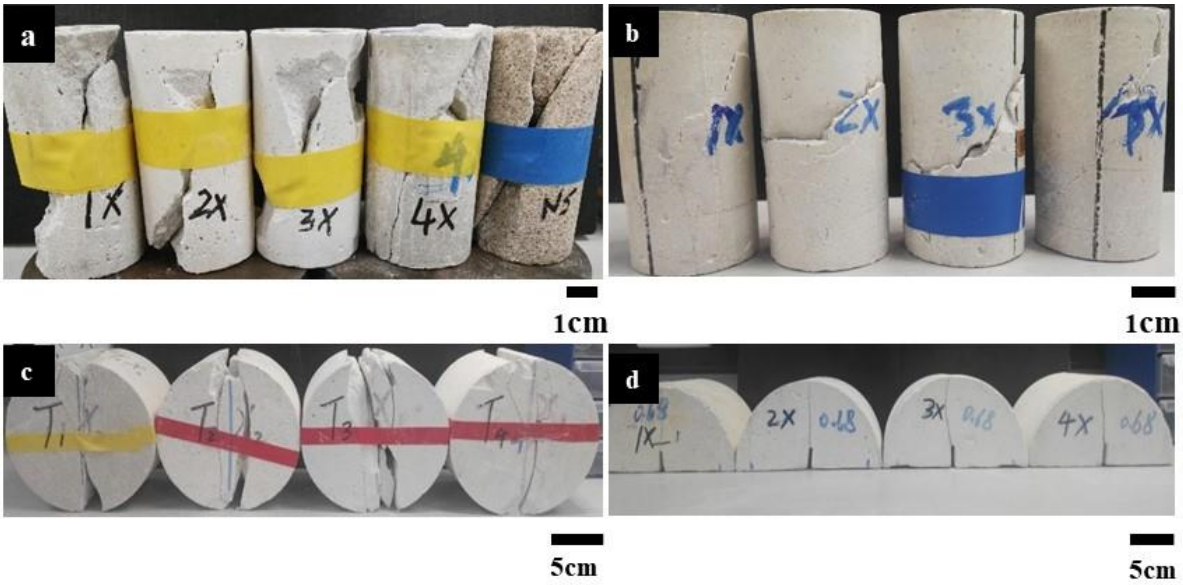

Fig.4.5 Failure patterns of the samples after (a) UCS; (b) TCS; (c) BTT and (d) SCB tests

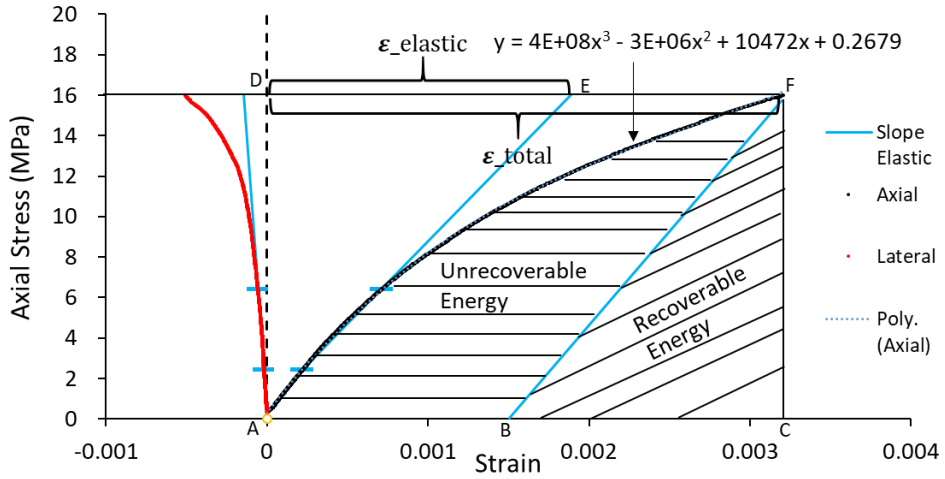

Fig.4.6 Stress vs strain curve obtained from UCS testing on sample (S_1)

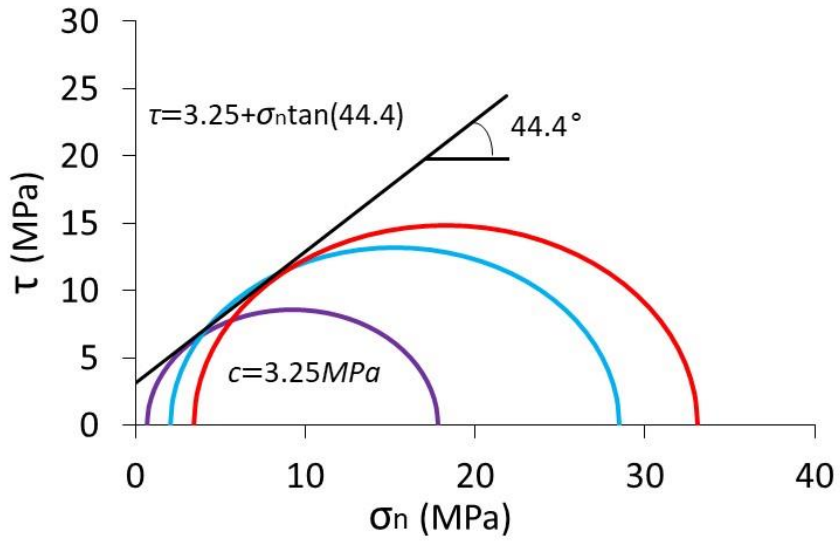

Fig.4.7 Fitted Mohr-Coulomb criterion to the TCS data of sample (S_1)

Table 4.3 Mechanical properties (averaged) of the preliminary series of mineral-cement mixtures and used in this study, and determined through unconfined (UCS) and triaxial (TCS) compression tests.

Mechanical properties	Quartz-rich (S_1)	Clay-rich (S_2)	Calcite-rich(S_3)	Mixed-average(S_4)
Young's modulus *E*, Gpa	11.5	6.7	8.5	10.4
Poisson's ratio ν	0.11	0.27	0.14	0.18
Cohesion *Co*, MPa	3.25	2.79	2.58	3.07
Internal friction angle $\Phi(^o)$	44.4	30.8	38.6	43.7
Tensile strength σ_T, MPa	1.11	0.66	1.1	1.38
Fracture toughness K_{IC}, Mpa√m	0.32	0.20	0.25	0.21
P-wave velocity V_p, m/s	2667	1826	2253	2035
S-wave velocity V_s, m/s	1740	1130	1283	1300
Porosity ∅	0.22	0.21	0.11	0.21

4.3.2 New mechanical and physical properties for BI_3 and BI_7

The physical photo of five new types of samples after Tri-axial compressive tests (TCS) are presented in **Fig.4.8**. The shear failure is observed in Quartz-rich S_1 **(Fig.4.8a)**, Average-mix S_4 **(Fig.4.8b)** and Calcite-rich S_3 **(Fig.4.8c)** samples, while for the two types of Clay-rich sample S_5 **(Fig.4.8d)** and S_2 **(Fig.4.8e)** there are no significant failure plane due to their high ductility under 3.4MPa of confinement. The representative stress-strain curve from TCS is shown in **Fig.4.9,** in which the higher portion of plastic axial/lateral strain are observed in both clay-rich samples **(**S_2 and S_5).

The mechanical properties of the new mineral-cement mixtures used for the model BI_3 and BI_7 (see **Table 2.1**) are shown in **Table 4.4**. Young's modulus *E* ranges between 1.5 and 6.9 GPa, where the quartz-rich mixture S_1 exhibits the highest value, followed by the PMMA S_6, the calcite-rich mixture S_3, the mixed-average mixture S_4, the clay-rich mixture S_2, and the lowest value was found for the clay-rich$_2$ mixture S_5. Poisson's ratio ranges from 0.39 for PMMA, down to 0.1 for the clay-rich mixture S_2; while mixtures S_1, S_5, S_4, and S_3 exhibit intermediate

values comprised between 0.17 and 0.21. The internal friction angle Φ ranges between 14.4° for PMMA and 42° for the quartz-rich mixture S_1; and the cohesion C_o is comprised between 0.6 MPa for the clay-rich mixture S_2 and 44.6MPa for PMMA. Ultrasonic compressional and shear wave velocities (V_P and V_S, respectively) at room conditions are higher in the stiffer mixtures S_1 and S_6 than in the clay-rich mixtures S_2 and S_5. To the first order, this is attributed to the attenuation of acoustic wave by clay minerals (Han et al. 1986; Li et al. 2021).

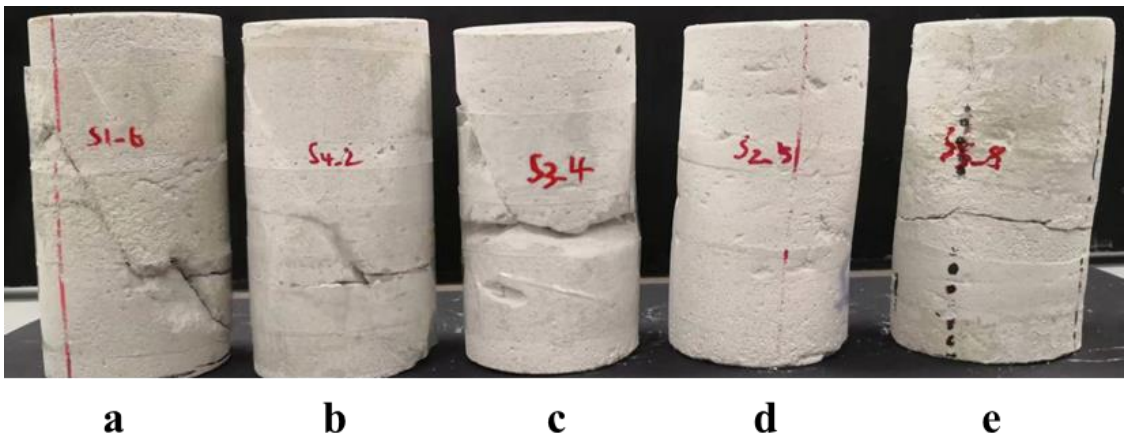

Fig.4.8 Failure patterns of the five new synthetic samples after TCS under confinement of 3.4MPa: a) Quartz-rich S_1 b) Average-mix S_4 c) Calcite-rich S_3 d) Clay-rich S_2 e) Clay-rich S_5

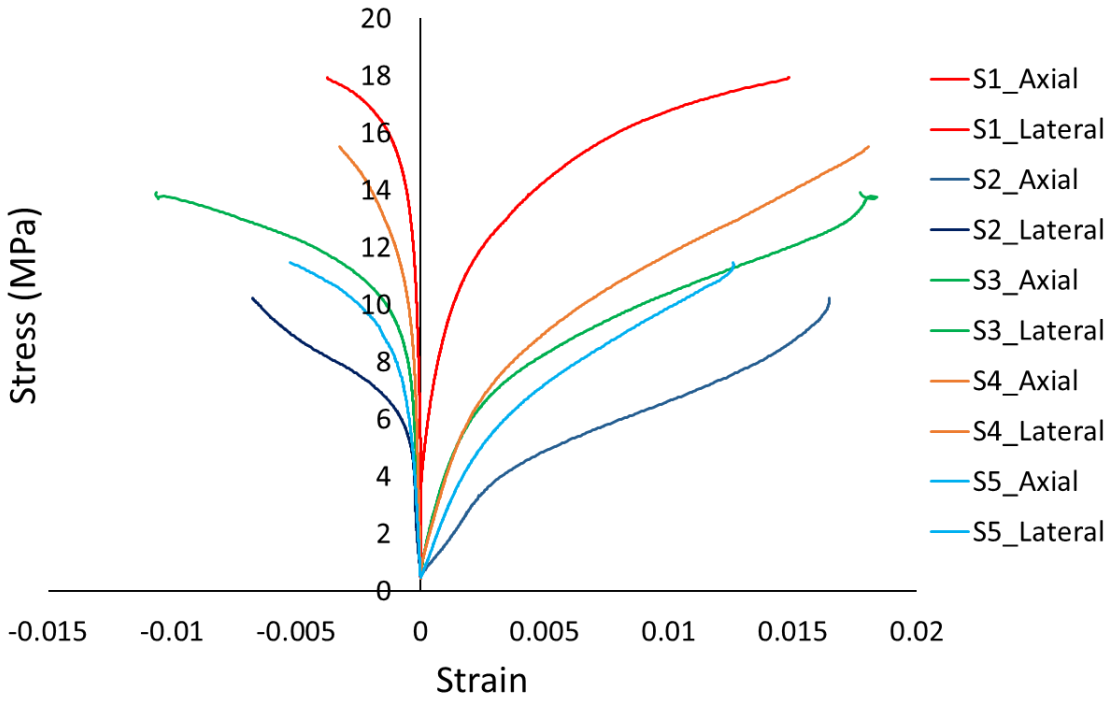

Fig.4.9 Stress vs strain curve obtained from TCS testing on samples (S_1 to S_5)

Table 4.4 Mechanical properties (averaged) of the new series of mineral-cement mixtures and PMMA used in this study, and determined through unconfined (UCS) and triaxial (TCS) compression tests.

Mineral-cement mixture	Young's modulus *E* (GPa)	Poisson's ratio*n* (-)	Friction angle Φ (°)	Cohesion *Co* (MPa)	P-wave velocity V_P (km/s)	S-wave velocity V_S (km/s)	Porosity ϕ (-)
Quartz-rich(S_1)	6.9*	0.17*	42*	1.76*	2.1	1.4	0.29
Clay-rich(S_2)	2.6*	0.1*	35.3*	0.6*	1.3	0.87	0.3
Calcite-rich(S_3)	3.2*	0.21*	40.9*	0.9*	1.69	1.07	0.2
Mixed average(S_4)	3.0*	0.18*	35.8*	1.5*	1.8	1.17	0.24
Clay-rich2(S_5)	1.6*	0.17*	37.3*	0.8*	1.47	0.97	0.3
PMMA(S_6)	6.2**	0.39**	14.4**	44.6**	2.75	1.4	0

** UCS tests are conducted on dry samples, and TCS tests are conducted in dry conditions at 0.6, 2.1, and 3.4 MPa confining pressure. ** Data reported in the literature.*

4.3.3 Integrated wellbore pressure and strain data for BI_9 and BI_{10}

The time of fracture initiation serves as a reference for the experimental evaluation of the energy partitioning during hydraulic fracturing. The borehole pressure BHP and the three mutually orthogonal strains derived from the measured displacements are normalized by their value at this specific time. The injection energy E_I and the aseismic deformation energy E_d (**Eq.2.18**) are calculated accordingly. The typical hydro-mechanical data set acquired during the hydraulic fracturing of a quartz-rich sample S_1 are shown in **Fig.4.10** (low confinement) and **Fig.4.11** (high confinement), where by convention a negative (positive) strain indicates extension (compression). Overall, the time evolution of the three mutually orthogonal strains recorded during the experiment are significantly nonlinear. The horizontal tensile strain is essentially induced by the opening and propagation of the fracture (negative ε_h in green), whereas the vertical shortening is induced by the imposed vertical compressive stress σ_v simulating the overburden (positive ε_v in blue).

The evolution of the three strains as a function of the borehole pressure BHP for the samples under low confinement (σ_V = 6.5 MPa, σ_H = 3 MPa, and σ_h = 1.5 MPa) are shown in **Fig.4.12**. The magnitude of the strain ε_H along the maximum horizontal stress σ_H (orange curve) remains relatively small compared to the other two strains (from sample S_1 to S_5); it also remains relatively constant throughout the experiment, although a small and temporary deflection can

be observed when the magnitude of ε_h (green curve) and ε_V (blue curve) exhibit the largest change with BHP during fracture propagation. While for PMMA S_6 (**Fig.4.12f**), the strain ε_H shows a significant deflection comparing to that of other samples.

Under the higher confinement (σ_V = 15 MPa, σ_H = 10 MPa, and σ_h = 5 MPa) shown in **Fig.4.13**.The magnitude of the strain ε_H along the maximum horizontal stress σ_H (orange curve) shows slightly negative deflection for quartz-rich S_1, mixed-average S_4, and PMMA S_6; while significant positive compression are observed in clay-rich S_2, the calcite-rich S_3, and the clay-rich$_2$ S_5. The representative full hydro-mechanical data set and more detailed discussion are presented in **Chapter 6**.

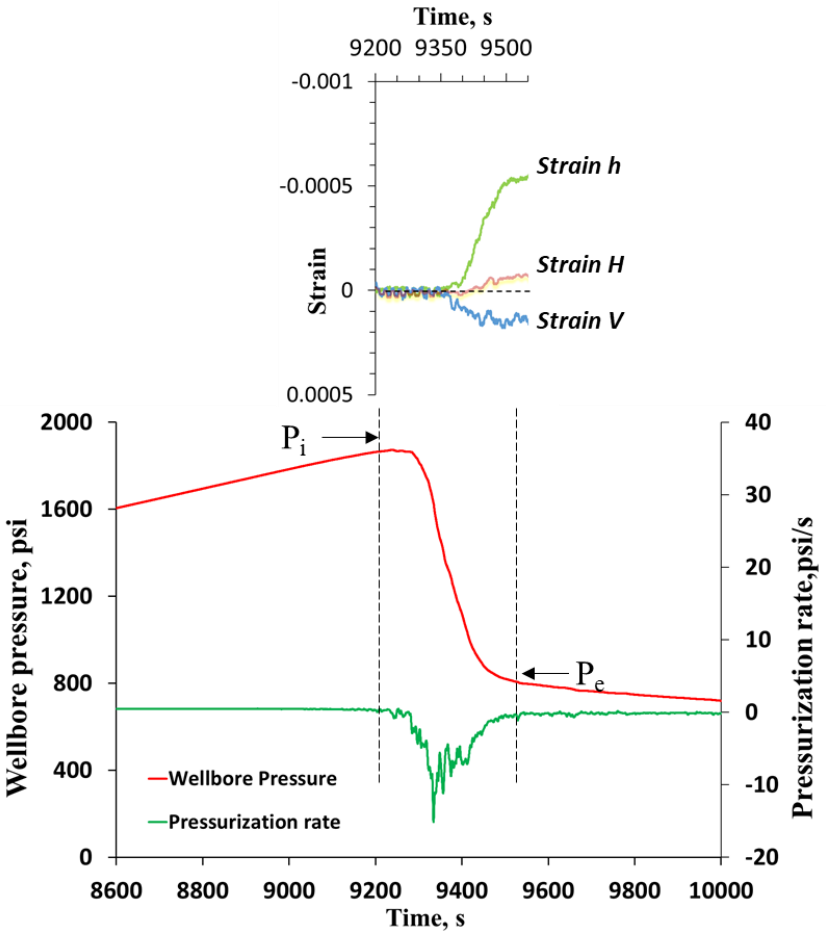

Fig.4.10 Synchronized wellbore pressure and strain data recorded during a representative hydraulic fracturing experiment (quartz-rich sample S_1) under σ_V = 6.5 MPa (940psi), σ_H = 3 MPa (440psi), and σ_h = 1.5 MPa (220psi). P_i and P_e denote the borehole pressure at the initiation and at the end of fracture propagation, respectively.

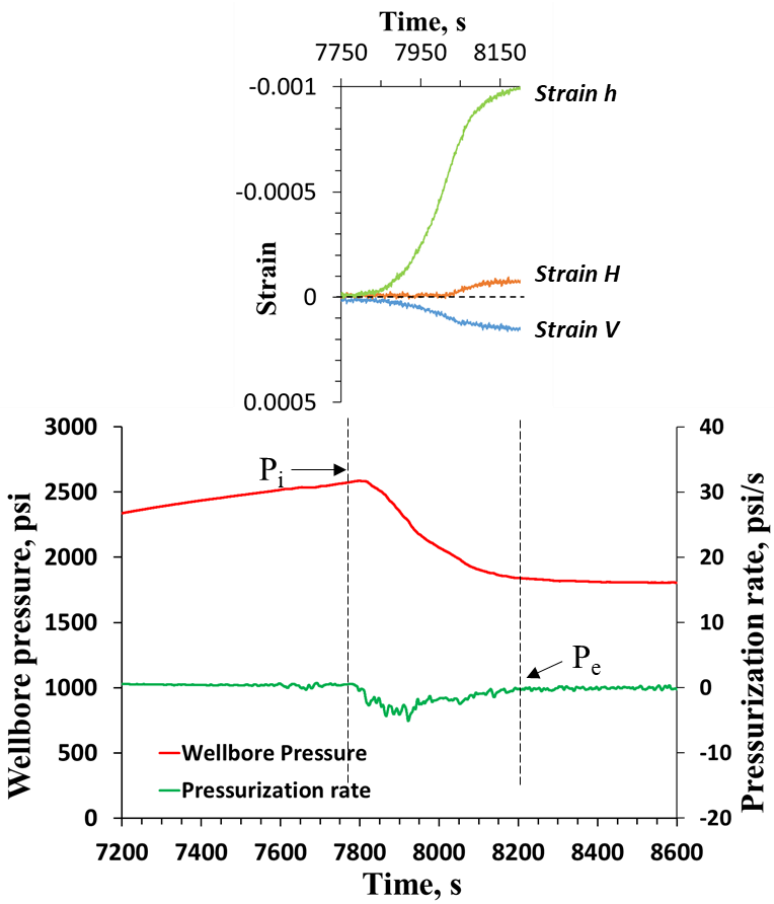

Fig.4.11 Synchronized wellbore pressure and strain data recorded during a representative hydraulic fracturing experiment (quartz-rich sample S_1) under σ_V = 15 MPa (2175psi), σ_H = 10 MPa (1450psi), and σ_h = 5 MPa (725psi). P_i and P_e denote the borehole pressure at the initiation and at the end of fracture propagation, respectively.

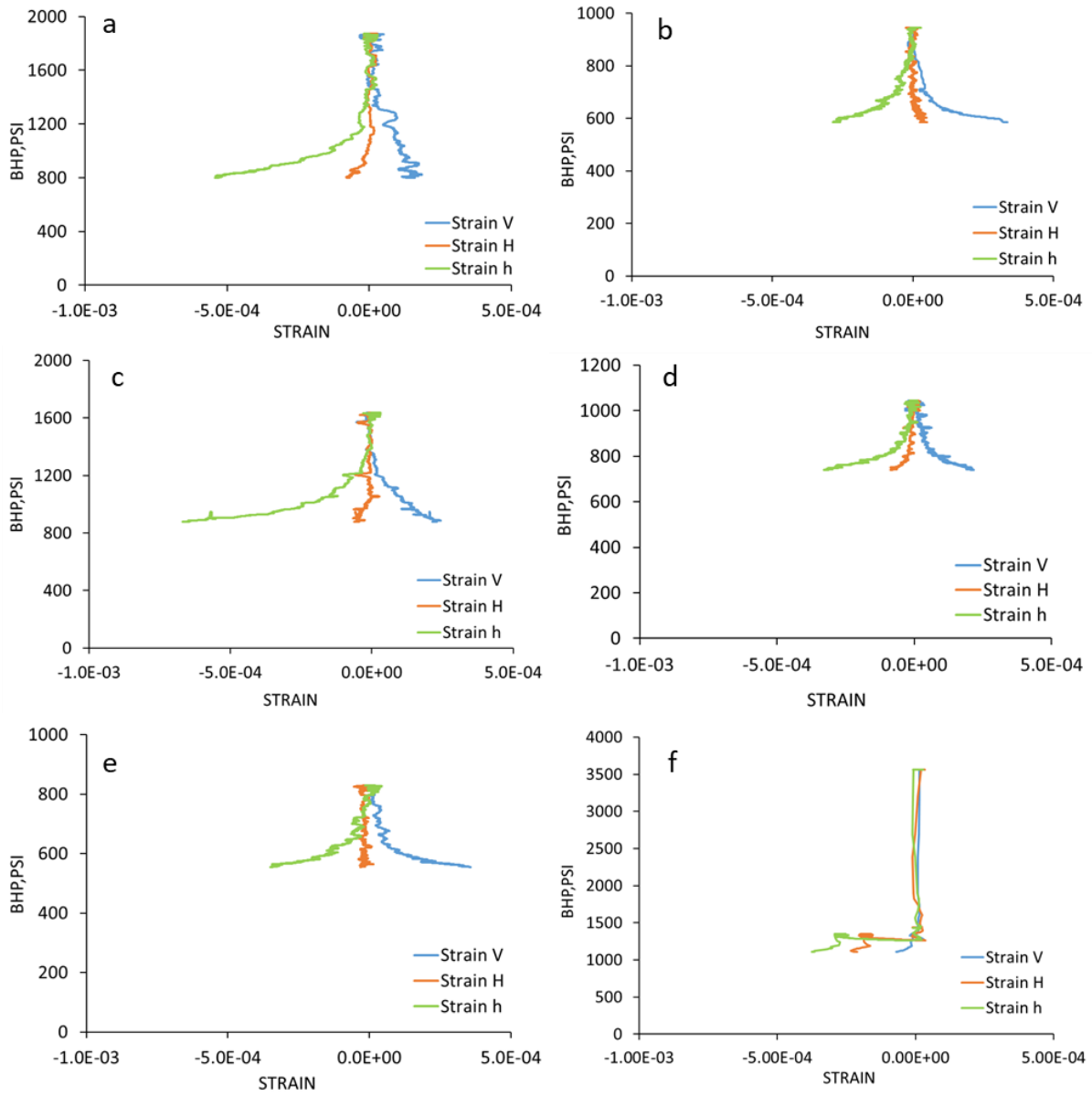

Fig.4.12 Wellbore pressure and strain data recorded during hydraulic fracturing between fracture initiation at BHP = P_i, and the end of propagation at BHP = P_e for: a) the quartz-rich sample S_1, b) the clay-rich S_2, c) the calcite-rich S_3, d) mixed-average S_4, e) the clay-rich$_2$ S_5, and f) the PMMA S_6. The stress conditions are σ_V = 6.5 MPa, σ_H = 3 MPa, and σ_h = 1.5 MPa.

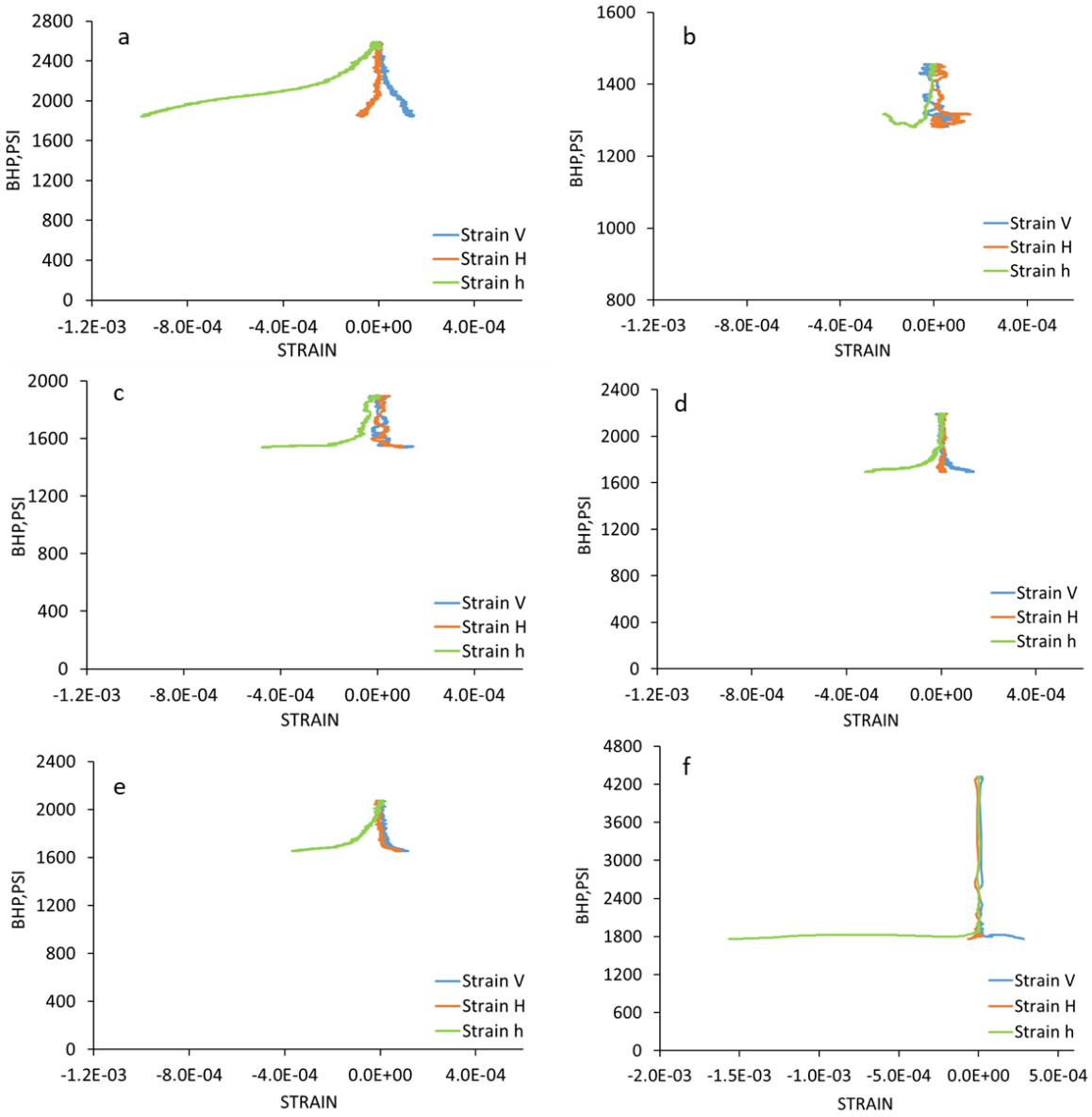

Fig.4.13 Wellbore pressure and strain data recorded during hydraulic fracturing between fracture initiation at BHP = P_i, and the end of propagation at BHP = P_e for: a) the quartz-rich sample S_1, b) the clay-rich S_2, c) the calcite-rich S_3, d) mixed-average S_4, e) the clay-rich$_2$ S_5, and f) the PMMA S_6. The stress conditions are σ_V = 15 MPa, σ_H = 10 MPa, and σ_h = 5 MPa.

4.3.4 Visualization of hydraulic fracture geometry

The representative photographs of the samples after hydraulic fracturing are shown in **Fig.4.14** (low confinement) and **Fig.4.15** (high confinement). It turns out that for clay-rich S_2, the calcite-rich S_3, and the clay-rich$_2$ S_5 the fracture is overall orthogonal to σ_h, as expected. However, for the quartz-rich S_1 (**Fig.4.14a** and **Fig.4.15a**), and the mixed-average S_4 (**Fig.4.14d** and **Fig.4.15d**) samples, the fracture is tilted with respect to both σ_H and σ_h. The most striking result is the vertically shear-opening fracture geometry within PMMA S_6 under

the high confinement (**Fig.4.15f**), comparing to the conventional horizontal opening for that of lower confinement (**Fig.4.14f**). More discussion regarding to the fracture geometry verse brittleness index (BI) will be presented in **Chapter 6**.

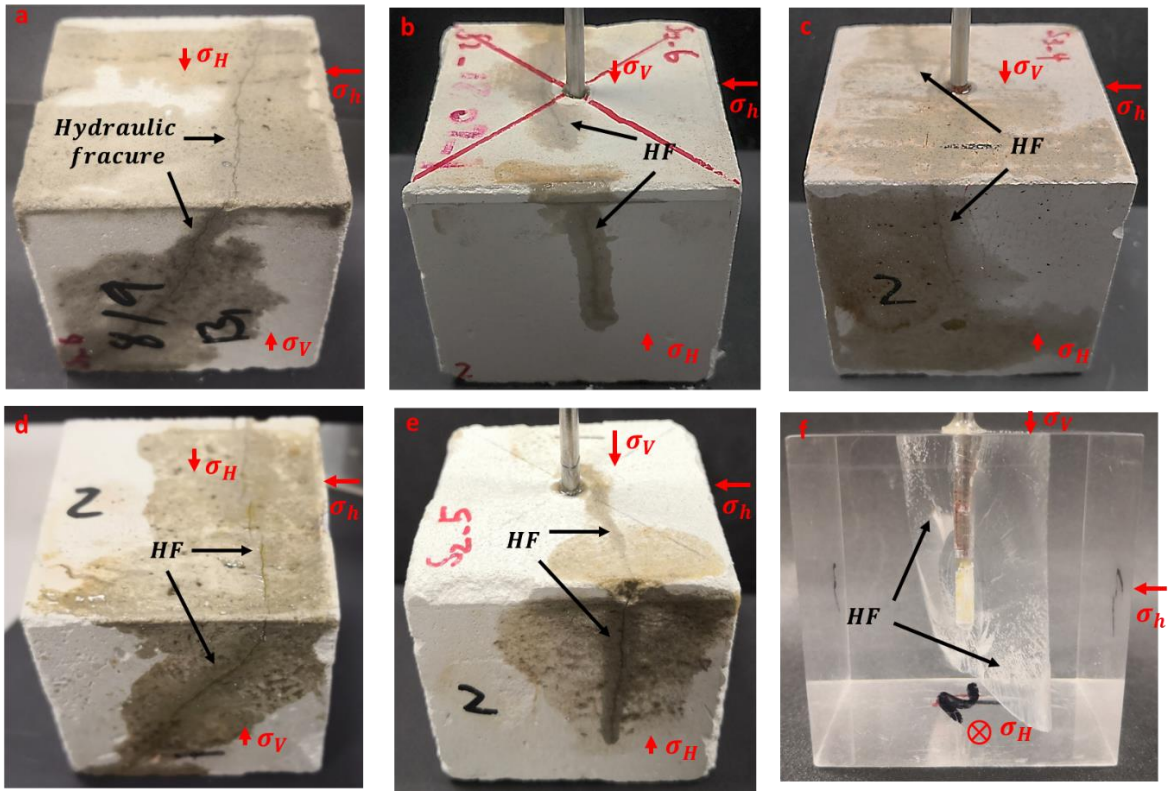

Fig.4.14 Hydraulic fracture propagation scenario, where either the strain along the maximum principal horizontal stress e_H is negligible, or the fracture is orthogonal to s_H. Fractured samples from: a) the quartz-rich rock type S_1, b) the clay-rich S_2, c) the calcite-rich S_3, d) the mixed-average S_4, e) the clay-rich$_2$ S_5, and f) the PMMA sample. The stress conditions are σ_V = 6.5 MPa, σ_H = 3 MPa, and σ_h = 1.5 MPa.

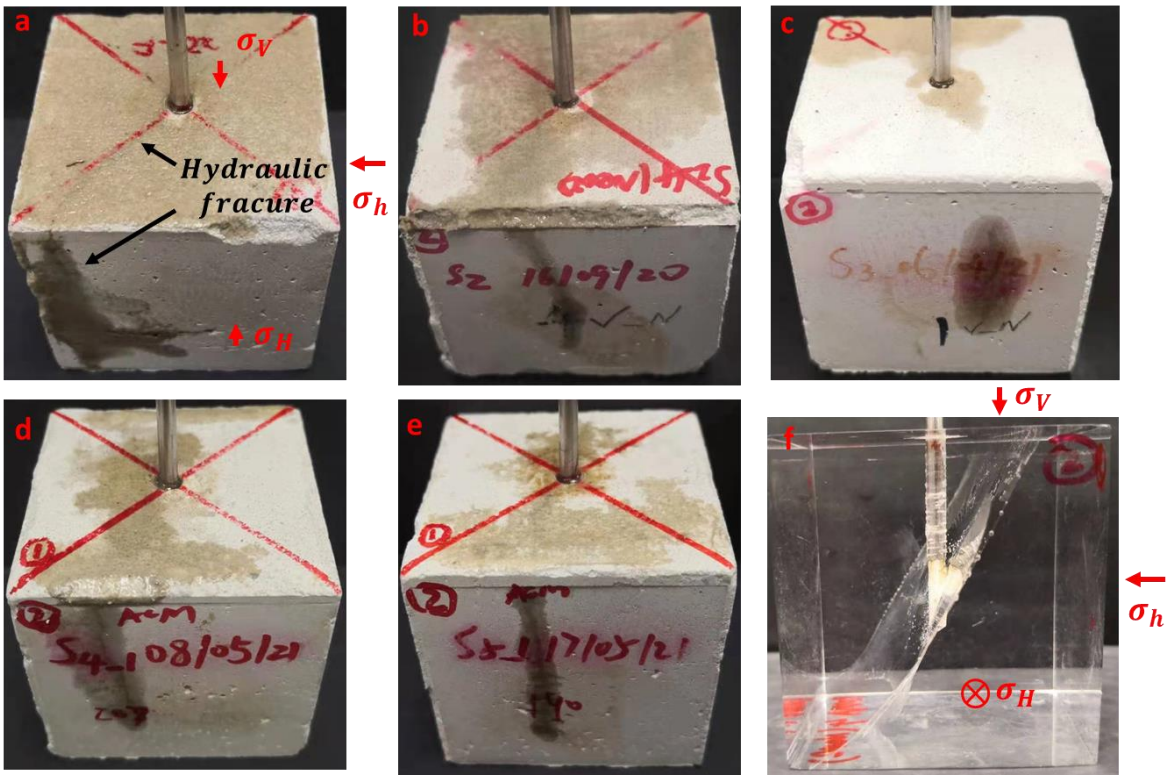

Fig.4.15 Hydraulic fracture propagation scenario, where either the strain along the maximum principal horizontal stress e_H is negligible, or the fracture is orthogonal to s_H. Fractured samples from: a) the quartz-rich rock type S_1, b) the clay-rich S_2, c) the calcite-rich S_3, d) the mixed-average S_4, e) the clay-rich$_2$ S_5, and f) the PMMA sample. The stress conditions are σ_V = 15 MPa, σ_H = 10 MPa, and σ_h = 5 MPa.

Chapter 5
Brittleness index (BI) quantification based on investigated models and experimental results

5 Brittleness index (BI) quantification based on investigated models and experimental results

This chapter mainly discusses the results of brittleness index (BI) based on the investigated models (i.e., BI_1 to BI_{10} listed in **Table 2.1**): (i) Initially we present the BI quantification based on the preliminary study (i.e., BI_1 to BI_8), and exam the consistence among these eight *BI* models. (ii) Then we show the BI results based on cohesive energy model BI_9, and the two conventional models BI_3 and BI_7. (iii) Finally, we present the BI results based on the quantified aseismic deformation energy and injection energy (BI_{10}); and compare it with the BI_7 and BI_9. The discussion and conclusion are finally given.

This chapter includes a modified content from the following scientific articles:

Feng R., Sarout J., Dautriat J., Ghuwainim Y., Rezaee R., Sarmadivaleh M (2022b). Laboratory validation of a new hydro-mechanical energy-based brittleness index model for hydraulic fracturing. Preprint DOI: doi.org/10.31223/X55M1J

Feng R., Zhang Y., Rezagholilou A., Roshan H., Sarmadivaleh M (2020). Brittleness Index: From Conventional to Hydraulic Fracturing Energy Model. *Rock Mechanics and Rock Engineering* 53: 739-753.

5.1 Results of BI quantification

5.1.1 BI based on preliminary experimental results (BI_1 to BI_8)

The results of brittleness index models ($BI_{1\text{-}8}$ in **Table 2.*1***) are listed in **Table 5.*1***. It is seen from this table that the magnitude of all *BI* models vary from 0 to 1 except the values of BI_5 which are significantly higher than 1. The BI_5 model therefore requires substantial modification to give within range results. Furthermore, it is noteworthy that the magnitude of BI_1 and BI_2 are highly dependent on the selected inflection point for elastic to plastic transition based on the stress-strain data thus inducing a subjective estimation (**Fig.4.*6***). Moreover, the values of *UCS* of rocks are usually one order of magnitude greater than their tensile strength (σ_T). Considering the BI_4 model, the values of four type of samples ($S_{1\text{-}4}$) are very close to each other but deviates from other *BI* models (**Table 5.*1***). Based on the first-order assessment with above discussion, the models of BI_1, BI_2, and BI_4 are not recommended for brittleness evaluation for practical applications at this stage.

From models of BI_3 and BI_6, quartz-rich sample (S_1) exhibited the highest brittleness, followed by mixed average (S_4), calcite-rich (S_3), and the lowest brittleness for clay-rich (S_2). However, the brittleness of S_4 is larger than that of S_1 based on BI_5 model. The contradiction can be

explained by the parameters representing the failure mechanism in different *BI* models. BI_3 was derived based on dynamic Young's Modulus (E) and Poisson's ratio (ν) to have direct field applications (Rickman et al. 2008). However, it is evident that distinct shale interval may exhibit analog E or ν due to the variety of mineral composition, but significantly different failure mechanisms. In addition, BI_5 was defined based on uniaxial compressive strength (*UCS*) and tensile strength (σ_T) and BI_6 was developed based on the internal friction angle obtained from triaxial loading. These tests induce different failure modes and damage mechanisms can be different.

Holt et al. (2015) demonstrated that the fracturing process can be dominated by either tensile or shear failure due to the complexity of geological conditions. The magnitude of BI_7 is quite low (0.1-0.22) compare with that of other models. This significant difference can be explained by the formulation of BI_7. This model is sensitive to high level of stresses or in the other word the high level of ductility in relatively weak rocks (refer to *UCS* and σ_T in **Table 4.*3***) which should lead to superficially lower *BI* prediction. This is also consistent with the simulation work accomplished by Papanastasiou (1999) and Papanastasiou et al. (2016). The applicability of BI_7 however needs further investigation for hard formations.

The results obtained from BI_8 indicate that quartz-rich sample (S_1) exhibited the highest brittleness, followed by mixed average (S_4), clay-rich (S_2), and finally the lowest brittleness for calcite-rich (S_3). This in turn indicates the discrepancies between the results of BI_8 with *BI*s in cases of S_2 and S_3. The presence of calcite mineral in the rock is often assumed to increase the brittle behavior of the rock and therefore assists increasing the stimulated reservoir volume (SRV) during hydraulic fracturing treatment (Jin et al. 2014; Wang and Gale 2009). However, the triaxial testing results showed that the ductile deformation of calcite crystals can be considerable at evaluated pressure (even at room temperature) (Evans et al. 1990; Wong and Baud 2012). Our results from BI_8 model also show a consistent trend to later where calcite-rich shale (S_3) exhibits high level of ductility which should potentially hinder the hydraulic fracture propagation. This is also in a good agreement with predictions of BI_3 and BI_7 models. It is also noted that the BI_3 and BI_7 have consistent trends (**Fig.5.1**). Quantitatively the *BI* is overestimated by BI_3 model but underestimated by BI_7 model when compare with proposed model (BI_8) (**Fig.5.1**).

Table 5.1 Brittleness index (BI) results based on models BI_{1-8}

BI model	Quartz-rich (S_1)	Clay-rich (S_2)	Calcite-rich (S_3)	Mixed Average (S_4)	Sparklines
BI_1	0.59	0.55	0.56	0.61	
BI_2	0.5	0.41	0.45	0.54	
BI_3	0.96	0.53	0.54	0.69	
BI_4	0.86	0.87	0.83	0.82	
BI_5	2.93	1.78	2.57	3.16	
BI_6	0.7	0.51	0.61	0.69	
BI_7	0.22	0.1	0.11	0.2	
BI_8	0.73	0.4	0.36	0.54	

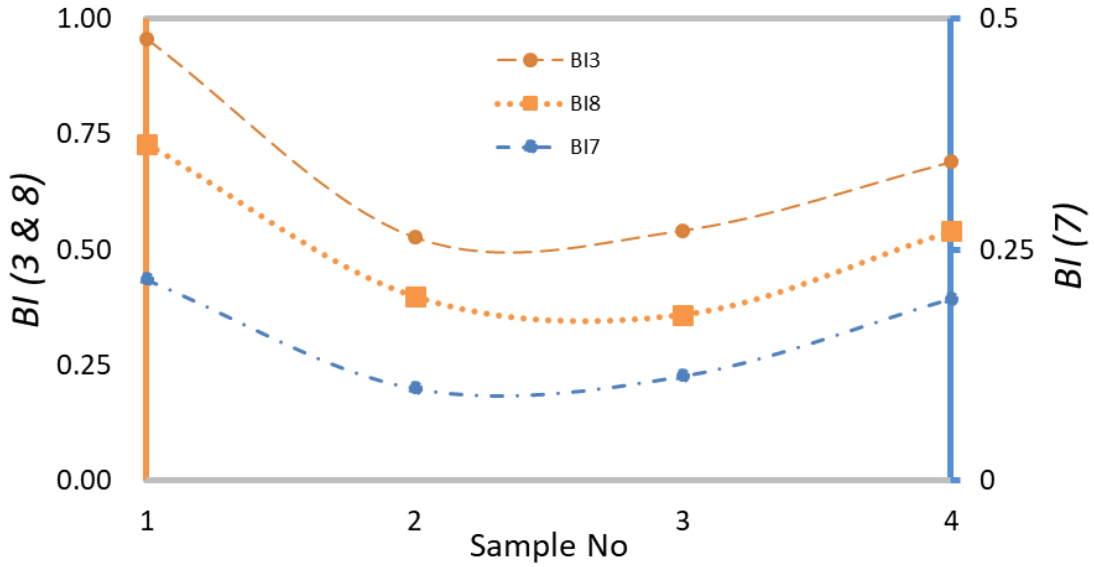

Fig.5.1 Brittleness index (BI_3, BI_7 and BI_8) versus investigated samples

5.1.2 BI based on Cohesive energy concept (BI_9)

The BI results of all six types of tested samples based on BI_3 (Rickman et al.'s model) , BI_7 (Papanastasiou et al.'s), and our cohesive energy concept- BI_9 are shown in **Table 5.2**. The results of BI_7 and BI_9 are evaluated under low (6.5, 3, 1.5MPa) and high confinement (15, 10, 5MPa). Under the lower confine, the BI_9 shows a good qualitative agreement with BI_7 in terms of the overall trend, in which the benchmark sample- PMMA (S_6) exhibited the highest brittleness, followed by quartz-rich sample (S_1), mixed average (S_4), calcite-rich (S_3), clay-

rich$_2$ (S_5), and finally the lowest brittleness for clay-rich (S_2). However, for BI_3 a distinct trend is observed, especially for the striking lower BI value of the PMMA S_6 and Calcite-rich S_3.

Under the higher confinement (15, 10 , 5MPa), the overall value of BI_9 is decreased; and the BI value of S_3, S_4, and S_5 are not as distinctive as the one under lower case. Interestingly, it is found that the BI value based on BI_7 and BI_9 are both quantitatively and qualitatively consistent (very limited error exists). However, as the confinement is increased, the BI_7 shows an anomalously increasing trend among samples of clay-rich (S_2), calcite-rich (S_3), and clay-rich$_2$ (S_5); an unexcepted constant BI value for quartz-rich (S_1) and mixed-average (S_4).

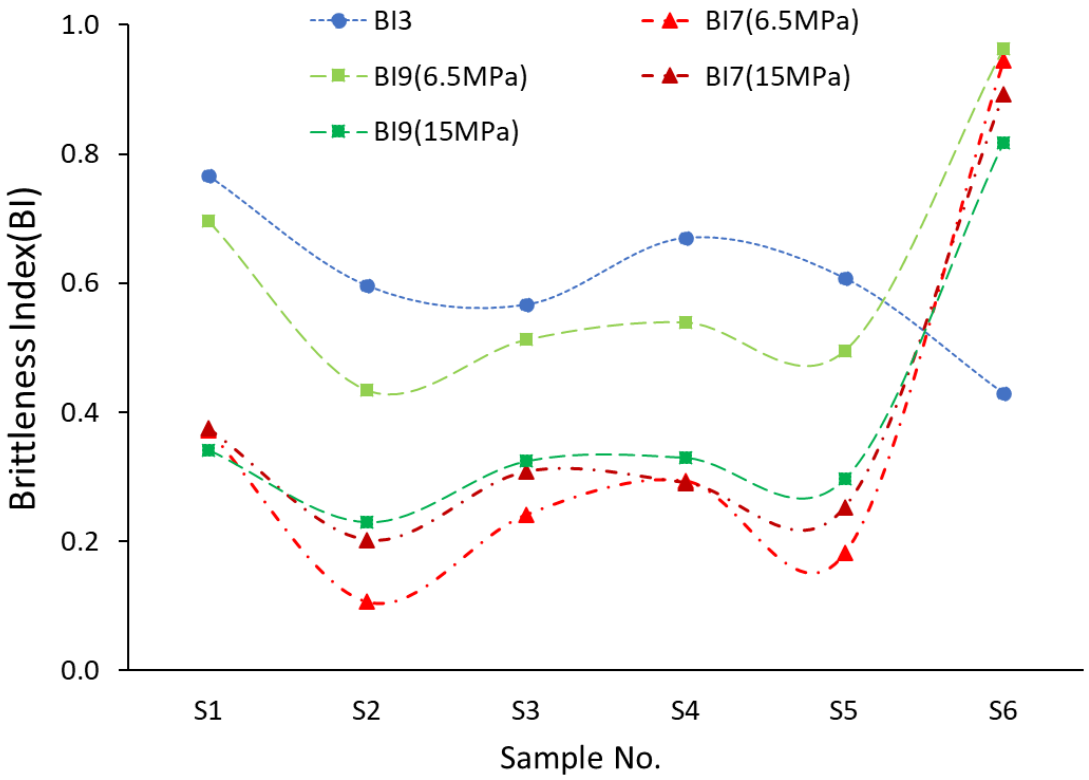

Fig.5.2 Brittleness index BI_3, BI_7 and BI_9 versus investigated samples under the confinement of low (σ_V = 6.5 MPa, σ_H = 3 MPa, and σ_h = 1.5 MPa) and higher (σ_V = 15 MPa, σ_H = 10 MPa, and σ_h = 5 MPa) .

5.1.3 BI based on calculated aseismic deformation energy (BI_{10})

The injection energy E_I, aseismic deformation energy E_d, and the energy partitioning ratio E_d/E_I are computed for the hydraulic fracturing experiments conducted on all mineral-cement mixtures and PMMA. The representative values for each material studied here are reported in **Table 5.2.** These results show that the clay-rich rock type S_2 exhibits the highest partitioning ratio for both high (E_d/E_I = 90.6%) and low confinement (E_d/E_I = 64.7%), respectively,

followed by the clay-rich$_2$ S_5 (86% and 61.8%), the calcite-rich S_3 (76.3% and 55.8%), the mixed-average S_4 (74% and 43.4%), the quartz-rich S_1 (65.2% and 32.4%); and the lowest value was recorded for the PMMA S_6 (6.1% and 2.7%).

These BI values based on models-BI_7 , BI_9, and BI_{10} are shown in **Table 5.*3*** and compared in **Fig.5.*3***. The overall value of BI_{10} decreases as the increase of confinement; and yield analogous trend across the tested materials studied (except for S_4). Under the high confining case, BI_7 and BI_{10} exhibited qualitative consistency of the trend among samples $S_{1\text{-}6}$. Their quantities are relatively consistent among S_1, S_4, and S_6; but a notable discrepancy exists among S_3, especially for the S_2 and S_5.Interestingly, the BI based on BI_7 (under the low confinement) and BI_{10} (under the high confinement) are shown to be quantitatively consistent, which is an unexpected result.

For the BI_9 and BI_{10} under the lower confinement, they quantitatively yield good consistency among quartz-rich S_1 and mixed-average S_4, and PMMA S_6; but a notably lower value of BI_{10} among the samples of clay-rich S_2, calcite-rich S_3, and clay-rich$_2$ S_5. While for the high confinement, the only consistency between BI_9 and BI_{10} is observed in S_1; the exceptional lower BI predictions based on BI_{10} are observed among $S_{2\text{-}5}$, especially for S_2 and S_5; but a higher BI_{10} for S_6.

Table 5.2 The Injection energy E_I, aseismic deformation energy E_d corresponding to hydraulic fracture propagation, and energy partitioning ratio E_d/ E_I calculated for the six materials under low and higher confinement studied here (Representative case). Values outlined in bold represent the minimum and maximum for each reported parameter.

Energy (J)	Quartz-rich (S_1)	Clay-rich (S_2)	Calcite-rich (S_3)	Mixed Average (S_4)	Clay-rich$_2$ (S_5)	PMMA (S_6)
E_I (Low Conf)	123	51.3	101	58	42	279
E_d (Low)	40	33.2	56.4	25.2	25.8	7.4
E_d / E_I (Low)	32.4%	64.7%	55.8%	43.4%	61.8%	2.7%
E_I (High Conf)	182.5	80	104.6	130	117	413
E_d (High)	119	72.5	80	96	100.8	25.2
E_d / E_I (High)	65.2%	90.6%	76.3%	74%	86%	6.1%

Table 5.3 Brittleness index results for the six materials studied here (Five types of mineral-cement mixtures and one PMMA). Values outlined in bold represent the minimum and maximum for each reported parameter.

BI model	Quartz-rich (S_1)	Clay-rich (S_2)	Calcite-rich (S_3)	Mixed Average (S_4)	Clay-rich$_2$ (S_5)	PMMA (S_6)
BI_7 (Low Conf)	0.373	**0.107**	0.242	0.294	0.182	**0.945**
BI_9 (Low)	0.696	**0.434**	0.512	0.539	0.495	**0.963**
BI_{10} (Low)	0.68	**0.35**	0.44	0.57	0.38	**0.974**
BI_7 (High Conf)	0.375	**0.2**	0.308	0.29	0.253	**0.893**
BI_9 (High)	0.342	**0.23**	0.324	0.33	0.3	**0.82**
BI_{10} (High)	0.35	**0.094**	0.24	0.26	0.14	**0.94**

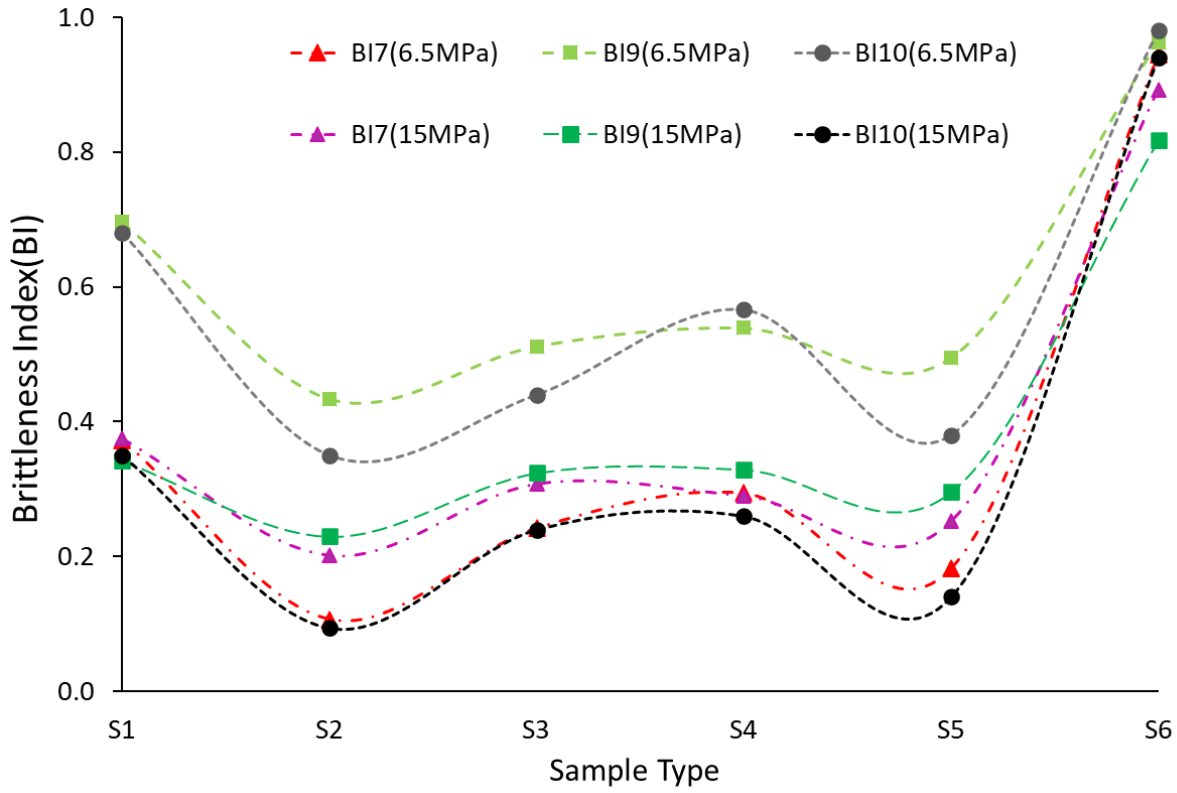

Fig.5.3 Brittleness index BI_7, BI_9 and BI_{10} versus investigated samples under the confinement of low (σ_V = 6.5 MPa, σ_H = 3 MPa, and σ_h = 1.5 MPa) and higher (σ_V = 15 MPa, σ_H = 10 MPa, and σ_h = 5 MPa).

5.2 Discussion and Conclusion

The preliminary results (**Section 5.1.1**) indicates that the BI value based on BI_3 and BI_7 are qualitatively consistent with the preliminary hydraulic fracturing energy-based model BI_9 (**Fig.5.1**). Therefore, BI_3 and BI_7 are incorporated with BI_9 and BI_{10} for this study (**Fig.5.3)**. It is found that BI_3 fails in predicting the BI value for a wide range of geomaterials, i.e., the extreme-brittle PMMA S_6. For preliminary and current study, the overall BI value are both overestimated by BI_3, which could be attributed to the lack of P-wave and S-wave measurement (**Table 2.1**) subjected to the confinement.

Both BI_9 and BI_{10} yield a reasonable decremental trend as the increase of confinement (**Fig.5.3**), revealing that both models are stress-dependent. However, it is observed that the BI value based on BI_9 are relatively indistinguishable among clay-rich S_2 , calcite-rich S_3, and clay-rich$_2$ S_5, which may attribute to the limitation of theoretical concept (cohesive energy) used in this model definition. On the other hand, the anomalous value of BI_7 observed from the low-to-high confinement indicate that the applicability of this model is challenged for variable confining stresses, especially when the range of rock types/rheology arise. Interestingly, the anomalously low value of BI_7 under the low confinement is shown to be coincidently consistent with the BI_{10} which is under high confinement; this phenomenon requires further investigation on the sensitivity.

Under the higher confinement (15, 10 and 5MPa) (**Fig.5.3**), the quantitative agreement of the BI value of quartz-rich S_1 and mixed-average S_4 based on BI_7 , BI_9 , and BI_{10} reveals that these three models could be applied for the assessment of analogous quasi-brittle rocks. In contrast, the BI_7 and BI_9 are indistinguishable for relatively ductile samples e.g., clay-rich S_2, calcite-rich S_3, and clay-rich$_2$ S_5, which increase the uncertainties for field assessment. These observations in turns indicate that the BI_{10} is stress-dependent and capable of capturing the brittle-to-ductile behaviour within a wide range of rheological samples subjected to hydraulic fracturing.

Chapter 6

Role of Brittleness index (BI) in hydraulic fracture initiation and propagation

6 Role of Brittleness index (BI) in hydraulic fracture initiation and propagation

In this chapter we integrate the quantified BI based on the newly developed model BI_{10} and the characterized hydraulic fracture (HF) attributes, e.g., HF geometry, 3D strain from hydraulic fracturing experiments. The X-ray Computed Tomography (CT) imaging is used to document the HF geometry. Finally, a correlation between the normalized fracture area (A_{FN}) and the brittleness index (BI) of tested samples is introduced. The results demonstrate the role of BI in orientation angle of HFs, state of stress/strain, fracturing area, and roughness of the fracture surface.

This chapter includes a modified content from the following scientific articles:

Feng R., Liu S., Sarout J., Dautriat J., Zhong Z., Rezaee R., Sarmadivaleh M (2022a). Hydraulic fracturing: Laboratory evidence of the brittle-to-ductile transition with depth. Preprint DOI: doi.org/10.31223/X5PH0S

Feng R., Sarout J., Dautriat J., Ghuwainim Y., Rezaee R., Sarmadivaleh M (2022). Laboratory validation of a new hydro-mechanical energy-based brittleness index model for hydraulic fracturing. Preprint DOI: doi.org/10.31223/X55M1J

6.1 Introduction

The deformation of geo-materials incorporate the process as shear stress is increased toward failure: I- initial elastic deformation; II – non-recoverable deformation, i.e., brittle micro-cracking, or ductile/plastic flow; III – micro-cracks nucleation and macroscopic fracture propagation. The three stages are highly influenced by the confinement of stress, a brittle-to-ductile transitional failure is thus expected and observed as the increase of confinement (Aharonov and Scholz 2019; Evans et al. 1990; Minaeian 2014; Nygård et al. 2006; Vachaparampil and Ghassemi 2017; Wong and Baud 2012; Zhang et al. 1993). However, much fewer investigations focus on the transitional deformation induced by hydraulic fracturing emerging in a wide range of underground engineering applications. Hydro-mechanical force is the main driven mechanism for the propagation of hydraulic fracture and with the same analogy, such transitional failure should be a measurable function of stress. Deeply understanding this transitional deformation can facilitate not only theoretical/numerical modelling but also provide critical insights for field applications associated with hydraulic fracturing.

When hydraulic fracture initiates and propagates within geo-materials under *in-situ* stresses, three types of failure modes are often observed: mode-I (tensile), mode-II (shear), and mixed-

mode-I and II (Economides and Nolte 1989; Gischig and Preisig 2015; Wu 2006). The stress anisotropy, fluid mechanics, natural fractures, and rock mechanical properties are recognized as the most influential factors in the failure mode (Gischig and Preisig 2015; Li et al. 2020a; Liu et al. 2020b; Papanastasiou 1997; Sarmadivaleh 2012; Wang 2019; Wang et al. 2013; Yang et al. 2021; Zeng et al. 2020; Zhang et al. 2009; Zhou et al. 2008). Incorporating all these parameters in fracturing analysis is complicated to be achieved. Since the hydraulic fracture growth is a dynamic process where the damage is mainly accumulated adjacent to the tip within the process zone (Desroches et al. 1994; Elices et al. 2002; Garagash 2019; Ju et al. 2021; Liu and Lecampion 2021; Papanastasiou 1997), which allows an alternative way studying the fracturing process. Several studies demonstrated that the plastic yielding/stress softening at the tip will absorb the effective injection energy, which significantly hinders the fracture propagation and results in a uniformed fracture geometry in ductile rocks (Feng et al. 2020; Ju et al. 2021; Papanastasiou 1997; Parisio et al. 2021). Recently, Ju et al. (2021) performed a 3D finite element-discrete element (FE-DE) numerical model for hydraulic fracture propagation in tightly brittle and ductile reservoirs. This work also used the entropy weight method (EMW) for brittleness definition/evaluation, in which the six influencing factors (Young's modulus, Poission's ration, cohesion, internal friction angle, tensile strength, and fracture toughness) are incorprated. They confirmed that the stress concentration near the fracture tip is highly diffused in the ductile reservoir. Parisio et al. (2021) carried out an experimental study of the brittle-to-ductile transition of hydraulic fracture within Polymethyl Methacrylate (PMMA). They observed complex fracture patterns under non-uniform stress distribution in the sample under the brittle regime. The complexity of fracture is significantly reduced as the ductility is increased. These studies revealed that a brittle-to-ductile transition is anticipated for the hydraulic fracture in a wide range of rock types in elevated confinements. However, such experimental study on a wide range of geo-materials is still lacking, which is essential to provide enough data set required for the calibration of the modelling suitable for field applications.

In this chapter, we present hydro-mechanical data based on hydraulic fracturing tests on variable types of geomaterials subjected to two sets of true triaxial stress conditions (TTSC), i.e., low confining (σ_1= 6.5MPa, σ_2= 3MPa, and σ_3=1.5MPa), and higher confining stresses (σ_1= 15MPa, σ_2=10MPa, and σ_2=5MPa); the evolution of wellbore pressure and the three mutually orthogonal strains induced by hydraulic fracture propagation are interpreted. We also interpreted the geometry and surface area (A_F) of hydraulic fracture based on the visualization

of the X-ray Computational Tomography (CT) images of tested samples. These quantifications allow us to correlate the A_F and the brittleness index (BI) of the samples subjected to hydraulic fracturing; this correlation is compared against the previous numerical study.

6.2 Representative hydro-mechanical data

Fig.6.1 and **Fig.6.2** show the representative hydro-mechanical data (i.e., the wellbore pressure and 3D strain (volumetric) induced by hydraulic fracturing) subjected to low (**Fig.6.1**) and high (**Fig.6.2**) confinement for the different samples: brittle PMMA (**Fig.6.1a and Fig.6.2a**), semi-brittle S_1 (**Fig.6.1b and Fig.6.2b**), semi-brittle S_4 (**Fig.6.1c and Fig.6.2c**), semi-ductile S_3 (**Fig.6.1d and Fig.6.2d**), ductile S_5 (**Fig.6.1e and Fig.6.2e**), and S_2 (**Fig.6.1f and Fig.6.2f**). The variation of 3D strain prior to the breakdown (maximum) pressure remains constant comparing to the strain after the breakdown pressure. The minimum horizontal strain ε_h is mainly produced by the propagation of fracture (negative ε_h in green curve), whereas the positive vertical strain ε_V (blue) indicates the vertical compression induced by the vertical stress. For brittle PMMA, and semi-brittle rock S_1, the strain ε_h abruptly increases after the (breakdown pressure) (**Fig.6.1 and Fig.6.2a and b**); in contrast, for the ductile rock (S_5 and S_2), the ε_h are gradually increased to the peak value (**Fig.6.1 and Fig.6.2e and f**).

Interestingly, the magnitude of strain ε_H along the intermediate horizontal stress σ_H (orange curve) shows a slightly negative deflection (tension) for semi-brittle sample S_1 under both low (**Fig.6.1b**) and high confinement (**Fig.6.2b)**; a slightly postive deflection (compression) for ductile sample S_2 under low confinement (**Fig.6.1f**) but a significantly postive deflection (compression) of ε_H is observed for S_2 under high confinement (**Fig.6.2f**). The more specific characteristics of intermediate strain ε_H will be discussed in **Sections 6.3.2 and 6.4**. Another important observation is the coincidence of the intermediate (ε_H) and vertical (ε_V) strain for semi-ductile S_3 (**Fig.6.2d**), ductile S_5 (**Fig.6.2e**) and S_2 (**Fig.6.2f**) subjected to the high confinement, which would be discussed in **Section 6.4**.

The volumetric strains (ε_T) are correspondingly shown at top right conner (purple curve) for each test. Under the low confinement (**Fig.6.1**): i) for brittle PMMA (**Fig.6.1a**), and semi-brittle sample S_1(**Fig.6.1b**), the volumetric strain ε_T are abruptly increased to the maximum value (negative deflection) after the period of constancy, indicating a significant dilated behaviour; ii) for semi-brittle samples S_4 (**Fig.6.1c**), and semi-ductile sample S_3 (**Fig.6.1d**), the ε_T are more gradually developed (nonlinear dilated behaviour); iii) whereas for the ductile sample S_5 (**Fig.6.1e**) the ε_T keeps relatively constant from the initiation to the end of propagation; notably

for ductile sample S_2 (**Fig.6.1f**), the positive deflection of ε_T indicates a compressive manner of the deformation subjected to hydraulic fracturing.

Under the high confinement (**Fig.6.2**): i) for brittle PMMA (**Fig.6.2a**), the volumetric strain ε_T shows a more significant negative deflection (relatively linear after the breakdown) comparing to that under the low confinement; for semi-brittle sample S_1, the ε_T shows a significant negative deflection with strong nonlinearity (**Fig.6.2b**). ii) for semi-brittle S_4 (**Fig.6.2c**), semi-ductile S_3 (**Fig.6.2d**), and ductile samples S_5 (**Fig.6.2e**), the ε_T exhibits the analogous slightly negative deflection; ii) while for ductile sample S_2, volumetric strain ε_T is relatively constant from the early initiation until the end of propagation.

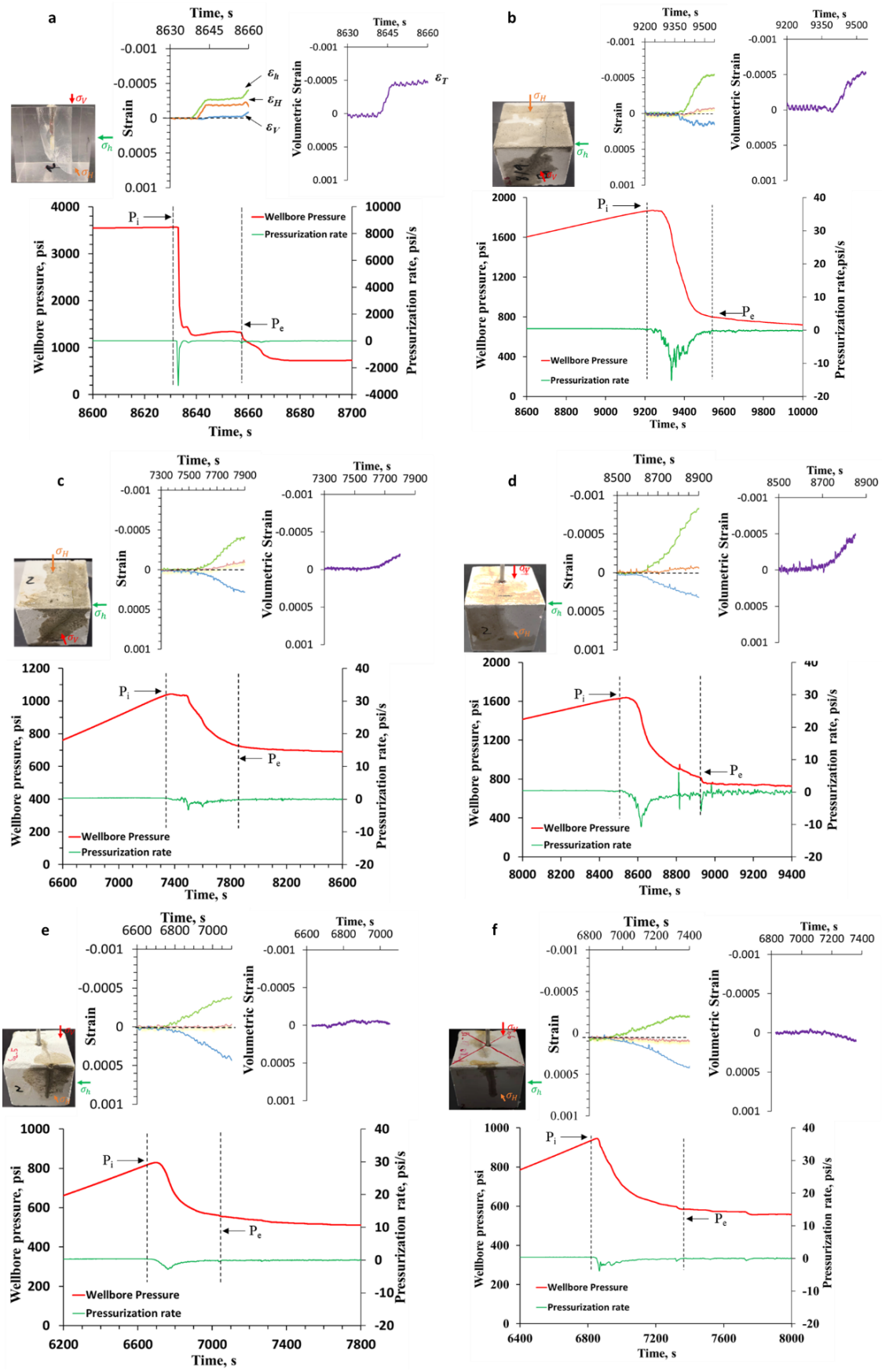

Fig.6.1 Synchronization of wellbore pressure and hydraulic fracture induced strain (vertical-ε_v, maximum horizontal (intermediate)-ε_H, and minimum horizontal-ε_h) under low confinement (6.5MPa ,

3MPa, and 1.5MPa): a) PMMA2 b) S_1 c) S_4 d) S_3 e) S_5 f) S_2. P_i and P_e denote the borehole pressure at the initiation and at the end of fracture propagation, respectively. The corresponding each sample after test are shown at the left. The volumetric strain (ε_v) are shown at the top-right. The tested samples are shown at the top-left.

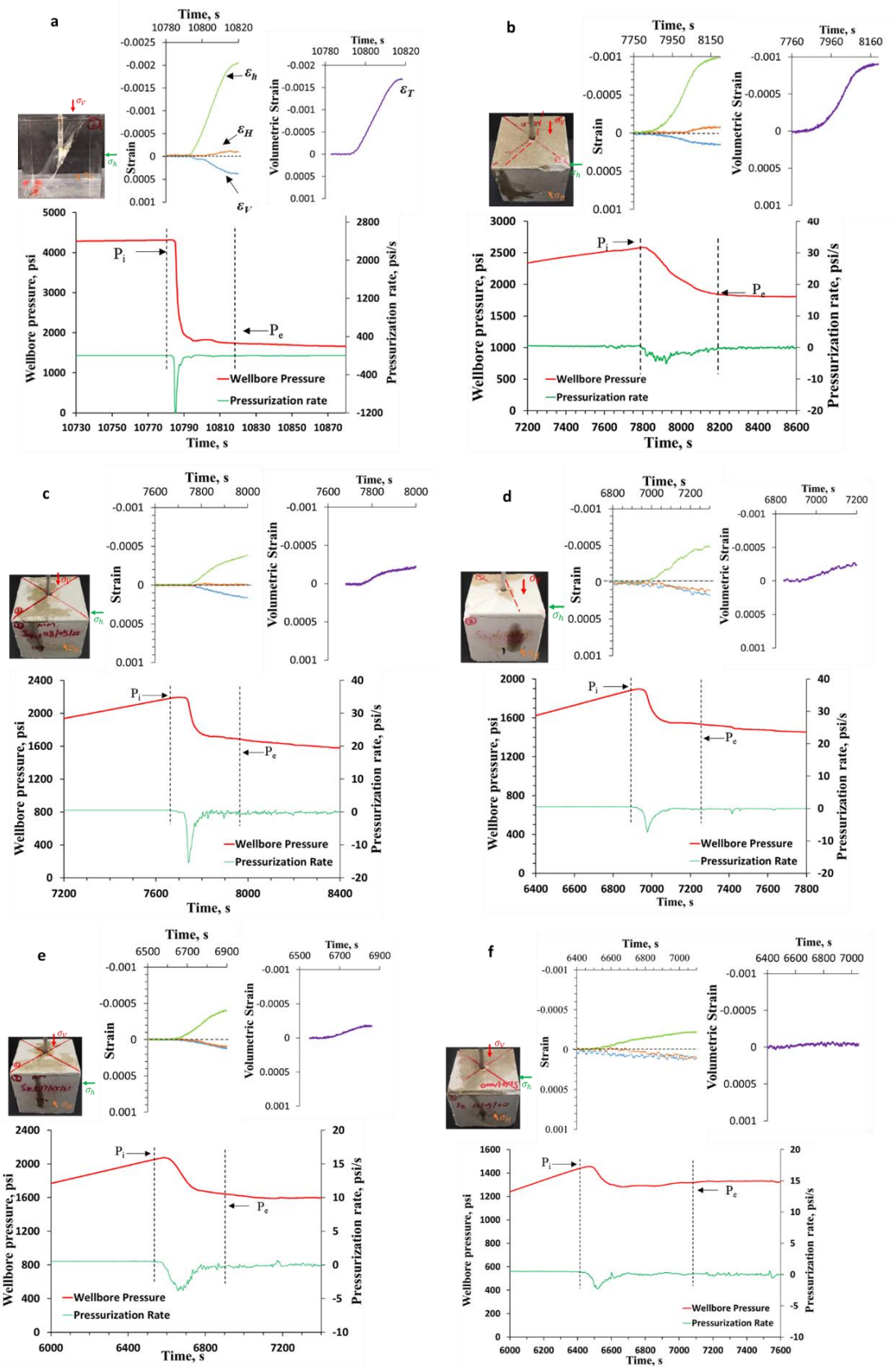

Fig.6.2 Synchronization of wellbore pressure and hydraulic fracture induced strain (vertical-ε_v, maximum horizontal (intermediate)-ε_H, and minimum horizontal-ε_h) under high confinement (15MPa , 10MPa, and 5MPa): a) PMMA4 b) S_1 c) S_4 d) S_3 e) S_5 f) S_2. P_i and P_e denote the borehole pressure at the initiation and at the end of fracture propagation, respectively. The corresponding each sample after test are shown at the left. The volumetric strain (ε_v) are shown at the top-right. The tested samples are shown at the right top.

6.3 Brittle-to-Ductile transition of hydraulic fracture and its associated deformation

According to the brittleness index (BI) quantification based on BI_{10} (Refer to **Chapter 5** or Feng et al (2022a)), the six types of samples are classified as brittle PMMA (BI=0.97), semi-brittle quartz-rich S_1 (BI=0.68), semi-brittle mixed-average S_4 (BI=0.57), semi-ductile calcite-rich S_3 (BI=0.44), the ductile clay-rich$_2$ S_5 (BI=0.38) and clay-rich S_2 (BI=0.35) under the low confinement. The same classification but different BI values under higher confinement: PMMA (BI=0.94), S_1 (BI=0.35), S_4 (BI=0.26), S_3 (BI=0.24), S_5 (BI=0.14), and S_2 (BI=0.094). First, the geometry of hydraulic fracture under both confinements are presented (**Section 6.3.1**). Moreover, we also discuss the characteristics of intermediate strain (ε_H) induced by hydraulic fracture propagation (**Section 6.3.2**). Finally, the correlation between fractured area and brittleness index (BI) is studied in **Section 6.3.3**.

6.3.1 Geometry and orientation of hydraulic fracture among different samples

The geometry of hydraulic fracture for different samples subjected to low confinement (i.e., 6.5, 3 , and 1.5MPa) are shown in **Fig.6.3.** The fractures are highly tilted with respect to both σ_H and σ_h for brittle PMMA (**Fig.6.3a)**, and semi-brittle rock S_1 **(Fig.6.3b)** and S_4 **(Fig.6.3c)**. For the semi-ductile S_3 (**Fig.6.3d**) and ductile rock S_5 (**Fig.6.3e**), the tilted angle are significantly reduced. In contrast, for ductile sample S_2 the fractures are nearly orthogonal to σ_h only (**Fig.6.3f**). Overall, it turns out a clear transition from highly titled (brittle) to orthogonal (ductile) fractures as the increase of ductility. This analogous phenomenon is also observed in the samples subjected to higher confinement (i.e., 15, 10 , and 5MPa) (**Fig.6.4**). The most interesting observation is the significant shear failure induced by hydraulic fracturing within PMMA: the geometry of hydraulic fracture (HF) is highly titled to ε_V and ε_h (**Fig.6.4a**), instead of inclining to ε_H and ε_h subjected to the lower confinement. Macroscopically, the geometry of hydraulic fractures are more planar/smooth under high confinement (**Fig.6.4**) rather than that of relatively tortuous fractures under the low confinement (**Fig.6.4**).

The experimental geometry of hydraulic fracture (HF) with respect to the brittle and ductile rocks (**Fig.6.3 and Fig.6.4**) are in good agreement with the numerical study recently performed by Ju et al. (2021): for brittle reservoir the fracture is severely titled and result in a nonplanar geometry (**Fig.6.5a**), while for the ductile reservoir the inclination of fracture is highly mitigated due to the tip plasticity (**Fig.6.5c**), resulting in an axisymmetrically short fracture. Their numerical results are shown to be more consistent with our experimental geometry of HF subjected to the high confinement (**Fig.6.4**).

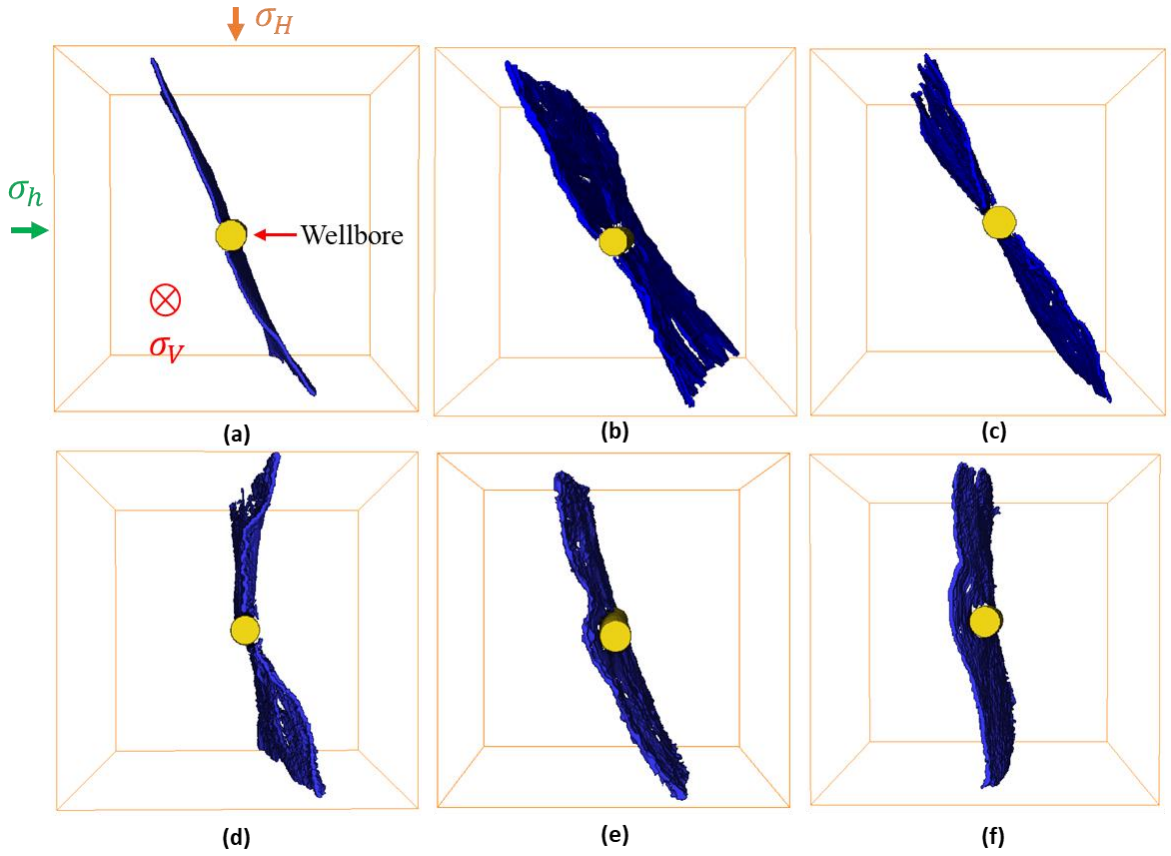

Fig.6.3 Geometry of hydraulic fracture from brittle to ductile transition a) PMMA b) the quartz-rich sample S_1 c) mixed-average S_4 d) calcite-rich S_3 e) clay-rich$_2$ S_5 f) clay-rich S_2 under 6.5, 3.0, and 1.5MPa

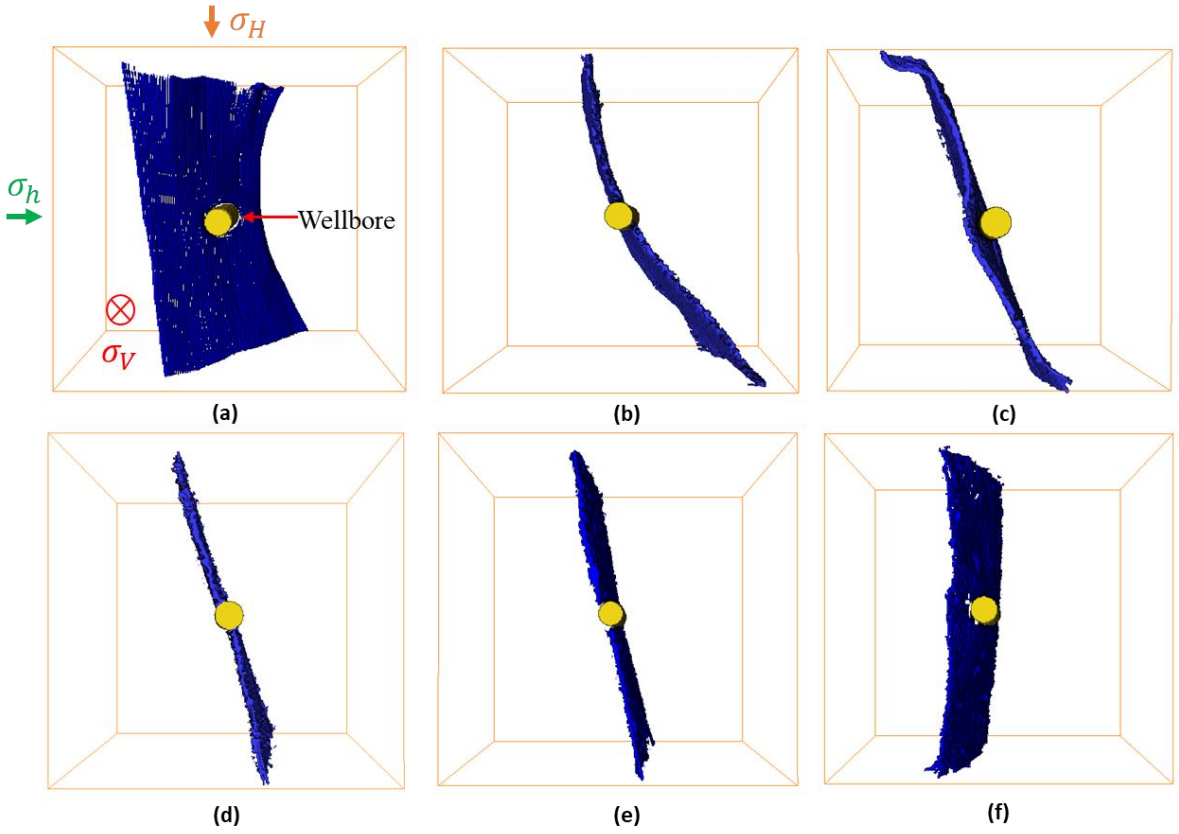

Fig.6.4 Geometry of hydraulic fracture from brittle to ductile transition a) PMMA b) the quartz-rich sample S_1 c) mixed-average S_4 d) calcite-rich S_3 e) clay-rich$_2$ S_5 f) clay-rich S_2 under 15, 10, and 5MPa

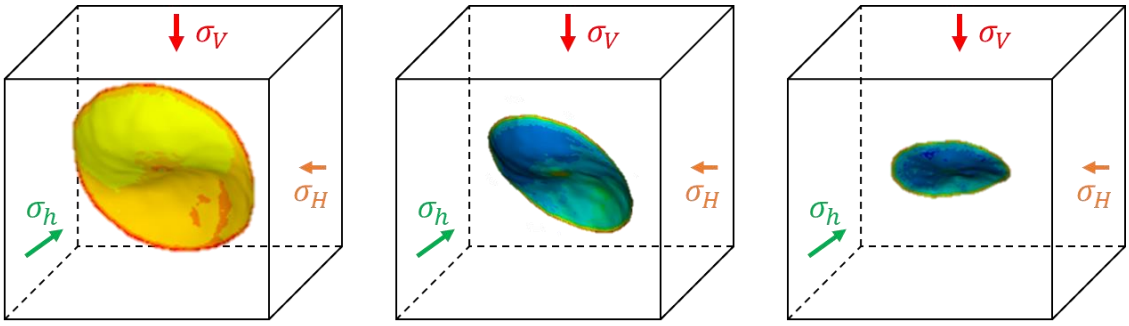

Fig.6.5 Numerical modelling of the morphology of hydraulic fracture from a) brittle, b) semi-brittle, and c) ductile reservoir under true triaxial stresses σ_v=30MPa, σ_H= σ_h=20MPa. Images modified from a 3D numerical work (Ju et al. 2021).

6.3.2 Intermediate strain (ε_H) transition

Refer to the hydro-mechanical data set (**Fig.6.1 and Fig.6.2**), the vertical strain ε_v shows a compression, and the minimum horizontal strain ε_h exhibits tension for all samples. However, the characteristics of intermediate strain ε_H are highly variable (depend on the sample types

and confinement) (**Fig.6.6**). For semi-ductile S_3, and ductile samples S_5 and S_2 under higher confinement (**Fig.6.6b**), the magnitude of ε_H is significantly larger than that of lower confinement (**Fig.6.6a**). In summary, the significant transitions of ε_H from the brittle to ductile samples are observed:

Under the low confinement (**Fig.6.6a**): the intermediate strain ε_H shows a significant tensile deflection for brittle PMMA; a moderate tensile deflection for semi-brittle rock sample S_1 and S_4; a slight deflection for semi-ductile S_3; a nearly constant ε_H for ductile S_5; while a slight compressive deflection for ductile rock sample S_2.

Under the high confinement (**Fig.6.6b**), the transition is analogous to the lower one: the negative deflection of ε_H becomes ease for PMMA, and still exhibits the highest value among all samples; for the rock samples (from S_1 to S_5), the moderate negative deflection of ε_H are observed in semi-brittle rock sample S_1 and S_4 , but a significant positive compression of ε_H are found in semi-ductile S_3 , ductile S_5 and S_2.

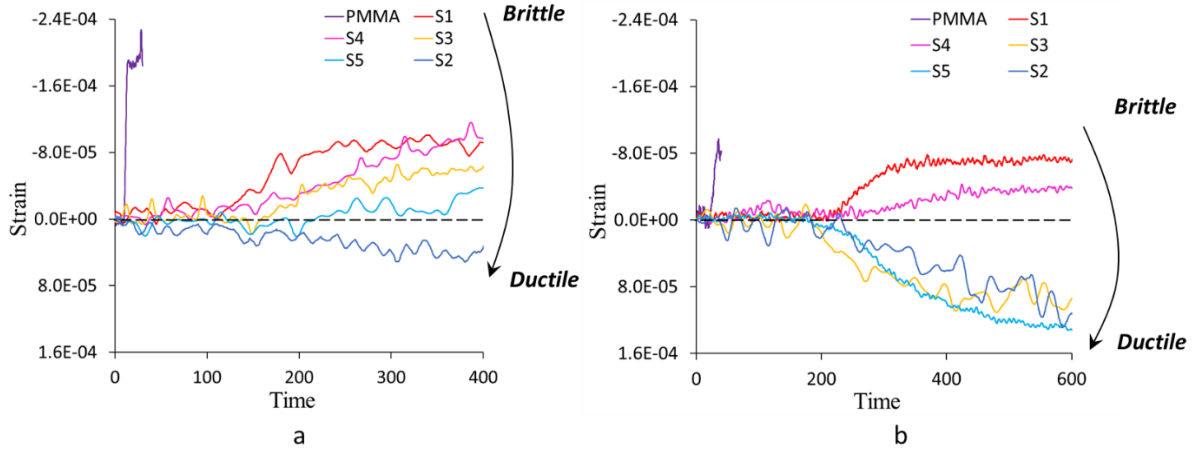

Fig.6.6 Transition of intermediate strain ε_H from brittle to ductile samples for a) low confinement b) high confinement

6.3.3 Fracturing Area verse BI

Ju et al. (2021) numerically studied the relation between fractured area and the brittleness index (BI) of shale reservoir. He showed that the fractured area is increased as the increase of BI. Here we quantify the hydraulic fractured area based on the CT images of tested rock samples (S_1 to S_5). We normalized the numerical (A_{TN}) and experimental fractured area (A_{FN}) based on the dimension of samples used in numerical modelling/experimental study, we then plot both A_{TN} and A_{FN} verse BI (**Fig.6.7**). Both A_{TN} and A_{FN} show an increased trend as the increase of BI. Notably, under the lower confinement, the fitting of A_{FN} and BI shows a second polynomial relation (negative coefficient). On the other hand, under the high confinement, the

analogous second polynomial relation (positive coefficients) are observed for both A_{FN} and A_{TN} verse BI; but their quantities are significantly different.

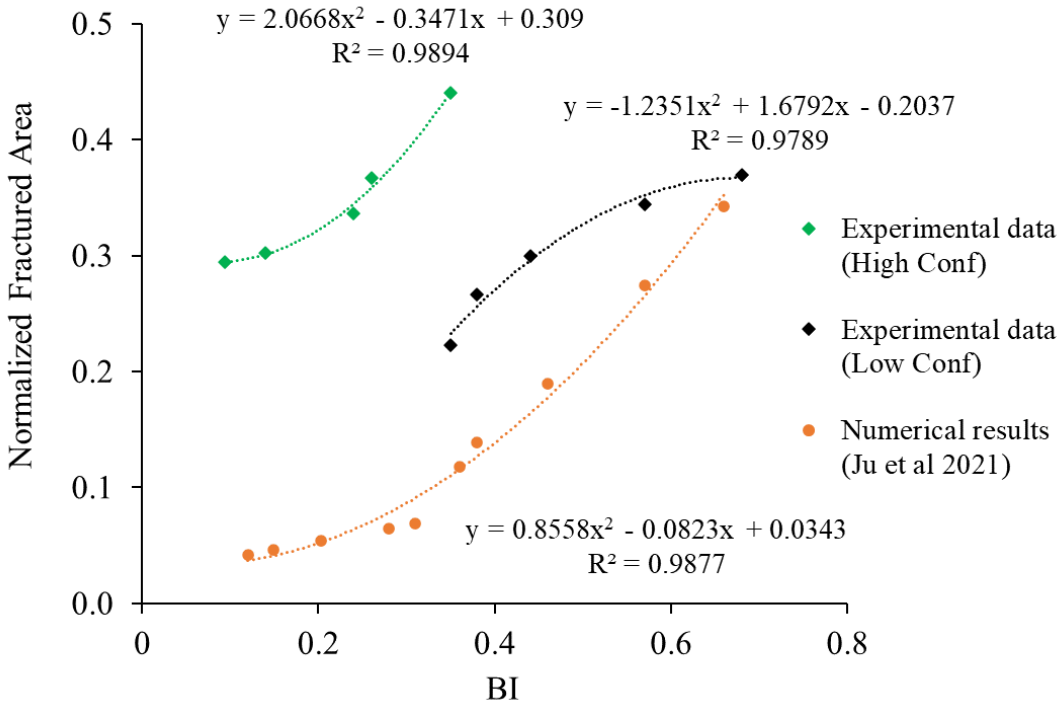

Fig.6.7 Normalized fractured area vs brittleness index (BI) based on our experimental results of low (6.5, 3.0, and 1.5MPa) and high (15, 10, and 5MPa) confinement; and the literature data from (Ju et al. 2021)

6.4 Viscoelastic Stress Relaxation

It is interesting to investigate possible mechanisms for the distinct characteristics of hydro-mechanical deformation subjected to true triaxial stress states (i.e., **Section 6.3.1 to 6.3.3**). Viscoelastic stress relaxation has been recognized as one of the primary reasons for higher magnitude of the minimum horizontal stress σ_h in unconventional shale gas reservoirs compared to the other layered clastic formations (Sone and Zoback 2014; Zoback, M. D., & Kohli, A. H. 2019; Mandal 2021).

The **Fig.6.8** illustrates how does the stress relaxation play a role in decreasing the stress anisotropy due to the increase of the magnitude of the least principal stress: as the significant increase of the minimum stress of the shale zone, the fracture growth is expected to be restricted. The creep compliance function based on power law model (among the constitutive models) has been accepted for sedimentary rock (Sone and Zoback 2014):

$$\varepsilon = \sigma B t^n \tag{6.1}$$

$$J(t) = B t^n \tag{6.2}$$

where J(t) is the creep compliance function described by axial strain ε(t) per unit value of differential stress σ; B and n are the fitting parameters referred to the creep constitutive parameters: B is the instantaneous elastic compliance in response to a unit stress step loading, n is the time-dependent exponent reflecting the rate of creep. These two parameters can be obtained based on the fitting of the creeping data, as it is shown in **Fig.D 1**.

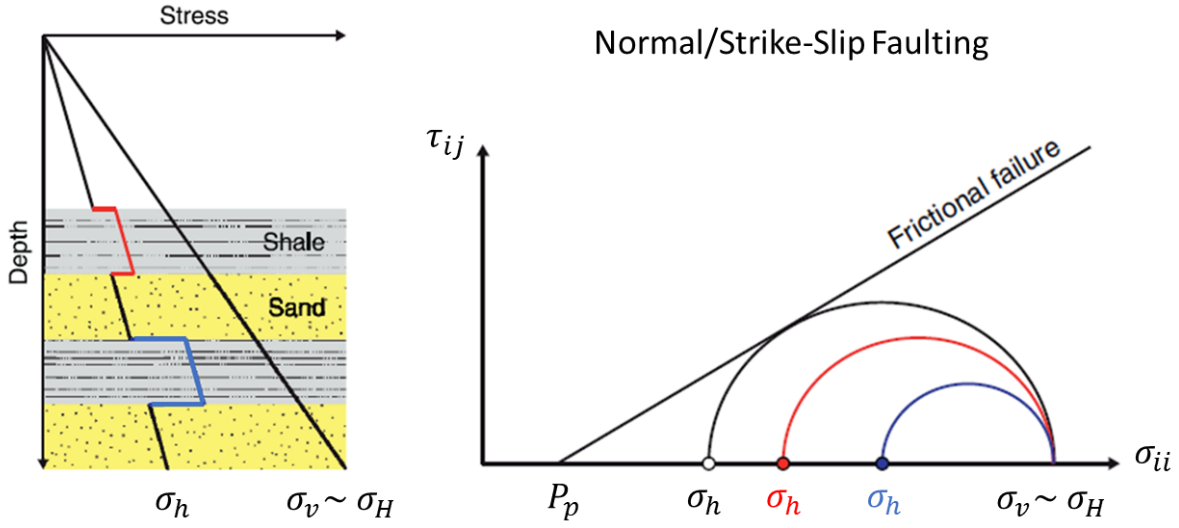

Fig.6.8 Schematic diagram illustrating how viscoelastic stress relaxation results in decreasing stress anisotropy due to increasing the magnitude of the least principal stress. Left: greater increment of S_{hmin} for the shale zone below rather than the minor increase of the S_{hmin} above the sand zone, which provide a barrier for fracture growth. Right: The Mohr-circle diagram in response to the viscoelastic stress relaxation (modified from Zoback, M. D., & Kohli, A. H. (2019)). Note the minimum horizontal stress $\sigma_3 = \sigma_h$ in this schematic.

Fig.6.9 shows the amount of different stress would be remained on the samples (PMMA, S_1 to S_5) after one-day from application of a one-dimensional strain step of 0.02. This value is selected based on our axial strain data of our samples under both triaxial (**Fig.6.9**) and true-triaxial compressive tests (**Fig.D 1**). The contour lines represent the predicted reciprocal stress relaxation after one-day with the strain step (**Fig.6.9**): the highest magnitude of contour (e.g.,100MPa) indicates the stress accumulation is much faster than stress relaxation caused by viscoelastic deformation, which is usually observed in brittle rocks (Zoback, M. D., & Kohli, A. H. 2019); while the lowest magnitude of contour (e.g.,10MPa) reveals that the stress accumulation is much lower than the viscoelastic stress relaxation, which is evident in ductile

rocks (Zoback, M. D., & Kohli, A. H. 2019). The contours intersected with the horizontal axis represents the purely elastic stress magnitude resulted from the strain. It can be seen that the samples-PMMA and S_1 are nearly located at the contour with the highest differential stress (100MPa), while the sample S_2 is at the lowest one (10MPa); and the samples S_3 ,S_4 , and S_5 are located in the between (from 30 to 40MPa). The repeatability of these results are shown in **Fig.6.9b**, although the difference are existed for the value of B and n (e.g., S_{2_2}, PMMA_2), the result of contour line shows the good repeatability. A clear brittle-to-ductile transition among our tested samples are indicated from **Fig.6.9**. These results of viscoelastic stress relaxation not only explain the distinct characteristics of deformation among the tested samples (PMMA and S_1 to S_5) subjected to hydraulic fracturing (**Fig.6.*3*** and **Fig.6.*4***), but also verified our BI prediction (see **Fig.5.*3***) based on our proposed BI model (i.e., BI_9 and BI_{10} listed in **Table 2.1**).

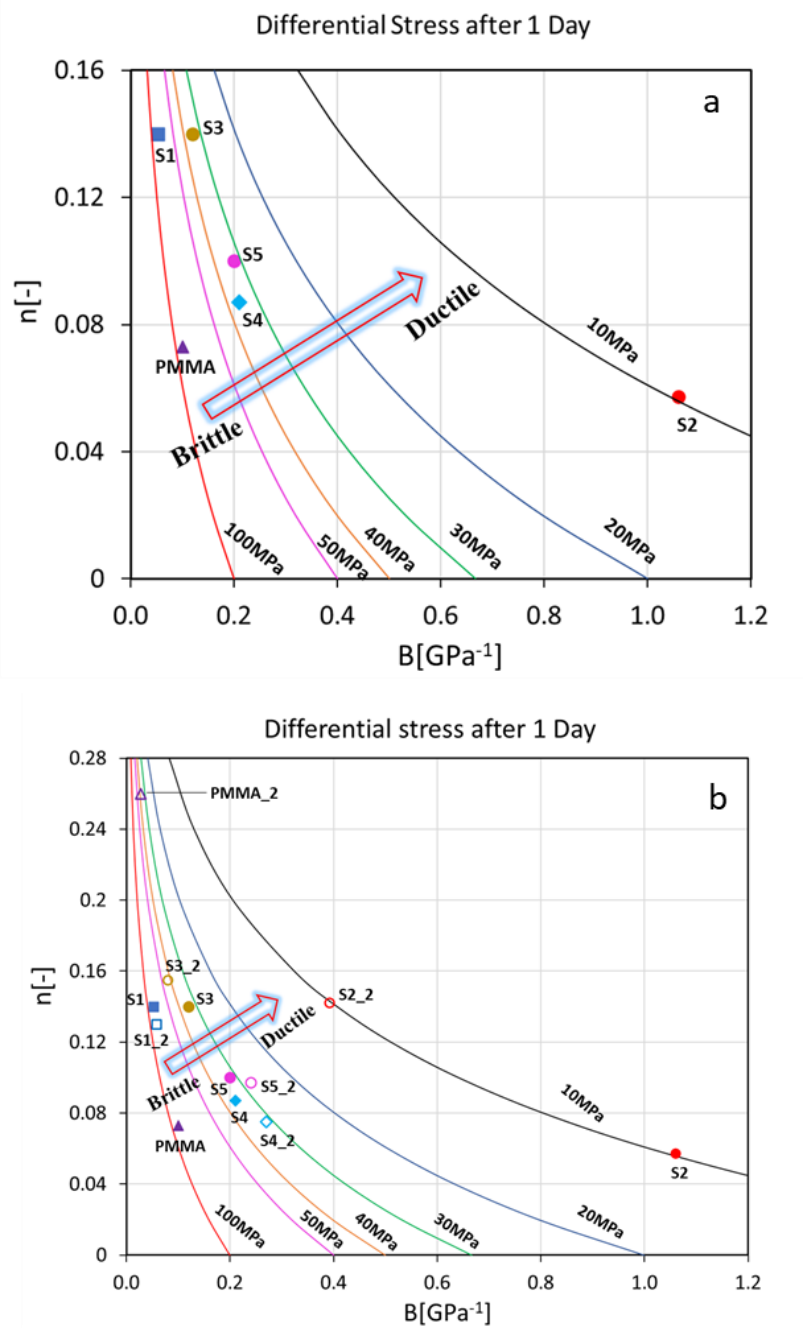

Fig.6.9 Differential stress response to change of the strain (0.02) for tested samples PMMA, and S_1 to S_5 after 1 Day under confinement of 15, 10, and 5MPa: a) representative stress relaxation results (see the creep data shown in **Fig.D 1**; b) full results of stress relaxation confirming the repeatability.

6.5 Discussion

6.5.1 Hydraulic fracture induced failure from low to high confinement

The characteristics of hydro-mechanical deformation can be indicated by the 3D strain (vertical-ε_v, intermediate-ε_H, and minimum horizontal-ε_h, and the volumetric strain

(ε_T))(**Fig.6.1** and **Fig.6.2**). Under the lower confinement, for brittle PMMA (**Fig.6.1a**), and semi-brittle samples S_1 (**Fig.6.1b**) the volumetric strain and small portion of axial strain indicate the fracture deformation are relatively localized. On the other hand, for semi-brittle S_4 (**Fig.6.1c**), and semi-ductile S_3 (**Fig.6.1d**) the volumetric strain (ε_T) experiences more nonlinearity; while for ductile samples S_5 (**Fig.6.1e**) and S_2 (**Fig.6.1f**), the relative constant or compressive ε_T reveal that nonlocalized (spatially extended) plastic deformation are expected to be developed during the fracture propagation within the sample. Under the higher confinement, the failure of PMMA(**Fig.6.2a**) is dominated by vertical shear dilation (PMMA), while for semi-brittle rock S_1 (**Fig.6.2b**) the lateral shear-tensile opening is dominated; the more pronounced strain is attributed to higher breakdown/net pressure. In contrast to the significantly dilated volumetric strain (ε_T) observed for PMMA and S_1, the volume of the samples are only slightly dilated for semi-brittle S_4 (**Fig.6.2c**), semi-ductile S_3 (**Fig.6.2d**), and ductile sample S_5 (**Fig.6.2e**); while it stay relatively constant for ductile sample S_2 (**Fig.6.2f**). These observations indicate that the plastic deformation are highly nonlocalized within semi-ductile S_3, and ductile samples (S_5 and S_2) where the compression of intermediate (ε_H) and vertical strain (ε_V) are highly coincided (**Fig.6.2d,e, and f**). Such evidence of nonlocalized (spatially extended) plastic deformation induced by fracture propagation (stress/hydraulic) are also observed and proven in the numerical/experimental studies (Brantut et al. 2011; Huang and Chen 2021; Huang and Ghassemi 2016; Liu and Brantut 2022; Parisio et al. 2021; Ramos Gurjao et al. 2022; Richard et al. 2021; Schmidt et al. 2022; Tan et al. 2021; Vinci et al. 2014; Wrobel et al. 2022; Zhang et al. 2020).

6.5.2 Role of intermediate stress (σ_H) in hydraulic fracture propagation

The intermediate stress σ_H is considered as an important parameter for the stress intensity factor (K_{HF}) if the geometry of hydraulic fracture (HF) is inclined to directions of both horizontal stresses, which is often observed in the laboratory or field (Lhomme 2003; Sarvaramini et al. 2019; Yu et al. 2022). The previous studies demonstrated the significant role of σ_H in the mechanical properties, and associated failure modes induced by the elevated mechanical stresses on sandstone and shale (Minaeian 2014). In this study, the intermediate strain ε_H induced by the coupled hydraulic and mechanical force are highly variable regarding the sample types, and the confinement. The deflection of ε_H exhibits a clear brittle-to-ductile transition among the tested samples especially for the higher confining case (**Fig.6.6**). Noteworthily, for semi-ductile and ductile samples subjected to the higher confinement, the ε_H

are significantly compressive after the early initiation stage (i.e., 200s), then starts to coincident with the vertical strain (ε_V) (**Fig.6.2d,e and f**). This observation can be explained by the more pronounced nonlocal (spatial extend) deformation induced by hydraulic fracture in the semi-ductile/ductile samples subjected to higher confining stresses (as discussed in **Section 6.5.1**).

6.5.3 Role of BI in geometry of hydraulic fracture

The representative transitional geometry of hydraulic fracture for both brittle and ductile samples **(Fig.6.3 and Fig.6.4)** are in good agreement with the numerical study **(Fig.6.5)** performed by Ju et al. (2021). The mechanisms behind these interesting observations are worthily to be discussed. In this section, we will concentrate on the possible mechanisms leading to the more representative transitional geometry under the higher confinement (i.e., 15, 10 , and 5MPa) (**Fig.6.2**).

Fig.6.10 shows a typical shear failure of brittle materials induced by true tri-axial stresses compression (TTSC) i.e., $\sigma_v > \sigma_H > \sigma_h$ (Minaeian 2014; Rahjoo and Eberhardt 2021). Prior to this failure, assume a fictitious weak plane (normal faulting regime) is formed within the sample subjected to the stresses (**Fig.6.10**). Noteworthily, the fictitious weak plane is different from the theoretical weakest plane for propagation of a hydraulic fracture (i.e., the one perpendicular to minimum horizontal stress). Based on the geometry observed in our tested samples **(Fig.6.4**), the representative schematic of brittle to ductile transition for the hydraulic fracture (HF) subjected to the designed stress regime are displayed in **Fig.6.11**.

For the brittle PMMA the HF propagates along to the normal faulting regime (**Fig.6.2a Fig.6.10,** and **Fig.6.11a**), which is mainly attributed to **(i)** the energy effectively converted from highly pressurized fracturing fluid causes high stress concentration near the crack tip and **(ii)** the higher stress anisotropy accumulated from the principal stress magnitudes. While for semi-brittle rocks S_1 and S_4, the vertical shearing failure observed in PMMA is highly eased, instead, the hydraulic fracture is mainly inclined to both intermediate stress σ_H and the least principal stress σ_h (**Fig.6.11b**). This alleviation could be attributed to: **(i)** the slightly mitigated stress concentration near the fracture tip due to the strain softening (Ju et al. 2021; Papanastasiou 1997) and **(ii)** the slightly reduced stress anisotropy due to the viscoelastic stress relaxation. On the other hand, for semi-ductile (S_3), and the ductile samples (S_5 and S_2), the HF is nearly perpendicular to the least principal stress σ_h (**Fig.6.11c** and **d**). This is attributed to **(i)** the significant tip plasticity and softening behaviour highly reduce the stress concentration (Feng et al. 2020; Ju et al. 2021; Papanastasiou 1997), which significantly reduces the kinematic

energy transformation from the accumulated injection energy; and **(ii)** the significant viscoelastic stress relaxation causes the increase of the least principal stress (**Fig.6.9**), resulting in more isotropic stress magnitude in these ductile formations (Zoback, M. D., & Kohli, A. H. 2019).

The abovementioned mechanisms (e.g., crack tip plasticity, viscoelastic stress relaxation) clearly explain why the geometry of hydraulic fracture always propagated along the theoretical weakest plane in semi-ductile/ductile samples, i.e., nearly perpendicular to the minimum horizontal stress **(Fig.6.11c or d)**, without being significantly affected by the fictitious weak plane induced by the deviatoric stress state ($\sigma_V > \sigma_H > \sigma_h$) shown in **Fig.6.10**. Notably, for the materials (S_1 to S_5) tested in this study , the macroscopic geometry of hydraulic fractures subjected to high confinement **(Fig.6.4)** are more planar than that of low confinement **(Fig.6.3)**, which is attributed to the higher resistance of fracture propagation as the increase of confinement/ductility.

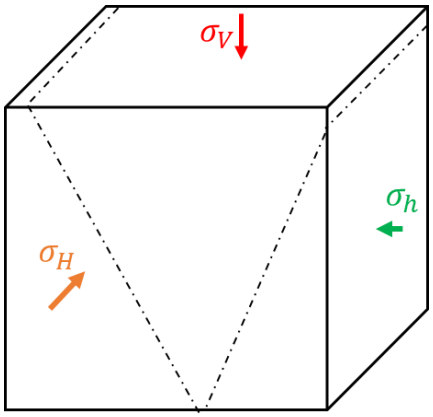

Fig.6.10 The failure mode of brittle materials under true triaxial stress compression i.e., $\sigma_v > \sigma_H > \sigma_h$ (Minaeian 2014; Rahjoo and Eberhardt 2021).

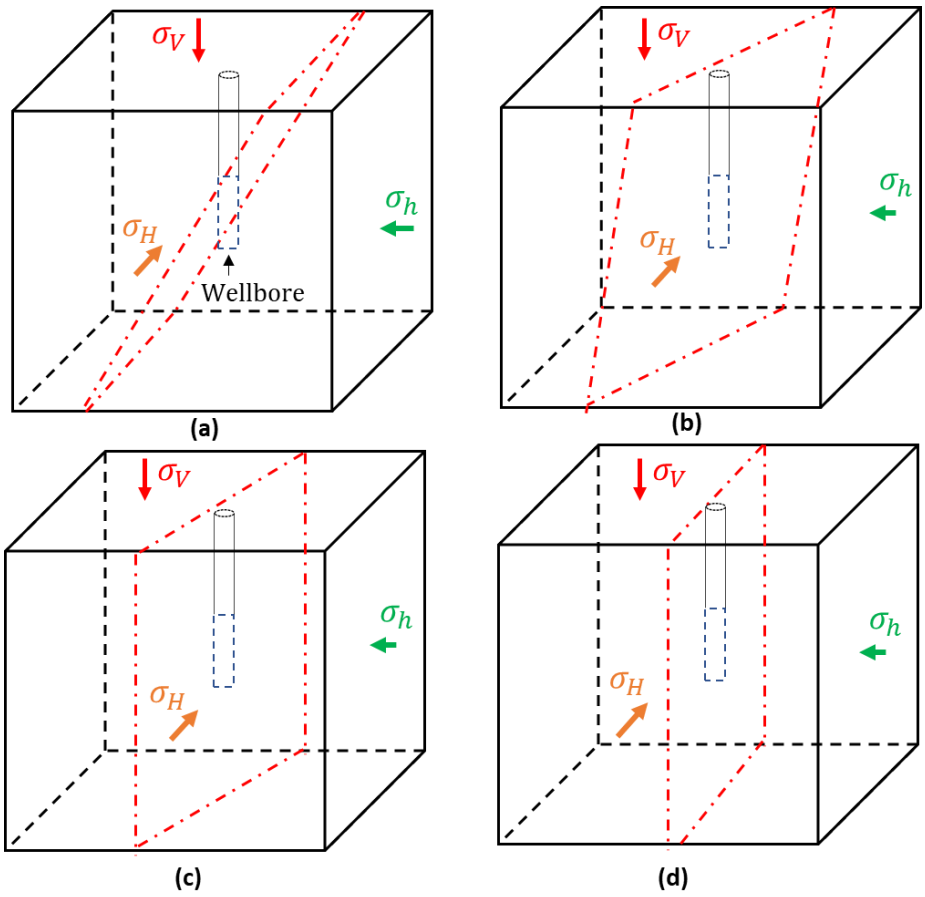

Fig.6.11 Representative Geometry of hydraulic fracture from brittle to ductile transition: **a)** brittle PMMA (under high confinement) **b)** brittle PMMA (under low confinement) or brittle/semi-brittle rock **c)** semi-ductile rock **d)** ductile rock. Note: the failure plane shown above is a simplified diagram, not necessarily indicating the fracture will exactly follow that plane or penetrated to the boundary of sample.

6.5.4 Role of BI in fracturing area

laboratory results indicated that the fractured area (A_{FN}) are reduced from brittle to ductile samples subjected to both low and high confinement (**Fig.6.7**), which is in good agreement with the numerical study recently performed by (Ju et al. 2021). As shown in **Fig.6.7**, the experimental results subjected to the high confinement (A_{FN} verse BI) shows an analogous polynomial relation comparing to the numerical results (A_{TN} verse BI); regardless of their quantities. For laboratory experiments, the limited sample size and continuously injected energy allow the fluid-driven fractures penetrate the boundary of sample, while the HF are retained within the boundary of numerical model due to the early termination of fracture propagation in ductile reservoirs (Ju et al. 2021).

Interestingly, for the same type of tested sample, the fractured area (A_{FN}) subjected to high confinement (15MPa, 10 MPa, and 5MPa) are larger than that of lower confinement (6.5MPa,

3 MPa, and 1.5MPa) (**Fig.6.7)**, although the brittleness index (BI) of former one is reduced. This could be attributed to: (i) higher deviatoric horizontal stress exerted on the samples subjected to high confinement (Van Dam and De Pater 1999; Van Dam et al. 2000a). (ii) higher stress concentration near the fracture tip due to the higher breakdown/propagation pressure. This coupled mechanism causes the fracture to propagate in a manner of relatively higher effective stress and sufficient propagating time, resulting in a more tortuous fracture with relatively rougher surface in the view of meso-scale (**Fig.6.12**).

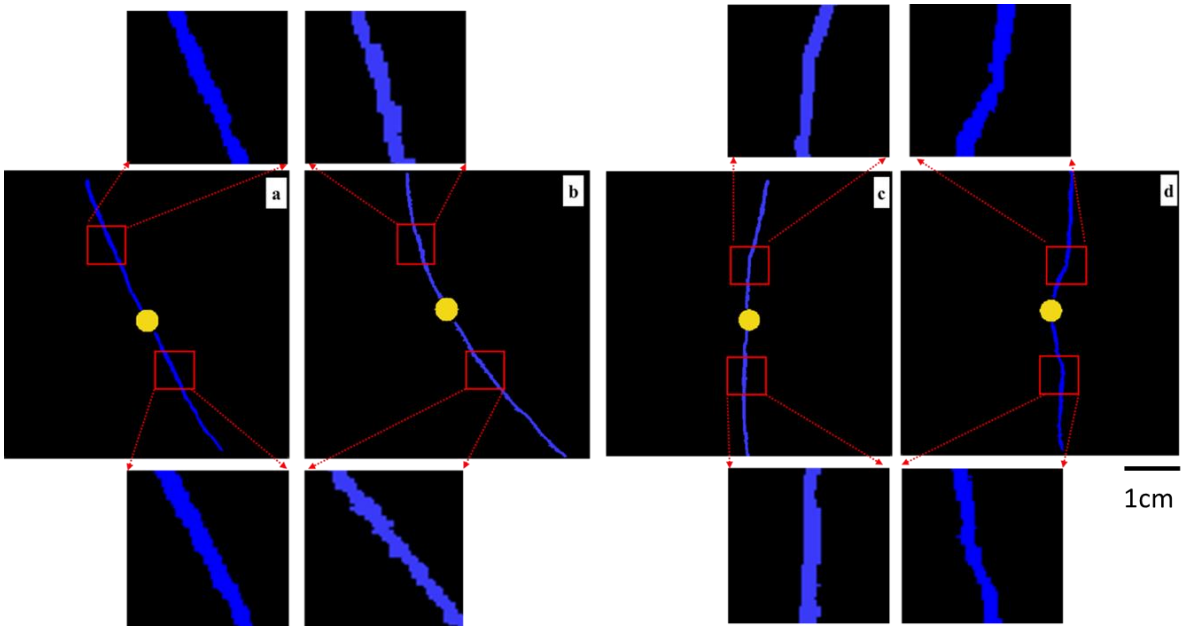

Fig.6.12 CT images of hydraulic fracture in semi-brittle rock S_1 under a) low and a) high confinement; ductile rock S_2 under c) low and d) high confinement

6.6 Conclusion

In this chapter, we discuss the hydro-mechanical data on five types of rock samples in addition to PMMA, which represents the extreme brittle reference. The samples were subjected to true triaxial stress conditions (TTSC), and during fluid injection wellbore pressure and the three-dimensional (3D) strains induced by hydraulic fracture propagation were simultaneously monitored. After each experiment, the fractured sample was imaged using X-ray Computed Tomography (XCT); the 3D images were used to quantitatively evaluate the morphology and area of the induced hydraulic fracture (Avizo software). The analysis of stress relaxation based on creep data indicates the viscoelastic behavior should be considered for analysis of the stress state or deformation of different lithological layers in the field, rather than the simplified

elasticity. These experiments are designed to shed light on the hydraulic fracturing response as a function of depth for a wide range of engineering applications.

The interpretation of the hydro-mechanical data reveals that:

(i) The non-localized deformation induced by hydraulic fracturing in a semi-brittle sample (e.g., S_4), a semi-ductile sample (e.g., S_3), and a ductile sample (e.g., S_5 and S_2) are significantly enhanced at higher confinement (mean compressive stress) (**Fig.6.1and Fig.6.2**). However, for the extremely brittle PMMA (**Fig.6.1a and b)**, and the semi-brittle sample S_1 (**Fig.6.2a and b),** the failure is dominated by localized shear-dilation at both low and high confinement.

(ii) For a normal faulting regime (i.e., $\sigma_v > \sigma_H > \sigma_h$), the volumetric strain ε_T and intermediate strain ε_H are exhibited from tensile deflection to positive compression when transiting from a brittle to a ductile regime (**Fig.6.*1*, Fig.6.*2*, and Fig.6.6)**; this phenomenon is enhanced as the increase of confinement.

The variable inclined angle (high-to-low) of HFs are observed from brittle/semi-brittle samples to semi-ductile/ductile samples:

(i) For the extremely brittle PMMA under high confinement, extremely high stress concentration near the crack tip and the higher stress anisotropy leads to a strong hydro-shearing fracture (see **Fig.6.4a or Fig.6.11a**), which is consistent with a normal faulting regime **(Fig.6.10)**.

(ii) For the semi-brittle samples (S_1 and S_4), the moderate plastic softening reduces the stress concentration at the fracture tip and slightly reduced stress anisotropy inhibit vertical hydro-shearing, but promoting horizontal inclined hydro-dilating fractures (see **Fig.6.4b and c; Fig.6.11b and c**).

(iii) For the semi-ductile sample S_3 and the ductile samples (S_5 and S_2), **(i)** the significant plastic softening behaviour at the fracture tip reduces the near-tip stress concentration (Feng et al. 2020; Ju et al. 2021; Papanastasiou 1997; Parisio et al. 2021), which significantly dissipates the effective propagation energy; **(ii)** the significant viscoelastic stress relaxation causes the increase of the least principal stress, resulting in more isotropic stress magnitude in these ductile formations. These mechanisms are thought to be the cause of the highly mitigated inclination of hydraulic fractures observed in samples S_3 (**Fig.6.3d and Fig.6.4d; Fig.6.11c**) and S_5 (**Fig.6.3e and Fig.6.4e;**

Fig.6.11c), which contrasts with the fracture induced in sample S_2, i.e., nearly perpendicular to the minimum horizontal stress (**Fig.6.3f, Fig.6.4f and Fig.6.11d**).

The correlation between normalized fractured area (A_{FN}) and brittleness index (BI) indicates that:

(i) The measured surface area of the hydraulic fractures is reduced when transiting from the brittle to the ductile regime, regardless of the confinement (**Fig.6.7**), which is in good agreement with the numerical study reported by Ju et al. (2021).

(ii) Notably, for the same type of sample under high confinement (15MPa, 10 MPa, and 5MPa), the fractured area (A_{FN}) is shown to be larger than that for lower confinement values (6.5MPa, 3 MPa, and 1.5MPa), despite the fact that the brittleness index (BI) is significantly reduced when confinement is significantly higher. This is attributed to a more tortuous fracture with a relatively rougher surface at high confinement (**Fig.6.12**).

Chapter 7

Conclusions and Recommendations

7 Conclusions and Recommendations

Summary and Conclusions

This thesis studies the role of brittleness index (BI) in hydraulic fracture initiation and propagation mechanisms in tight sedimentary rock using theoretical and experimental approaches. We aim to develop a robustly analytical model to quantify the BI subjected to hydraulic fracturing. We also interpret the lab-scale experimental data regarding to hydraulic fracture attributes within different types of synthetic rock samples under true triaxial stress conditions (TTSC) (e.g., the induced strain, orientation, fracturing area, roughness of the fracture surface, etc). By integrating the experimental data and the quantified BI of testing samples, we aim to understand the role of brittle/ductile behavior in hydraulic fracture growth mechanisms.

From the theory development:

- The underground brittle/ductile behavior of hydraulic fracture not only depends on the inherent rock properties, but also the multiple parameters subjected to hydraulic fracturing, such as failure modes, injection rate, fluid viscosity, stress/temperature conditions (Economides and Nolte 1989; Papanastasiou 1997; Bunger 2005; Wu 2006; Sarmadivaleh 2012; Gischig and Preisig 2015; Salimzadeh and Khalili 2015; Liu et al. 2020b; Liu 2021; Parisio et al. 2021; Feng et al. 2022). Incorporating all these parameters into a model is complicated and may lead to uncertainties for the evaluation. We therefore develop new brittleness index (BI) models based on hydro-mechanical energy criteria subjected to hydraulic fracturing (**Chapter 2**), in which the BI is quantified based on schematic energy partitioning (BI_8), cohesive energy concept (BI_9), and the direct calculation of aseismic deformation energy (BI_{10}). As a comparison/benchmark, the BI models from literature ($BI_{1\text{-}7}$ in **Table 2.1**) are also involved for quantification.
- To calculate the hydraulic fracturing area (A_d) used for quantifying the hydro-mechanical deformation (BI_{10}), a robust analytical model R_d for hydraulic fracture propagation based on Poiseuille's law and scaling analysis is proposed and validated through literature data (see **Chapter 3** or Feng et al 2022c). The history match of literature data based on our model R_d and the other analytical models demonstrate the robust applicability of R_d at laboratory.

From the laboratory study:

- We conducted conventional rock mechanical tests according to ISRM, time-dependent deformation (creep) tests and the lab-scale hydraulic fracturing experiments on geomaterials exhibiting a wide range of mechanical properties (**Chapter 4**): cubic samples 50x50x50 mm^3 in size are subjected to true triaxial stresses with either a low (σ_v = 6.5 MPa, σ_H =3 MPa, and σ_h =1.5MPa), and a high (15 MPa, 10 MPa, and 5MPa) confinement (Feng et al 2022b). The wellbore pressure and three-dimensional (3D) strains induced by hydraulic fracturing are monitored and interpreted. The geometry and surface roughness of hydraulic fracture are documented by X-ray CT images.
- The brittleness index (BI) is quantified based on the ten analytical models (i.e., BI_1 - BI_7 from literature, BI_8- BI_{10} developed in this study) and our experimental data (**Chapter 5**). The limitations of models BI_{1-6} applied in hydraulic fracturing (HF) are discussed. The results indicate that the models of BI_7 (Papanastasiou et al. 2016), and our newly developed BI_9, and BI_{10} are qualitatively consistent among the tested samples exhibiting a wide range of rheology. Quantitatively, the use of BI_7 for BI prediction from low to higher confinement need to be carefully considered. Both BI_9 and BI_{10} are shown to be stress-dependent, however, the BI value based on BI_9 are relatively indistinguishable among the semi-ductile sample calcite-rich S_3, and the ductile clay-rich S_2 and S_5. The results (**Fig.5.3**) reveal that the BI_{10} is capable of capturing the brittle-to-ductile behaviour within a wide range of rheological samples subjected to hydraulic fracturing under variable confinement.
- By integration of the BI results (BI_{10}) and experimental measurement of hydraulic fracture attributes (**Chapter 6**), we found that (i) The orientation angle of hydraulic fracture is highly inclined to the maximum horizontal σ_H (or vertical σ_v) stresses in brittle/semi-brittle samples PMMA S_6, quartz-rich S_1, and mixed-average S_4; the inclination is reduced for that of semi-ductile samples calcite-rich S_3, and ductile clay-rich$_2$ S_5; nearly reaches to zero (parallel to σ_H and σ_v) for ductile samples clay-rich S_2. This observation is well agreed with the numerical study (Ju et al. 2021). This is attributed to the significant plasticity in the vicinity of the fracture tip diffusing the stress concentration, and the reduce of stress anisotropy caused by stress relaxation. (ii) The intermediate stress plays a profound role in HF propagation and associated rock deformation, which is indicated by the nonlocalized volumetric strain (ε_T) in semi-ductile/ductile samples S_3, S_2, and S_5. (iii) The fracturing area decreases as the decrease of BI among different samples under both low and higher confinement. In addition, for

the same type of sample, the tortuosity and roughness of fracture surface leads to a larger surface area of hydraulic fracture at the higher confinement rather than that of low confinement.

- The results of viscoelastic stress relaxation (**Section 6.4**) not only explain the distinct characteristics of deformation among the tested samples (PMMA and S_1 to S_5) subjected to hydraulic fracturing (**Fig.6.*1*, Fig.6.*2*, Fig.6.*3*, Fig.6.*4***), but also verified our BI prediction (**Fig.5.*3***) based on our proposed BI model (i.e., BI_9 and BI_{10} listed in **Table 2.1**).
- The outcome of this research can facilitate not only laboratory and numerical studies, but also the field applications where the underground brittle-to-ductile behaviour are required to be considered prior to the implementation of hydraulic fracturing.

Recommendations and Perspectives

- Our analytical R_d model is validated through lab-scale experimental data set; Field assessment/application is highly recommended, where the radius predicted from R_d can be applied for the comparison/calibration of fracture growth monitoring based on active/passive seismic data interpretation.
- For the benchmark of the BI model definition, the synthetic samples used for this experimental study are homogeneously isotropic. Further experimental or numerical study regarding to anisotropic and heterogeneous (natural) samples are recommended.
- Numerical study is recommended to be conducted for comparison and upscaling purpose of the quantities, observations, and conclusions obtained from this analytical/experimental study.

Appendices

Appendix A: Mathematic transformation (Eq.2.13) and the validation of hypothesis (Eq.2.14)

A.1. Derivation of equation (10)

The total derivative of fluid pressure $p_f(r,t)$ as function of time t can be written as:

$$\frac{dp_f(r,t)}{dt} = \frac{\partial p_f(r,t)}{\partial r}\frac{\partial r}{\partial t} + \frac{\partial p_f(r,t)}{\partial t}\frac{\partial t}{\partial t} \quad \text{, with } 0 < r < R_f < R. \tag{A1}$$

At $r = R_f(t)$, Eq.(A1) can be rewritten as

$$\left.\frac{dp_f(r,t)}{dt}\right|_{r=R_f(t)} = \left.\frac{\partial p_f(r,t)}{\partial r}\right|_{r=R_f(t)}\frac{dR_f(t)}{dt} + \left.\frac{\partial p_f(r,t)}{\partial t}\right|_{r=R_f(t)} \tag{A2}$$

At any time, assume a lag exists between the fluid front $r = R_f(t)$ and the fracture tip, ensuring the physical coherence of the mathematical solution (Garagash and Detournay 2000; Detournay 2004; Garagash 2019; Liu and Lecampion 2021), where the pressure is essentially zero (if not negative and cavitation can occur); thus, at all times during fracture propagation $\left.\frac{dp_f(r,t)}{dt}\right|_{r=R_f(t)} \cong 0$, and Eq.(A2) becomes

$$\left.\frac{\partial p_f(r,t)}{\partial r}\right|_{r=R_f(t)}\frac{dR_f(t)}{dt} + \left.\frac{\partial p_f(r,t)}{\partial t}\right|_{r=R_f(t)} \cong 0 \tag{A3}$$

Combining Eq.(A3) and Eq.(10) in the main text yields

$$\left(\frac{dR_f(t)}{dt}\right)^2 \cong \frac{w^2}{12\,\mu_f}\left.\frac{\partial p_f(r,t)}{\partial t}\right|_{r=R_f(t)} \tag{A5}$$

A.2. Assumption on the fluid pressure time derivatives

Eq.(A5) requires the knowledge of the partial derivative of the fluid pressure near the fluid front in a propagating hydraulic fracture $\left.\frac{\partial p_f(r,t)}{\partial t}\right|_{r=R_f(t)}$. This data is often inaccessible in practice, neither in the laboratory nor in the field. The key accessible parameter is the wellbore pressure, corresponding essentially to the fluid pressure at the inlet of the fracture.

Based on the few evaluations of fluid pressure profiles along a propagating hydraulic fracture available in the literature, we hypothesise that at each time increment, the change with time in

fluid pressure at the fluid front $\left.\frac{\partial p_f(r,t)}{\partial t}\right|_{r=R_f(t)}$ is linearly related to the change with time of the fluid pressure at the fracture inlet (wellbore) $\left.\frac{\partial p_f(r,t)}{\partial t}\right|_{r=o}$, with a time-dependent proportionality coefficient $-\lambda_p(t)$, assumed to be time-dependent for generality (see **Fig.A1**). Noting that at the borehole $r = 0$

$$\left.\frac{\partial p_f(r,t)}{\partial t}\right|_{r=o} = \frac{\partial p_f(0,t)}{\partial t} = \frac{dp_o(t)}{dt}, \tag{A6}$$

where $p_o(t)$ is the borehole/injection pressure, we obtain **Eq.(2.11)** in the main text, i.e.,

$$\left.\frac{\partial p_f(r,t)}{\partial t}\right|_{r=R_f} = -\lambda_p(t)\,\frac{dp_o(t)}{dt}, \tag{A7}$$

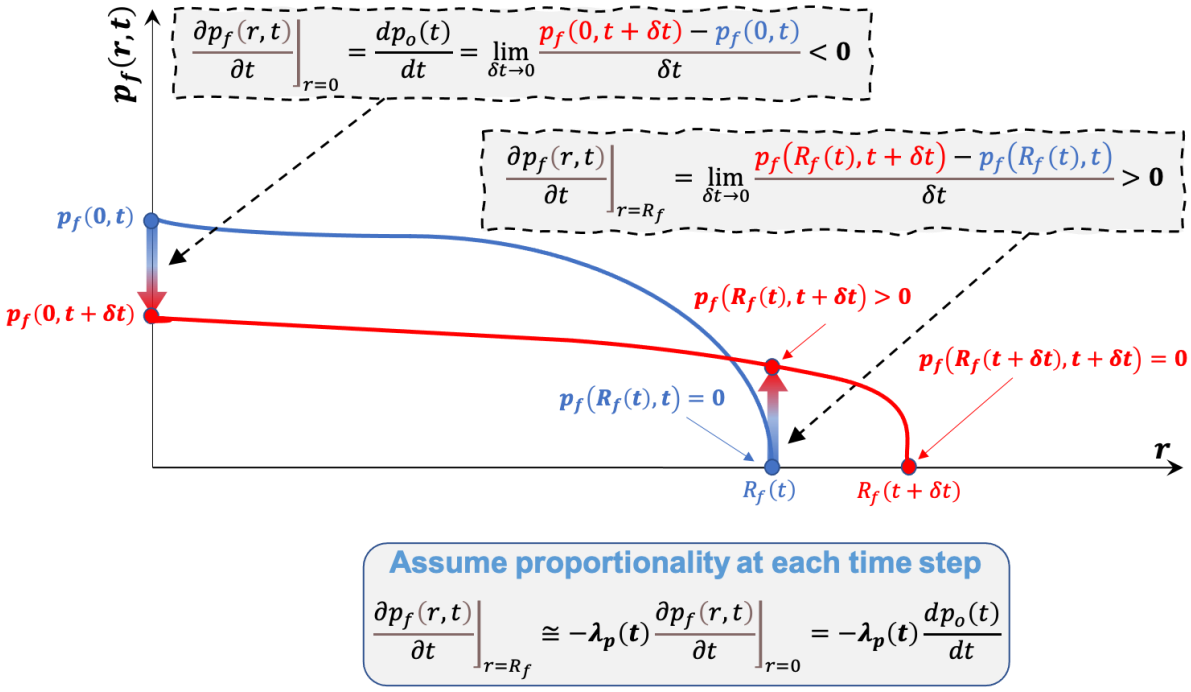

Fig.A1 Schematic justification of the hypothesis on the fluid pressure time derivatives at the inlet and tip of a propagating hydraulic fracture.

A.3. Validation of the assumption on the fluid pressure time derivatives

To validate **Eq.(2.11)** recalled above, we use the few model predictions of fluid pressure profiles within a propagating penny-shaped hydraulic fracture (Kanaun 2018; Kanaun 2020; Zia and Lecampion 2020). Estimating the time derivatives of the fluid pressure at the inlet and near the tip of a propagating hydraulic fracture we can estimate the proportionality coefficient $-\lambda_p(t)$ for the various time steps reported in each publication (see **Fig.A2**). It turns out that λ_p

is approximately fixed for a given fracture propagation simulation (see **Fig.A3**), which corresponds to **Eq.(12)** in the main text, i.e., $\frac{\partial p_f(r,t)}{\partial t}\Big|_{r=R_f(t)}$ is approximately linearly related to $\frac{dp_o(t)}{dt}$ during fracture propagation.

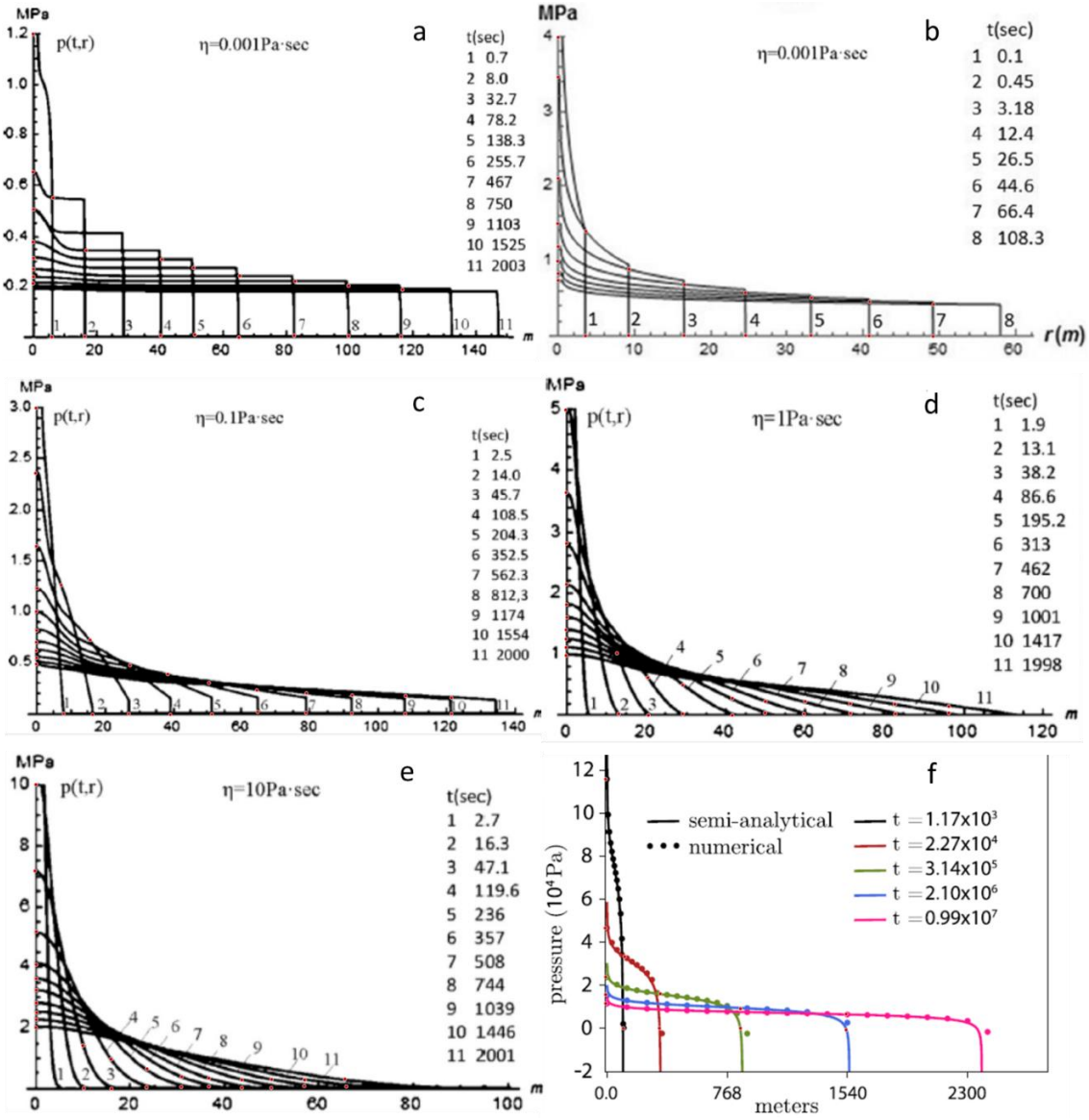

Fig.A2 Fluid pressure P_f (r,t) distribution within a penny-shaped hydraulic fracture: (a)-(e) from (Kanaun 2018; Kanaun 2020); (f) from Zia and Lecampion (2020).

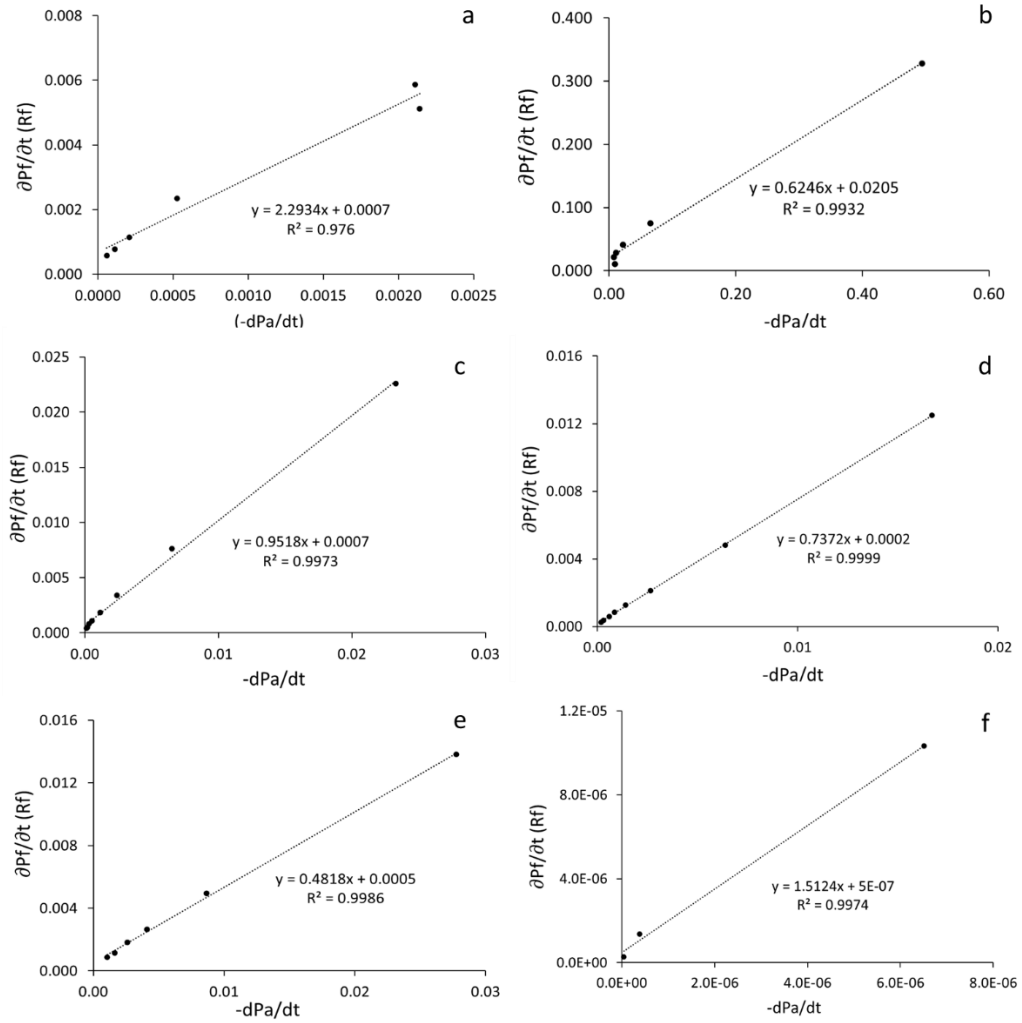

Fig.A3 Validation of **Eq.12** using literature data for a penny-shaped hydraulic fracture: (a)-(e) from (Kanaun 2018; Kanaun 2020); (f) from Zia and Lecampion (2020).

Appendix B: dp_o/dt Correction for early-time initiation

When the process of early-time fracture initiation is significant, i.e., the fracture initiates at a much lower wellbore pressure than the breakdown pressure (i.e. maximum pressure recorded during the entire test), which is mostly happened in stable propagation cases, e.g., hydraulic fracturing tests reported in Lhomme (2005), Sarmadivaleh and Rasouli (2015), and (Lecampion et al. 2017). Therefore, the pressurization rate ($\frac{dp_o}{dt}$) stay positive until reaches to the breakdown pressure, for convenience of calculating the *product PD* $\sqrt{-\frac{w^2}{12\mu_f}\frac{\Delta p_o}{\Delta t}}$, the pressurization rate for early-time fracture propagation ($\frac{\Delta p_o}{\Delta t}_{ei}$) can be corrected as:

$$\frac{\Delta p_o}{\Delta t}_{ei} = \frac{\Delta p_o}{\Delta t} - \frac{\Delta p_o}{\Delta t}_{pri} \tag{B1}$$

where $\frac{\Delta p_o}{\Delta t}_{pri}$ is the linearized wellbore pressurization rate before fracture initiation.

For stable propagation case (i.e., significant early-time initiation & propagation), the correction of $\frac{\Delta p_o}{\Delta t}$ will be only applied prior to maximum wellbore pressure. On the other hand, for unstable propagation case where the initiation and breakdown of wellbore pressure always coincide, the effective pressurization rate ($\frac{\Delta p_o}{\Delta t}_{ei}$) will be used for the entire propagation due to the wellbore storage effect (Lecampion et al. 2017).

Appendix C: Temporal fracturing area (A_d) validation for leak-off and repeated case

C.1. Felser 02: Stable propagation case with leak-off

The evolution of the fracture area with time measured by Lhomme (2005) in Felser 02 is displayed in **Fig.C1**. Similar to Colton 08, the cohesive zone effect are also necessarily accounted. As shown in **Fig.C1a**, the $(\Delta A_R)_m$ exhibited reasonably analogous trend with the *product*$_2$ (PD_2) $\sqrt[3]{-\frac{{w_m}^2}{12\mu_f}(\frac{\Delta p_o}{\Delta t})_m}$, albeit stronger fluctuation of $(\Delta A_R)_m$ is observed after the peak. The robust linear regression analysis of $(\Delta A_R)_m$ verse PD_2 indicates a weakly linear relation with $R^2 = 0.84$ (**Fig.C1b**):

$$(\Delta A_R)_m = 3.07 * \sqrt[3]{-\frac{{w_m}^2}{12\mu_f}\left(\frac{\Delta p_o}{\Delta t}\right)_m} + 1.79 \times 10^{-6} \quad \text{(C1)}$$

The time evolution of the dimensionless relative change in experimental fracture area $(\Delta A_R)_m/A_T$ and the analytical fraction $\sqrt[3]{-\frac{{w_m}^2}{12\mu_f}\left(\frac{\Delta p_o}{\Delta t}\right)_m} \Big/ \sum_{i=1}^{N} \sqrt[3]{-\frac{{w_i}^2}{12\mu_f}\left(\frac{\Delta p_o}{\Delta t}\right)_i}$ are shown in **Fig.C1c**, indicating a reasonably robust fit, despite some fluctuations in measured $(\Delta A_R)_m/A_T$. Finally, **Fig.C1d** compares the predicted evolution of the fracturing area A_d (red triangle) and the experimental data (black dots), validating the hypothesis and approach followed here.

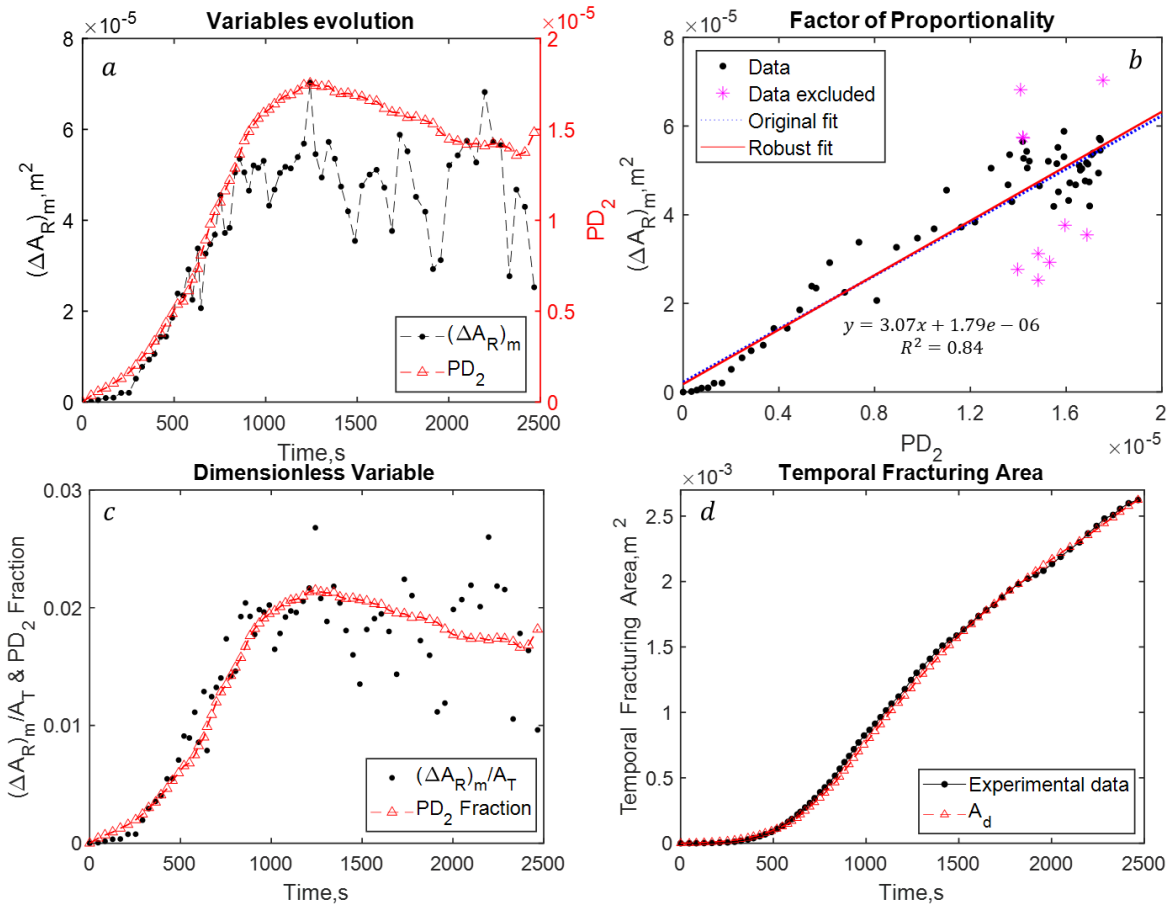

Fig.C1 Evolution of the fracture area for the Felser 02 sandstone sample during stable propagation: Comparison between direct laboratory measurements and predictions of the new model presented here.

C.2. ab5: Unstable propagation case(no leak-off)

The evolution of the fracture area with time measured by Bunger et al. (2013) in ab5 and the prediction from our A_d model are shown in **Fig.C2.** Analogously to the previous PMMA case (c11m1), we obtain the reasonably good linear correlation **Fig.C2b**:

$$(\Delta A_R)_m = 2.9 * \sqrt{-\frac{{w_m}^2}{12\mu_f}\left(\frac{\Delta p_o}{\Delta t}\right)_m} - 3.07e-06, \quad R^2 = 0.93 \qquad \text{(C2)}$$

Accounting for these correlations, **Fig.C2d** show the final results for the two corresponding samples. Again, a reasonable fit is found between predicted and measured evolution of the fracture area, although the minor discrepancy is observed during the intermediate propagation time.

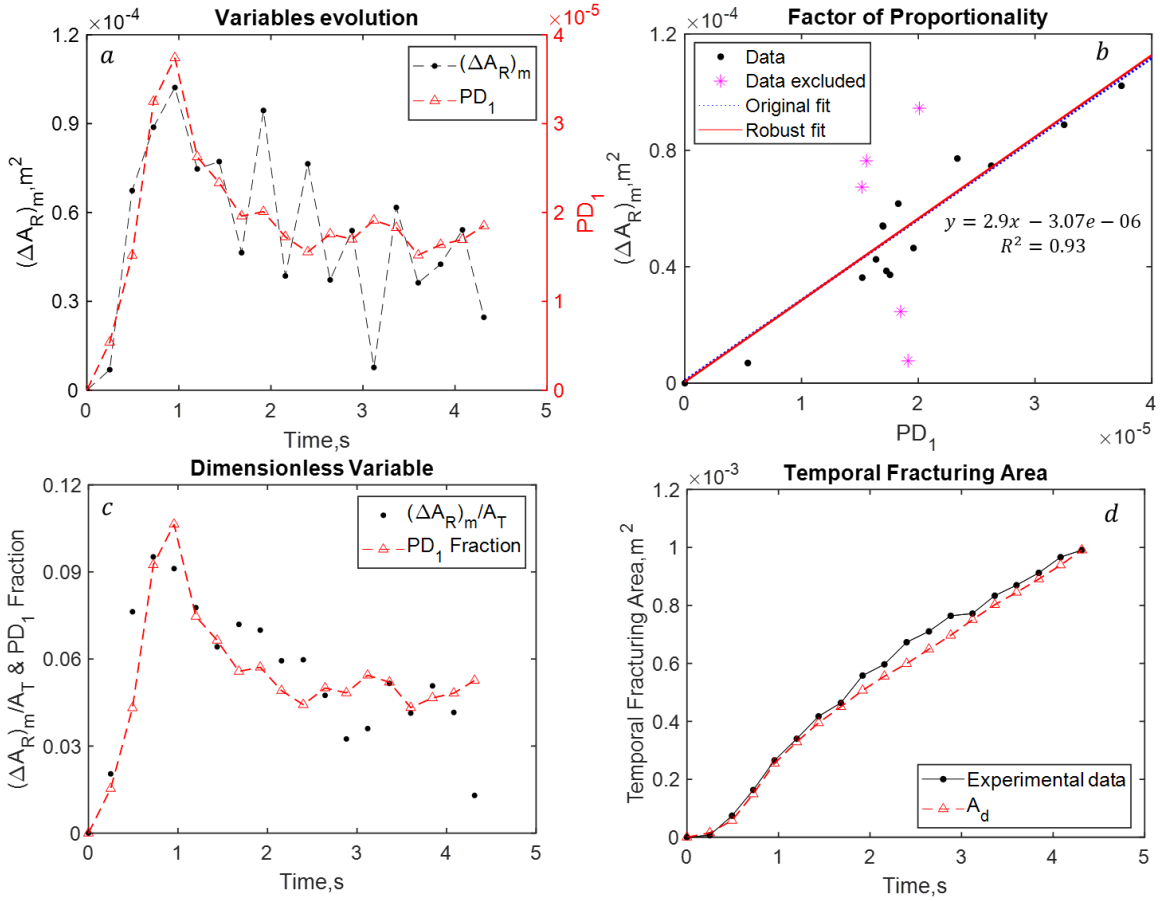

Fig.C2 Evolution of the fracture area for the ab5 (PMMA sample) during stable propagation: Comparison between direct laboratory measurements and predictions of the new model presented here.

C.3. Felser 03: Unstable propagation case with leak-off

Unlike the unstable cases with non-leak-off (i.e., Colton 09, ab5, and c11m1), for Felser 03 the value of $(\Delta A_R)_m$ significantly scatter after propagation of 50s (**Fig.C3a**), resulting in a weak linearity between $(\Delta A_R)_m$ and PD_2 (**Fig.C3b**) :

$$(\Delta A_R)_m = 7053 * \sqrt[3]{-\frac{{w_m}^2}{12\mu_f}\left(\frac{\Delta p_o}{\Delta t}\right)_m} - 9.1e-07,\ R^2 = 0.76 \qquad \text{(C3)}$$

The linear regression analysis indicates that the proportional hypothesis between $(\Delta A_R)_m$ and PD_2 is partially valid; the value of y-axis intercept B are still negligible since $B \ll (\Delta A_R)_m$. Although the dimensionless variable $(\Delta A_R)_m / A_T$ are highly fluctuated after 50s (**Fig.C3c**), the temporal fracturing area (A_d) are in relatively good agreement with the experimental data.

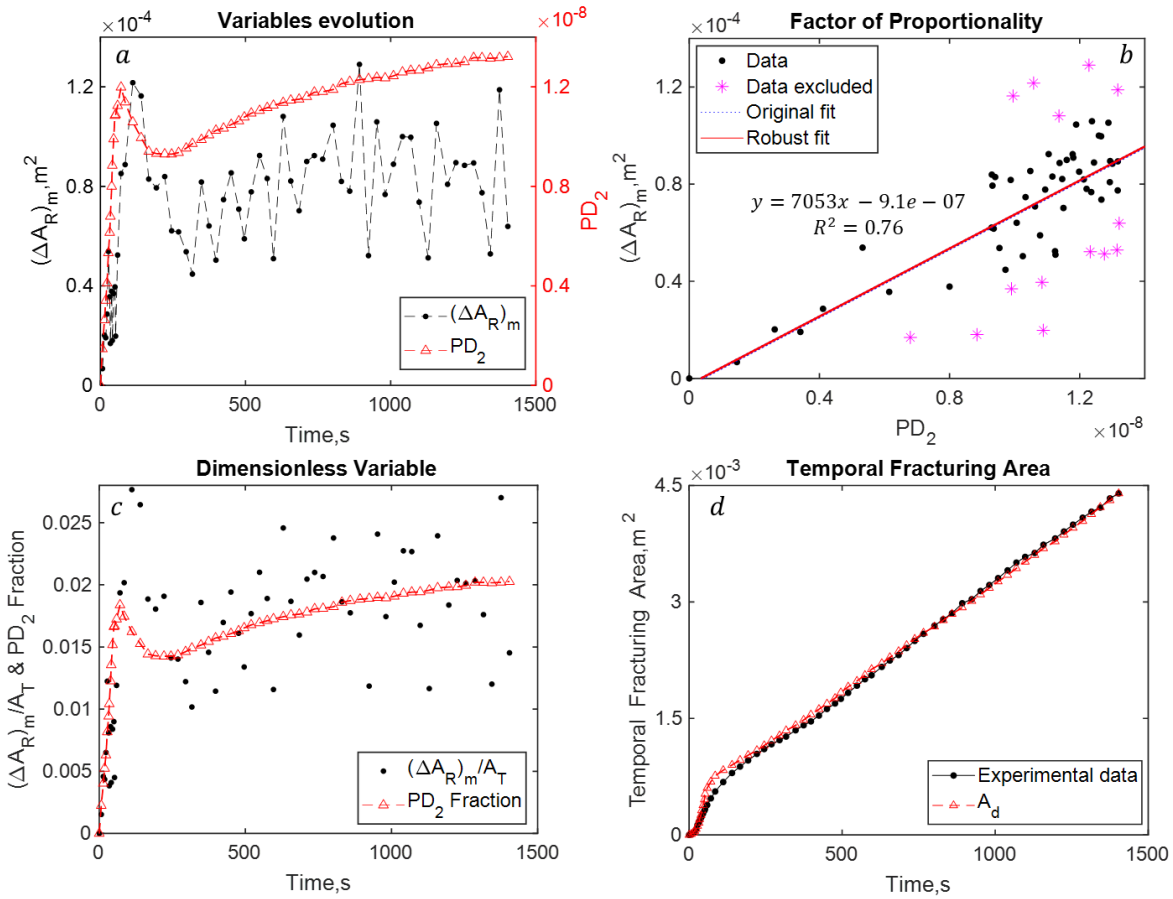

Fig.C3 Evolution of the fracture area for the Felser 03 during stable propagation: Comparison between direct laboratory measurements and predictions of the new model presented here.

Appendix D: Creep data used for stress relaxation analysis in Section 6.4

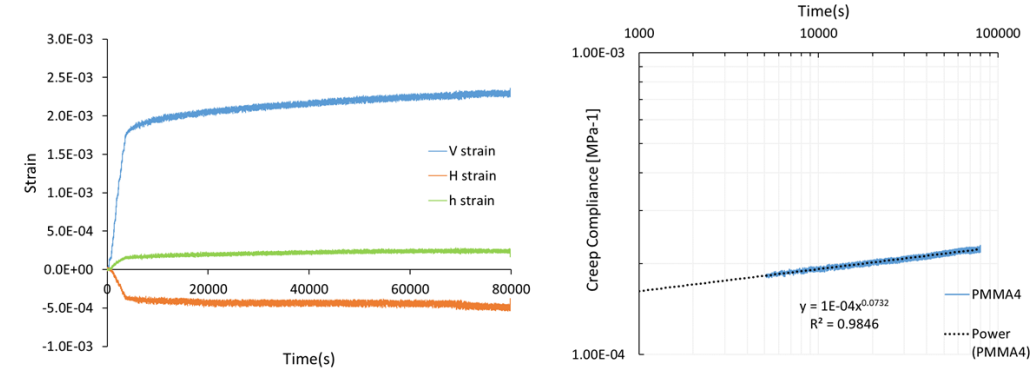

(a)

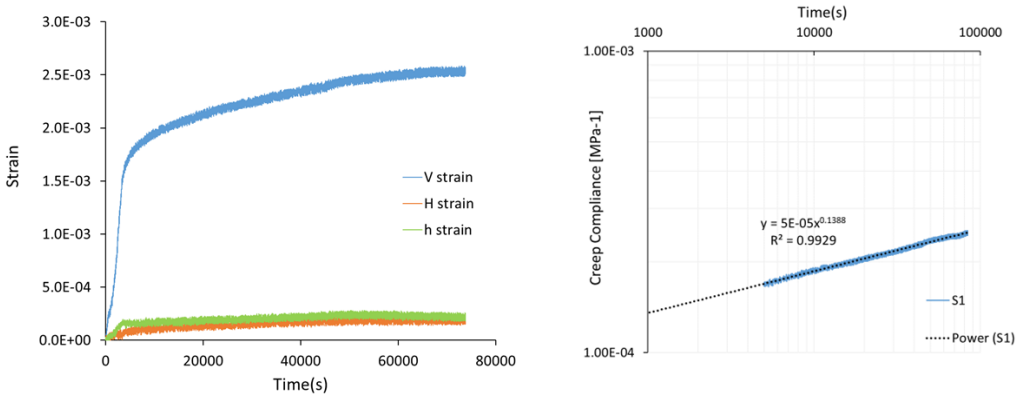

(b)

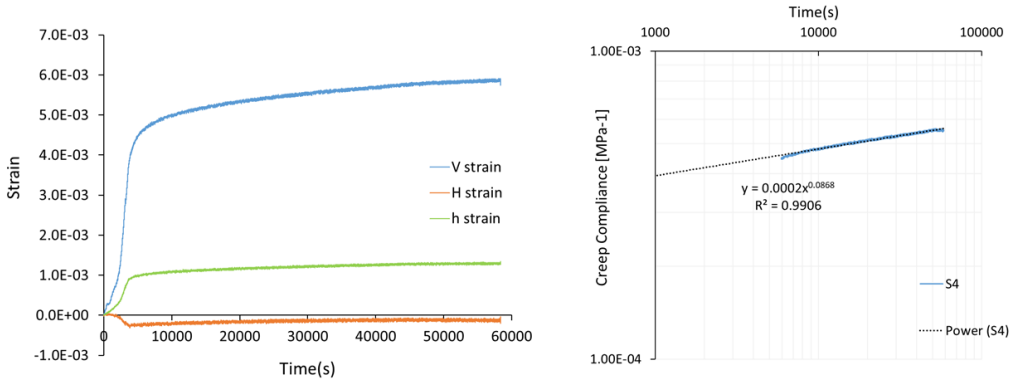

(c)

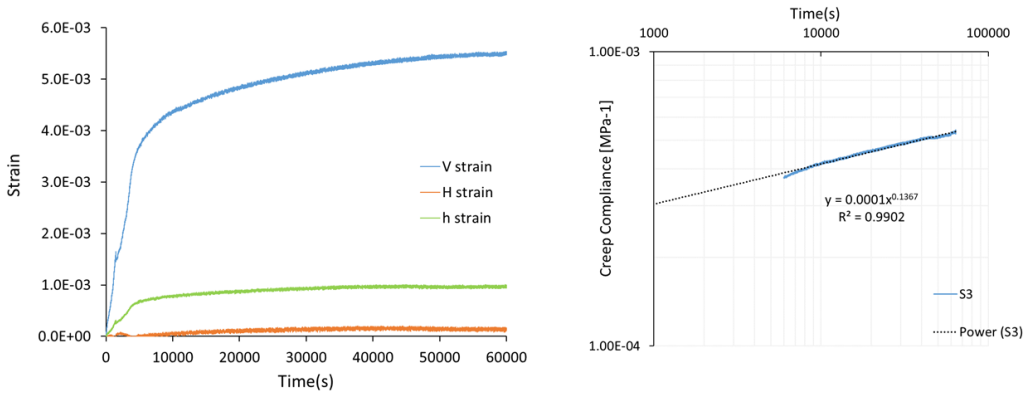

(d)

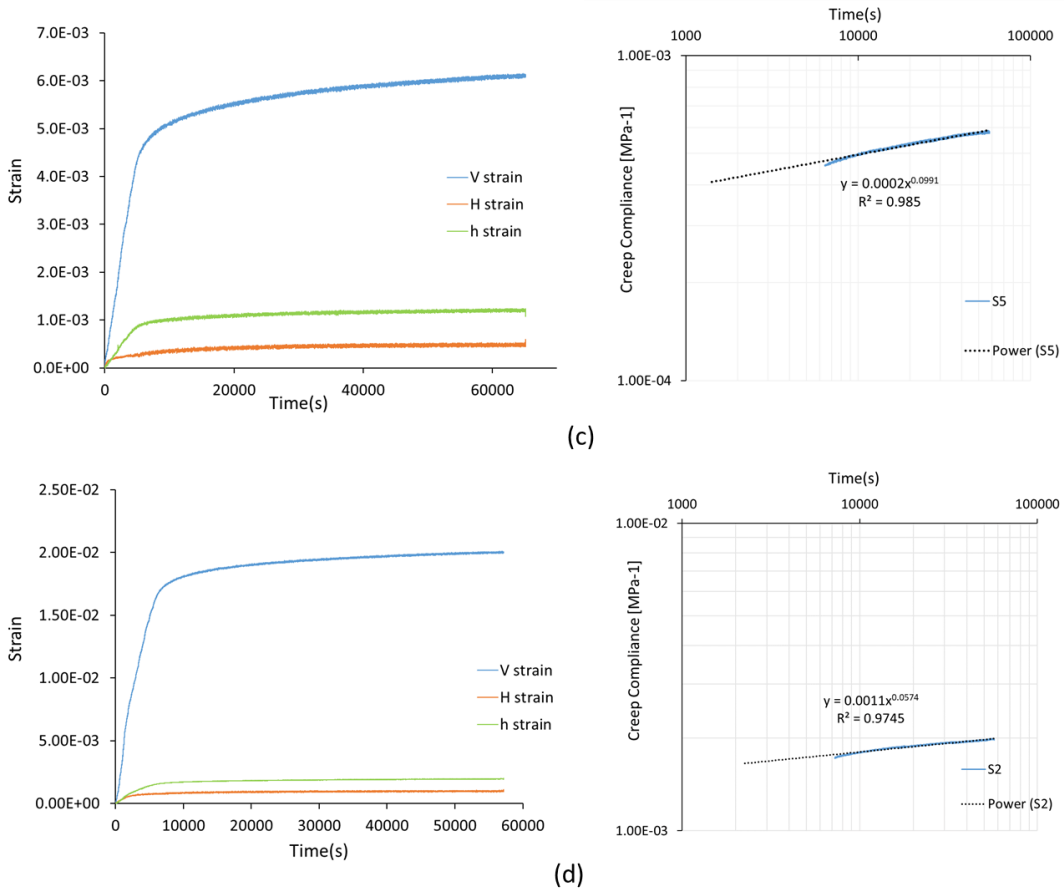

Fig.D 1 Representative creep data (including the loading stage shown at the left) used for stress relaxation analysis for six type of the samples tested in this study: a) PMMA b) Quartz-rich S_1 c)Mixed-average S_4 d) Calcite-rich S_3 e) Clay-rich$_2$ S_5 f) Clay-rich S_2 under 15, 10, and 5MPa

Reference

Abé Ha, Keer L, Mura T (1976) Growth rate of a penny-shaped crack in hydraulic fracturing of rocks, 2 .Journal of Geophysical Research 81:6292-6298

Adachi J, Siebrits E, m, Peirce A, Desroches J (2007) Computer simulation of hydraulic fractures .International Journal of Rock Mechanics and Mining Sciences 44:739-757

Advani S, Lee T, Lee J (1990) Three-dimensional modeling of hydraulic fractures in layered media: part I—finite element formulations

Advani S, Torok J, Lee J, Choudhry S (1987) Explicit time-dependent solutions and numerical evaluations for penny-shaped hydraulic fracture models. Journal of Geophysical Research: Solid Earth 92:8049-8055

Aharonov E, Scholz CH (2019) The brittle-ductile transition predicted by a physics-based friction law. Journal of Geophysical Research: Solid Earth 124:2721-2737

Alpak FO (2021) A Cohesive-Zone Model for Simulating Hydraulic-Fracture Evolution within a Fully Coupled Flow/Geomechanics-Simulation System. SPE Journal 26:22-43

Altindag R, Guney A (2010) Predicting the relationships between brittleness and mechanical properties (UCS, TS and SH) of rocks. Scientific research and Essays 5:2107-2118

Amitrano D (2003) Brittle-ductile transition and associated seismicity: Experimental and numerical studies and relationship with the b value. Journal of Geophysical Research: Solid Earth 108

Batchelor CK, Batchelor G (2000) An introduction to fluid dynamics. Cambridge university press,

Bishop A Progressive failure-with special reference to the mechanism causing it. In: Proc. Geotech. Conf., Oslo, 1967. pp 142-150

Boroumand N, Eaton DW Comparing energy calculations-hydraulic fracturing and microseismic monitoring. In: 74th EAGE Conference and Exhibition incorporating EUROPEC 2012, 2012. European Association of Geoscientists & Engineers, pp cp-293-00090

Brantut N, Schubnel A, Guéguen Y (2011) Damage and rupture dynamics at the brittle-ductile transition: The case of gypsum. Journal of Geophysical Research: Solid Earth 116

Bradley AL (2013) Investigating the Influence of Mechanical anisotropy on the Fracturing Behaviour of Brittle Clay Shales with Application to Deep Geological Repositories.

Bunger AP (2005) Near-surface hydraulic fracture. University of Minnesota

Bunger AP, Detournay E (2007) Early-time solution for a radial hydraulic fracture. Journal of engineering mechanics 133:534-540

Bunger AP, Detournay E (2008) Experimental validation of the tip asymptotics for a fluid-driven crack .Journal of the Mechanics and Physics of Solids 56:3101-3115

Bunger AP, Gordeliy E, Detournay E (2013) Comparison between laboratory experiments and coupled simulations of saucer-shaped hydraulic fractures in homogeneous brittle-elastic solids. Journal of the Mechanics and Physics of Solids 61:1636-1654

Bura E, Seweryn A (2018) Mode I fracture in PMMA specimens with notches–Experimental and numerical studies. Theoretical and Applied Fracture Mechanics 97:140-155

Chang S-H, Lee C-I, Jeon S (2002) Measurement of rock fracture toughness under modes I and II and mixed-mode conditions by using disc-type specimens. Engineering geology 66:79-97

Chen Z, Jeffrey RG, Zhang X, Kear J (2017) Finite-element simulation of a hydraulic fracture interacting with a natural fracture. Spe Journal 22:219-234

Cho* D, Perez M (2014) Rock quality assessment for hydraulic fracturing: A rock physics perspective. In: SEG Technical Program Expanded Abstracts 2014. Society of Exploration Geophysicists, pp 2814-2818

Chong KP, Kuruppu MD, Kuszmaul JS (1987) Fracture toughness determination of layered materials. Engineering fracture mechanics 28:43-54

Clifton RJ, Abou-Sayed AS A variational approach to the prediction of the three-dimensional geometry of hydraulic fractures. In: SPE/DOE Low Permeability Gas Reservoirs Symposium, 1981. OnePetro,

Clifton RJ, Wang J-J Adaptive optimal mesh generator for hydraulic fracturing modeling. In: The 32nd US Symposium on Rock Mechanics (USRMS), 1991. OnePetro,

Dautriat J, Gland N, Dimanov A, Raphanel J (2011) Hydromechanical behavior of heterogeneous carbonate rock under proportional triaxial loadings. Journal of Geophysical Research: Solid Earth 116

De Laguna W (1966) Disposal of radioactive wastes by hydraulic fracturing: part I. General concept and first field experiments. Nuclear Engineering and Design 3:338-352

De Pater C, Cleary M, Quinn T, Barr D, Johnson D, Weijers L (1994a) Experimental verification of dimensional analysis for hydraulic fracturing. SPE Production & Facilities 9:230-238

De Pater C, Weijers L, Savic M, Wolf K, Van Den Hoek P, Barr D (1994b) Experimental study of nonlinear effects in hydraulic fracture propagation (includes associated papers 29225 and 29687) .SPE Production & Facilities 9:239-246

Desroches J, Detournay E, Lenoach B, Papanastasiou P, Pearson JRA, Thiercelin M, Cheng A (1994) The crack tip region in hydraulic fracturing. Proceedings of the Royal Society of London Series A: Mathematical and Physical Sciences 447:39-48

Detournay E Propagation regimes of fluid-driven fractures in impermeable rocks. In: Proceedings of the 10th International Conference on Computer Methods and Advances in Geomechanics, 2004a. pp 1277-1288

Detournay E (2004b) Propagation regimes of fluid-driven fractures in impermeable rocks. International Journal of Geomechanics 4:35-45

Detournay E (2016) Mechanics of hydraulic fractures. Annual Review of Fluid Mechanics 48:311-339

Dontsov E (2016) An approximate solution for a penny-shaped hydraulic fracture that accounts for fracture toughness, fluid viscosity and leak-off. Royal Society open science 3:160737

Economides MJ, Nolte KG (1989) Reservoir stimulation vol 2. Prentice Hall Englewood Cliffs, NJ,

Elices M, Guinea G, Gomez J, Planas J (2002) The cohesive zone model: advantages, limitations and challenges. Engineering fracture mechanics 69:137-163

England A, Green A Some two-dimensional punch and crack problems in classical elasticity. In: Mathematical Proceedings of the Cambridge Philosophical Society, 1963. vol 2. Cambridge University Press, pp 489-500

Evans B, Fredrich JT, Wong TF (1990) The brittle-ductile transition in rocks: Recent experimental and theoretical progress The Brittle-Ductile Transition in Rocks, Geophys Monogr Ser 56:1-20

Feng R et al. Source Mechanism and Stress Inversion for Hydraulic Fracturing Induced Microseismicity in Glutenite Reservoir. *In: SPE/IATMI Asia Pacific Oil & Gas Conference and Exhibition*, 2019. Society of Petroleum Engineers.

Feng R, Chen R, Sarmadivaleh M (2019) A practical fracability evaluation for tight sandstone reservoir with natural interface. The APPEA Journal 59:221-227

Feng R, Zhang Y, Rezagholilou A, Roshan H, Sarmadivaleh M (2020) Brittleness Index: from conventional to hydraulic fracturing energy model.Rock Mechanics and Rock Engineering 53:739-753

Feng R, Liu S, Sarout J, Dautriat J, Zhong Z, Rezaee R, Sarmadivaleh M (2022a) Hydraulic fracturing: Laboratory evidence of the brittle-to-ductile transition with depth. Preprint DOI: doi.org/10.31223/X5PH0S

Feng R., Sarout J., Dautriat J., Ghuwainim Y., Rezaee R., Sarmadivaleh M (2022b). Laboratory validation of a new hydro-mechanical energy-based brittleness index model for hydraulic fracturing. Preprint DOI: doi.org/10.31223/X55M1J

Feng R., Sarout J., Dautriat J., Zhang J., Roshan H., Rezaee R., Sarmadivaleh M (2022c). Data-constrained analytical model for the propagation of a penny-shaped hydraulic fracture under true triaxial stresses. Engineering Fracture Mechanics, under review. Preprint DOI: doi.org/10.21203/rs.3.rs-1525036/v4

Fischer-Cripps AC (2007) Introduction to contact mechanics vol 101. Springer,

Fjaer E, Holt RM, Horsrud P, Raaen AM (2008) Petroleum related rock mechanics. Elsevier,

Fung R, Vilayakumar S, Cormack DE (1987) Calculation of vertical fracture containment in layered formations. SPE formation evaluation 2:518-522
Garagash D, Detournay E (2000) The tip region of a fluid-driven fracture in an elastic medium. J Appl Mech 67:183-192
Garagash DI (2006) Propagation of a plane-strain hydraulic fracture with a fluid lag: Early-time solution. International journal of solids and structures 43:5811-5835
Garagash DI Roughness-dominated hydraulic fracture propagation. In: EOS Trans. AGU (Fall Meeting Suppl.), 2015. vol 52. pp MR41A-2628
Garagash DI (2019) Cohesive-zone effects in hydraulic fracture propagation. Journal of the Mechanics and Physics of Solids 133:103727
Geertsma J, De Klerk F (1969) A rapid method of predicting width and extent of hydraulically induced fractures. Journal of petroleum technology 21:1571-1581
Gischig VS, Preisig G Hydro-fracturing versus hydro-shearing: a critical assessment of two distinct reservoir stimulation mechanisms. In: 13th ISRM International Congress of Rock Mechanics, 2015. OnePetro,
Goebel T, Weingarten M, Chen X, Haffener J, Brodsky E (2017) The 2016 Mw5. 1 Fairview, Oklahoma earthquakes: Evidence for long-range poroelastic triggering at> 40 km from fluid disposal wells. Earth and Planetary Science Letters 472:50-61
Goodfellow S, Nasseri M, Maxwell S, Young R (2015) Hydraulic fracture energy budget: Insights from the laboratory. Geophysical Research Letters 42:3179-3187
Green AE, Zerna W (1992) Theoretical elasticity. Courier Corporation,
Griffith AA (1921) VI. The phenomena of rupture and flow in solids Philosophical transactions of the royal society of london Series A, containing papers of a mathematical or physical character 221:163-198
Hajiabdolmajid V, Kaiser P (2003) Brittleness of rock and stability assessment in hard rock tunneling. Tunnelling and Underground Space Technology 18:35-48
Hajiabdolmajid V, Kaiser P, Martin C (2003) Mobilised strength components in brittle failure of rock .Geotechnique 53:327-336
Han D-h, Nur A, Morgan D (1986) Effects of porosity and clay content on wave velocities in sandstones. Geophysics 51:2093-2107
He W, Chen Z, Shi H, Liu C, Li S (2021) Prediction of acoustic wave velocities by incorporating effects of water saturation and effective pressure. Engineering Geology 280:105890
He W, Hayatdavoudi A (2018) A comprehensive analysis of fracture initiation and propagation in sandstones based on micro-level observation and digital imaging correlation. Journal of Petroleum Science and Engineering 164:75-86
Holt RM, Fjær E, Stenebråten JF, Nes O-M (2015) Brittleness of shales: relevance to borehole collapse and hydraulic fracturing.Journal of Petroleum Science and Engineering 131:200-209
Huang C, Chen S (2021) Effects of Ductility of Organic-Rich Shale on Hydraulic Fracturing: A Fully Coupled Extended-Finite-Element-Method Analysis Using a Modified Cohesive Zone Model SPE Journal 26:591-609
Huang K, Ghassemi A A coupled nonlocal damage model for hydraulic fracture propagation. In: 50th US Rock Mechanics/Geomechanics Symposium, 2016. OnePetro,
Kovalyshen Y (2010) Fluid-driven fracture in poroelastic medium. University of Minnesota,
Kovalyshen Y, Bunger AP, Kear J, Kasperczyk D (2014) Comparison between ultrasonic and photometric methods for hydraulic fracture laboratory monitoring. International journal of rock mechanics and mining sciences 70:368-374
Hucka V, Das B Brittleness determination of rocks by different methods. In: International Journal of Rock Mechanics and Mining Sciences & Geomechanics Abstracts, 1974. vol 10. Elsevier, pp 389-392
Iqbal MA, Rezaee R, Laukamp C, Pejcic B, Smith G (2022) Integrated sedimentary and high-resolution mineralogical characterisation of Ordovician shale from Canning Basin, Western Australia:

Implications for facies heterogeneity evaluation. Journal of Petroleum Science and Engineering 208:109347
Irwin GR (1957) Analysis of stresses and strains near the end of a crack traversing a plate
Iyare U, Blake O, Ramsook R (2021) Brittleness evaluation of Naparima Hill mudstones. Journal of Petroleum Science and Engineering 196:107737
Jarvie DM, Hill RJ, Ruble TE, Pollastro RM (2007) Unconventional shale-gas systems: The Mississippian Barnett Shale of north-central Texas as one model for thermogenic shale-gas assessment AAPG bulletin 91:475-499
Jiang T, Jia C, Wang H (2017) Shale gas horizontal well SRV fracturing technology. Science China Press: Beijing, China,
Jin X, Shah SN, Roegiers J-C, Zhang B Fracability evaluation in shale reservoirs-an integrated petrophysics and geomechanics approach. In: SPE hydraulic fracturing technology conference, 2014. Society of Petroleum Engineers,
Jin X, Shah SN, Roegiers J-C, Zhang B (2015) An integrated petrophysics and geomechanics approach for fracability evaluation in shale reservoirs. SPE Journal 20:518-526
Ju Y, Wu G, Wang Y, Liu P, Yang Y (2021) 3D Numerical Model for Hydraulic Fracture Propagation in Tight Ductile Reservoirs, Considering Multiple Influencing Factors via the Entropy Weight Method. SPE Journal 26:2685-2702
Kanaun S (2018) Efficient numerical solution of the hydraulic fracture problem for planar cracks .International Journal of Engineering Science 127:114-126
Kanaun S (2020) On the hydraulic fracture of poroelastic media. International Journal of Engineering Science 155:103366
Lecampion B, Desroches J (2015) Simultaneous initiation and growth of multiple radial hydraulic fractures from a horizontal wellbore. Journal of the Mechanics and Physics of Solids 82:235-258
Lecampion B, Desroches J, Jeffrey RG, Bunger AP (2017) Experiments versus theory for the initiation and propagation of radial hydraulic fractures in low-permeability materials. Journal of Geophysical Research: Solid Earth 122:1239-1263
Lecampion B, Detournay E (2007) An implicit algorithm for the propagation of a hydraulic fracture with a fluid lag. Computer Methods in Applied Mechanics and Engineering 196:4863-4880
Legarth B, Huenges E, Zimmermann G (2005) Hydraulic fracturing in a sedimentary geothermal reservoir: Results and implications. International Journal of Rock Mechanics and Mining Sciences 42:1028-1041
Lhomme T (2005) Initiation of hydraulic fractures in natural sandstones
Li JX, Rezaee R, Müller TM (2020a) Wettability effect on wave propagation in saturated porous medium.The Journal of the Acoustical Society of America 147:911-920
Li JX, Rezaee R, Müller TM, Sarmadivaleh M (2021) Pore Size Distribution Controls Dynamic Permeability. Geophysical Research Letters 48:e2020GL090558
Li Y, Zhou L, Li D, Zhang S, Tian F, Xie Z, Liu B (2020b) Shale Brittleness Index Based on the Energy Evolution Theory and Evaluation with Logging Data: A Case Study of the Guandong Block ACS omega 5:13164-13175
Lisjak A, Liu Q, Zhao Q, Mahabadi O, Grasselli G (2013) Numerical simulation of acoustic emission in brittle rocks by two-dimensional finite-discrete element analysis. Geophysical Journal International 195:423-443
Lisjak A, Tatone BS, Grasselli G, Vietor T (2014) Numerical modelling of the anisotropic mechanical behaviour of opalinus clay at the laboratory-scale using fem/dem Rock mechanics and rock engineering 47:187-206
Liu D (2021) Hydraulic fracture growth in quasi-brittle materials. EPFL,
Liu D, Lecampion B (2021) Propagation of a plane-strain hydraulic fracture accounting for a rough cohesive zone. Journal of the Mechanics and Physics of Solids 149:104322

Liu D, Brantut N (2022) Micromechanical controls on the brittle-plastic transition in rocks. arXiv preprint arXiv:221111831
Liu Q, Xue L, Sarout J, Lin Q, Pan W, Liu Y, Feng R (2022) Automatic history matching of multistage fractured shale gas reservoir constrained by microseismic data. Journal of Petroleum Science and Engineering 213:110357
Liu S, Ma F, Zhao H, Guo J, Lu R, Feng X (2020) Numerical analysis on the mechanism of hydraulic fracture behavior in heterogeneous reservoir under the stress perturbation. Journal of Natural Gas Science and Engineering 78:103277
Liu S., Klaus T., Feng R., Bona A., Sarmadivaleh M (2022). Microstructure-based Modelling of Hydraulic Fracturing in Low-Permeability Rocks using the Cohesive Element Method. *Engineering Fracture Mechanics*, 108912.
Liu Y et al. (2020) Mechanical properties and failure behavior of dry and water-saturated anisotropic coal under true-triaxial loading conditions. Rock Mechanics and Rock Engineering 53:4799-4818
Long R, Hui C-Y, Gong JP, Bouchbinder E (2020) The fracture of highly deformable soft materials: A tale of two length scales. Annual Review of Condensed Matter Physics 12
Luan X, Di B, Wei J, Li X, Qian K, Xie J, Ding P Laboratory measurements of brittleness anisotropy in synthetic shale with different cementation. In: 2014 SEG Annual Meeting, 2014. Society of Exploration Geophysicists,
Luan X, Di B, Wei J, Zhao J, Li X (2016) Creation of synthetic samples for physical modelling of natural shale. Geophysical Prospecting 64:898-914
Maxwell SC, Shemeta JE, Campbell E, Quirk DJ Microseismic deformation rate monitoring. In: SPE Annual Technical Conference and Exhibition, 2008. OnePetro,
Minaeian V (2014) True triaxial testing of sandstones and shales. Curtin University
Murdoch L (1993) Hydraulic fracturing of soil during laboratory experiments Part 1. Methods and observations. Geotechnique 43:255-265
Mandal PP (2021) Integrated Geomechanical Characterization of Anisotropic Gas Shales: Field Appraisal, Laboratory Testing, Viscoelastic Modelling, and Hydraulic Fracture Simulation. Curtin University
Nabipour A (2013) Experimental and numerical study of ultrasonic monitoring of hydraulic fracture propagation. Curtin University
Naceur KB, Thiercelin M, Touboul E (1990) Simulation of fluid flow in hydraulic fracturing: implications for 3D propagation. SPE production engineering 5:133-141
Nordgren R (1972) Propagation of a vertical hydraulic fracture. Society of Petroleum Engineers Journal 12:306-314
Nygård R, Gutierrez M, Bratli RK, Høeg K (2006) Brittle–ductile transition, shear failure and leakage in shales and mudrocks. Marine and Petroleum Geology 23:201-212
Orowan E (1954) Energy criteria of fracture. Massachusetts Inst of Tech Cambridge Dept of Mechanical Engineering,
Pan C, Li X, He L, Li J (2021) Study on the effect of micro-geometric heterogeneity on mechanical properties of brittle rock using a grain-based discrete element method coupling with the cohesive zone model. International Journal of Rock Mechanics and Mining Sciences 140:104680
Papanastasiou P (1997) The influence of plasticity in hydraulic fracturing. International Journal of Fracture 84:61-79
Papanastasiou P (1999) The effective fracture toughness in hydraulic fracturing. International Journal of Fracture 96:127
Papanastasiou P, Papamichos E, Atkinson C (2016) On the risk of hydraulic fracturing in CO2 geological storage. International Journal for Numerical and Analytical Methods in Geomechanics 40:1472-1484

Papanastasiou P, Thiercelin M Influence of inelastic rock behaviour in hydraulic fracturing. In: International journal of rock mechanics and mining sciences & geomechanics abstracts, 1993. vol 7. Elsevier, pp 1241-1247
Parisio F et al. (2021) A laboratory study of hydraulic fracturing at the brittle-ductile transition. Scientific reports 11:1-16
Peck D, Wrobel M, Perkowska M, Mishuris G (2018) Fluid velocity based simulation of hydraulic fracture: a penny shaped model—part I: the numerical algorithm. Meccanica 53:3615-3635
Perez Altamar R, Marfurt K (2014) Mineralogy-based brittleness prediction from surface seismic data: Application to the Barnett Shale Interpretation 2:T255-T271
Perkins T, Kern LR (1961) Widths of hydraulic fractures. Journal of petroleum technology 13:937-949
Rahjoo M, Eberhardt E (2021) Development of a 3-D confinement-dependent dilation model for brittle rocks; Part 1, derivation of a Cartesian plastic strain increments ratios approach for non-potential flow rules. International Journal of Rock Mechanics and Mining Sciences 145:104668
Ramos Gurjao KG, Gildin E, Gibson R, Everett M (2022) Investigation of Strain Fields Generated by Hydraulic Fracturing with Analytical and Numerical Modeling of Fiber Optic Response. SPE Reservoir Evaluation & Engineering 25:367-379
Richard D, Lerner E, Bouchbinder E (2021) Brittle to ductile transitions in glasses: Roles of soft defects and loading geometry arXiv preprint arXiv:210305258
Rickman R, Mullen MJ, Petre JE, Grieser WV, Kundert D A practical use of shale petrophysics for stimulation design optimization: All shale plays are not clones of the Barnett Shale. In: SPE Annual Technical Conference and Exhibition, 2008. Society of Petroleum Engineers,
Rodriguez IV, Stanchits S (2017) Spatial and temporal variation of seismic attenuation during hydraulic fracturing of a sandstone block subjected to triaxial stress. Journal of Geophysical Research: Solid Earth 122:9012-9030
Roshan H, Masoumi H, Regenauer-Lieb K (2017) Frictional behaviour of sandstone: a sample-size dependent triaxial investigation. Journal of Structural Geology 94:154-165
Rybacki E, Reinicke A, Meier T, Makasi M, Dresen G (2015) What controls the mechanical properties of shale rocks?–Part I: Strength and Young's modulus. Journal of Petroleum Science and Engineering 135:702-722
Salimzadeh S, Khalili N (2015) A three-phase XFEM model for hydraulic fracturing with cohesive crack propagation. Computers and Geotechnics 69:82-92
Salimzadeh S, Paluszny A, Nick HM, Zimmerman RW (2018) A three-dimensional coupled thermo-hydro-mechanical model for deformable fractured geothermal systems. Geothermics 71:212-224
Sarmadivaleh M (2012) Experimental and numerical study of interaction of a pre-existing natural interface and an induced hydraulic fracture. Curtin University
Sarmadivaleh M, Rasouli V (2015) Test design and sample preparation procedure for experimental investigation of hydraulic fracturing interaction modes. Rock Mechanics and Rock Engineering 48:93-105
Sarout J, Esteban L, Delle Piane C, Maney B, Dewhurst DN (2014) Elastic anisotropy of Opalinus Clay under variable saturation and triaxial stress. Geophysical Journal International 198:1662-1682
Sarout J, Guéguen Y (2008a) Anisotropy of elastic wave velocities in deformed shales: Part 1—Experimental results. Geophysics 73:D75-D89
Sarout J, Guéguen Y (2008b) Anisotropy of elastic wave velocities in deformed shales: Part 2—Modeling results. Geophysics 73:D91-D103
Sarris E, Papanastasiou P (2011) The influence of the cohesive process zone in hydraulic fracturing modelling. International Journal of Fracture 167:33-45

Savitski A, Detournay E (2002) Propagation of a penny-shaped fluid-driven fracture in an impermeable rock: asymptotic solutions. International journal of solids and structures 39:6311-6337
Sarvaramini E, Dusseault MB, Komijani M, Gracie R (2019) A non-local plasticity model of stimulated volume evolution during hydraulic fracturing. International Journal of Solids and Structures 159:111-125
Schmidt P, Dutler N, Steeb H (2022) Importance of fracture deformation throughout hydraulic testing under in situ conditions. Geophysical Journal International 228:493-509
Serdyukov S, Kurlenya M, Patutin A (2016) Hydraulic fracturing for in situ stress measurement .Journal of Mining Science 52:1031-1038
Shapiro SA (2015) Fluid-induced seismicity. Cambridge University Press,
Shimizu H, Ito T, Tamagawa T, Tezuka K (2018) A study of the effect of brittleness on hydraulic fracture complexity using a flow-coupled discrete element method. Journal of Petroleum Science and Engineering 160:372-383
Shlyapobersky J Energy analysis of hydraulic fracturing. In: The 26th US Symposium on Rock Mechanics (USRMS), 1985. OnePetro,
Simonson E, Abou-Sayed A, Clifton R (1978) Containment of massive hydraulic fractures. Society of Petroleum Engineers Journal 18:27-32
Sneddon I, Elliot H (1946) The opening of a Griffith crack under internal pressure. Quarterly of Applied Mathematics 4:262-267
Sneddon IN (1946) The distribution of stress in the neighbourhood of a crack in an elastic solid Proceedings of the Royal Society of London Series. A Mathematical and Physical Sciences 187:229-260
Sneddon IN (1995) Fourier transforms. Courier Corporation,
Steiner W, Kaiser PK, Spaun G (2011) Role of brittle fracture in swelling behaviour: evidence from tunnelling case histories/Sprödbruch in wenig festem Fels als Auslöser von Quellvorgängen: Erkenntnisse aus Fallstudien Geomechanics and Tunnelling 4:141-156
Sun C, Jin Z-H (2006) Modeling of composite fracture using cohesive zone and bridging models. Composites science and technology 66:1297-1302
Sone H, Zoback MD (2014) Time-dependent deformation of shale gas reservoir rocks and its long-term effect on the in situ state of stress. International Journal of Rock Mechanics and Mining Sciences 69:120-132
Taleghani AD, Gonzalez-Chavez M, Yu H, Asala H (2018) Numerical simulation of hydraulic fracture propagation in naturally fractured formations using the cohesive zone model. Journal of Petroleum Science and Engineering 165:42-57
Tarasov B, Potvin Y (2013) Universal criteria for rock brittleness estimation under triaxial compression International. Journal of Rock Mechanics and Mining Sciences 59:57-69
Tan Y, Wang S, Rijken M, Hughes K, Ning ILC, Zhang Z, Fang Z (2021) Geomechanical Template for Distributed Acoustic Sensing Strain Patterns during Hydraulic Fracturing. SPE Journal 26:627-638
Tedd P, Carter IC, Watts KS, Charles JA (2011) Investigating hydraulic fracture at a puddle clay core dam Dams and Reservoirs 21:123-135
Vachaparampil A, Ghassemi A (2017) Failure characteristics of three shales under true-triaxial compression International. Journal of Rock Mechanics and Mining Sciences 100:151-159
Valkó P, Economides MJ (1995) Hydraulic fracture mechanics vol 28. Wiley Chichester,
Van Dam D, De Pater C Roughness of hydraulic fractures: The importance of in-situ stress and tip processes. In: SPE Annual Technical Conference and Exhibition, 1999. OnePetro,
Van Dam D, De Pater C, Romijn R (2000a) Analysis of hydraulic fracture closure in laboratory experiments. SPE Production & Facilities 15:151-158
van Dam DB, Papanastasiou P, De Pater C Impact of rock plasticity on hydraulic fracture propagation and closure. In: SPE Annual Technical Conference and Exhibition, 2000b. OnePetro,

van Dam DB, Papanastasiou P, De Pater C (2002) Impact of rock plasticity on hydraulic fracture propagation and closure. SPE Production & Facilities 17:149-159
Vandamme L, Curran J (1989) A three-dimensional hydraulic fracturing simulator. International Journal for Numerical Methods in Engineering 28:909-927
Vinci C, Renner J, Steeb H (2014) A hybrid-dimensional approach for an efficient numerical modeling of the hydro-mechanics of fractures. Water Resources Research 50:1616-1635
Wang FP, Gale JF (2009) Screening criteria for shale-gas systems
Wang H (2015) Numerical modeling of non-planar hydraulic fracture propagation in brittle and ductile rocks using XFEM with cohesive zone method. Journal of Petroleum Science and Engineering 135:127-140
Wang H (2019) Hydraulic fracture propagation in naturally fractured reservoirs: Complex fracture or fracture networks. Journal of Natural Gas Science and Engineering 68:102911
Wang S, Sloan S, Fityus S, Griffiths D, Tang C (2013) Numerical modeling of pore pressure influence on fracture evolution in brittle heterogeneous rocks. Rock mechanics and rock engineering 46:1165-1182
Wang Z, Nakamura T (2004) Simulations of crack propagation in elastic–plastic graded materials. Mechanics of Materials 36:601-622
Warpinski NR, Du J, Zimmer U (2012) Measurements of hydraulic-fracture-induced seismicity in gas shales. SPE Production & Operations 27:240-252
Weinberg RF, Regenauer-Lieb K (2010) Ductile fractures and magma migration from source.Geology 38:363-366
Wong T-f, Baud P (2012) The brittle-ductile transition in porous rock: A review. Journal of Structural Geology 44:25-53
Wrobel M, Papanastasiou P, Dutko M (2022) On the pressure decline analysis for hydraulic fractures in elasto-plastic materials. arXiv preprint arXiv:220206581
Wu R (2006) Some fundamental mechanisms of hydraulic fracturing. Georgia Institute of Technology,
Yagiz S, Yazitova A, Karahan H (2020) Application of differential evolution algorithm and comparing its performance with literature to predict rock brittleness for excavatability. International Journal of Mining, Reclamation and Environment 34:672-685
Yang Y, Liu S, Chang X (2021) Fracture stiffness evaluation with waterless cryogenic treatment and its implication in fluid flowability of treated coals. International Journal of Rock Mechanics and Mining Sciences 142:104727
Yao Y (2012) Linear elastic and cohesive fracture analysis to model hydraulic fracture in brittle and ductile rocks. Rock Mechanics and Rock Engineering 45:375-387
Yu B, Liu C, Chen W, Lu J, Liu Y (2022) Experimental study on deformation and fracture characteristics of coal under different true triaxial hydraulic fracture schemes. Journal of Petroleum Science and Engineering 216:110839
Zeng L, Reid N, Lu Y, Hossain MM, Saeedi A, Xie Q (2020) Effect of the fluid–shale interaction on salinity: implications for high-salinity flowback water during hydraulic fracturing in shales. Energy & Fuels 34:3031-3040
Zhang D, Ranjith P, Perera M (2016) The brittleness indices used in rock mechanics and their application in shale hydraulic fracturing: A review. Journal of Petroleum Science and Engineering 143:158-170
Zhang J, Davis DM, Wong T-F (1993) The brittle-ductile transition in porous sedimentary rocks: Geological implications for accretionary wedge aseismicity. Journal of Structural Geology 15:819-830
Zhang X, Jeffrey RG, Thiercelin M (2009) Mechanics of fluid-driven fracture growth in naturally fractured reservoirs with simple network geometries. Journal of Geophysical Research: Solid Earth 114

Zhang Z et al. (2020) Modeling of fiber-optic strain responses to hydraulic fracturing. Geophysics 85:A45-A50
Zhao H, Wang X, Wang W, Mu E (2018) A simulation method based on energy criterion for network fracturing in shale gas reservoirs. Journal of Natural Gas Science and Engineering 52:295-303
Zheltov AK 3. Formation of vertical fractures by means of highly viscous liquid. In: 4th world petroleum congress, 1955. OnePetro,
Zhou D, Zhang G, Zhao P, Wang Y, Xu S (2018) Effects of post-instability induced by supercritical CO2 phase change on fracture dynamic propagation. Journal of Petroleum Science and Engineering 162:358-366
Zhou J, Chen M, Jin Y, Zhang G-q (2008) Analysis of fracture propagation behavior and fracture geometry using a tri-axial fracturing system in naturally fractured reservoirs. International Journal of Rock Mechanics and Mining Sciences 45:1143-1152
Zia H, Lecampion B (2020) PyFrac: A planar 3D hydraulic fracture simulator. Computer Physics Communications 255:107368
Zoback, M. D., & Kohli, A. H. (2019). *Unconventional reservoir geomechanics*. Cambridge University Press.

Co-authors' approval for publications (submitted papers) included in this Thesis:

Brittleness Index: From Conventional to Hydraulic Fracturing Energy Model. *Rock Mechanics and Rock Engineering* 53: 739-753 (2020).

Runhua Feng[1], Yihuai Zhang[2], Ali Rezagholilou[1], Hamid Roshan[3], Mohammad Sarmadivaleh[1]

[1]School of WASM: Minerals, Energy and Chemical Engineering, Curtin University, 26 Dick Perry Ave, Kensington, WA 6151 Australia

[2]The Lyell Centre, Heriot-Watt University, Edinburgh EH14 4AS, Scotland, United Kingdom

[3]School of Minerals and Energy Resources Engineering, UNSW AUSTRALIA, Kensington, Sydney, 2052, Australia

Name	Conception and design	Acquisition of data & method	Data conditioning & manipulation	Analysis & statistical method	Interpretation & discussion & editing	Final approval
Yihuai Zhang	☐	☒	☐	☐	☒	☐
I acknowledge that these represent my contribution to the above research output.						
Ali Rezagholilou	☒	☒	☐	☐	☒	☐
I acknowledge that these represent my contribution to the above research output.						
Hamid Roshan	☐	☐	☒	☒	☒	☐
I acknowledge that these represent my contribution to the above research output.						
Mohammad Sarmadivaleh	☒	☒	☐	☒	☒	☒
I acknowledge that these represent my contribution to the above research output.						

Laboratory validation of a new hydro-mechanical energy-based brittleness index model for hydraulic fracturing. Preprint DOI: doi.org/10.31223/X55M1J

Runhua Feng[a], Joel Sarout[b] , Jeremie Dautriat[b], Yousef M Al Ghuwainim[a,c], Reza Rezaee[a], Mohammad Sarmadivaleh[a]

[a]School of WASM: Minerals, Energy and Chemical Engineering, Curtin University, 26 Dick Perry Ave, Kensington, WA 6151 Australia

[b]CSIRO Energy, Kensington, WA 6152, Australia

[c]Department of Petroleum Engineering and Geosciences (CPG), King Fahd University of Petroleum & Minerals, KFUPM, Dhahran 31261, Saudi Arabia

Name	Conception and design	Acquisition of data & method	Data conditioning & manipulation	Analysis & statistical method	Interpretation & discussion & editing	Final approval
Joel Sarout	☐	☐	☒	☒	☒	☐
I acknowledge that these represent my contribution to the above research output.						
Jeremie Dautriat	☐	☒	☒	☐	☒	☐
I acknowledge that these represent my contribution to the above research output.						
Yousef M Al Ghuwainim	☐	☒	☐	☐	☒	☐
I acknowledge that these represent my contribution to the above research output.						
Reza Rezaee	☐	☐	☒	☐	☒	☐
I acknowledge that these represent my contribution to the above research output.						
Mohammad Sarmadivaleh	☒	☒	☐	☒	☒	☒
I acknowledge that these represent my contribution to the above research output.						

Data-constrained analytical model for the propagation of a penny-shaped hydraulic fracture under true triaxial stresses. *Engineering Fracture Mechanics,* under review. Preprint DOI: doi.org/10.21203/rs.3.rs-1525036/v4

Runhua Feng[1], Joel Sarout[2] , Jeremie Dautriat[2], Jiecheng Zhang[3], Hamid Roshan[4] , Reza Rezaee[1], Mohammad Sarmadivaleh[1]

[1]School of WASM: Minerals, Energy and Chemical Engineering, Curtin University, 26 Dick Perry Ave, Kensington, WA 6151, Australia

[2]CSIRO Energy, Perth, WA 6151, Australia

[3]College of Safety and Ocean Engineering, China University of Petroleum-Beijing, China

[4]School of Minerals and Energy Resources Engineering, UNSW AUSTRALIA, Kensington, Sydney 2052, Australia

Name	conception and design	Acquisition of data & method	Data conditioning & manipulation	Analysis & statistical method	Interpretation & discussion & editing	Final approval
Joel Sarout	☒	☐	☒	☒	☒	☐
I acknowledge that these represent my contribution to the above research output.						
Jeremie Dautriat	☐	☒	☐	☒	☒	☐
I acknowledge that these represent my contribution to the above research output.						
Jiecheng Zhang	☐	☐	☒	☒	☒	☐
I acknowledge that these represent my contribution to the above research output.						
Hamid Roshan	☐	☐	☒	☒	☒	☐
I acknowledge that these represent my contribution to the above research output.						
Reza Rezaee	☐	☐	☒	☒	☒	☐

I acknowledge that these represent my contribution to the above research output.						
Mohammad Sarmadivaleh	☒	☒	☐	☒	☒	☒
I acknowledge that these represent my contribution to the above research output.						

Hydraulic fracturing: Laboratory evidence of the brittle-to-ductile transition with depth. *Journal of Petroleum Science and Engineering*, under review. Preprint DOI: doi.org/10.31223/X5PH0S

Runhua Feng[1], Shuo Liu[1] , Joel Sarout[2] , Jeremie Dautriat[2], Zhiqi Zhong[1,3], Reza Rezaee[1], Mohammad Sarmadivaleh[1]

[1]School of WASM: Minerals, Energy and Chemical Engineering, Curtin University, 26 Dick Perry Ave, Kensington, WA 6151 Australia

[2]CSIRO Energy, Perth, WA 6151, Australia

[3] College of Energy, Chengdu University of Technology, Chengdu, China

Name	conception and design	Acquisition of data & method	Data conditioning & manipulation	Analysis & statistical method	Interpretation & discussion & editing	Final approval
Shuo Liu	☐	☒	☒	☒	☒	☐
I acknowledge that these represent my contribution to the above research output.						
Joel Sarout	☐	☐	☒	☒	☒	☐
I acknowledge that these represent my contribution to the above research output.						
Jeremie Dautriat	☐	☒	☒	☐	☒	☐
I acknowledge that these represent my contribution to the above research output.						
Zhiqi Zhong	☐	☒	☒	☐	☒	☐

I acknowledge that these represent my contribution to the above research output.						
Reza Rezaee	☐	☐	☒	☒	☒	☐
I acknowledge that these represent my contribution to the above research output.						
Mohammad Sarmadivaleh	☒	☒	☐	☒	☒	☒
I acknowledge that these represent my contribution to the above research output.						